

**DEVELOPMENT OF A MOLECULAR RAYLEIGH SCATTERING
DIAGNOSTIC FOR SIMULTANEOUS TIME-RESOLVED MEASUREMENT OF
TEMPERATURE, VELOCITY, AND DENSITY**

by

AMY FLORENCE MIELKE

Submitted in partial fulfillment of the requirements

For the degree of Doctor of Philosophy

Dissertation Adviser: Dr. Chih-Jen Sung

Department of Mechanical and Aerospace Engineering

CASE WESTERN RESERVE UNIVERSITY

January, 2008

CASE WESTERN RESERVE UNIVERSITY
SCHOOL OF GRADUATE STUDIES

We hereby approve the dissertation of

candidate for the Ph.D. degree *.

(signed) _____

(chair of the committee)

(date) _____

*We also certify that written approval has been obtained for any proprietary material contained therein.

CHAPTER 3: UNCERTAINTY ANALYSIS AND NUMERICAL SIMULATION	46
3.1 Introduction.....	46
3.2 Lower bound for measurement uncertainty	46
3.2.1 Experiment optimization.....	48
3.2.2 Experiment measurement uncertainty.....	51
3.3 Simulation of <i>noisy</i> data.....	57
CHAPTER 4: EXPERIMENTAL SETUP AND PROCEDURE	66
4.1 Introduction.....	66
4.2 Measurement approach	66
4.3 Acoustically modulated nozzle flow.....	67
4.4 Asymmetric oscillating counterflow with unequal enthalpies.....	71
4.5 High speed electrically-heated jet.....	76
4.6 Spectral analysis and detection.....	80
CHAPTER 5: RESULTS AND DISCUSSION	85
5.1 Introduction.....	85
5.2 Experiment calibration and data analysis methods.....	85
5.2.1 Calibration.....	85
5.2.2 Data analysis and simulations.....	89
5.2.3 Power spectral calculations.....	90
5.3 Experiment 1: Acoustically modulated jet: velocity fluctuation validation study.....	92
5.4 Experiment 2: Asymmetric oscillating counterflow with unequal enthalpies: temperature and density fluctuation validation study.....	103
5.4.1 Temperature fluctuation validation.....	105
5.4.2 Density fluctuation validation.....	111
5.5 Experiment 3: High speed electrically-heated jet: simultaneous measurement demonstration	117
5.5.1 Measurements in low velocity, low temperature flow (case 1)	118
5.5.2 Measurements in high velocity, low temperature flow (case 2) ...	126
5.5.3 Measurements in low velocity, high temperature flow (case 3) ...	133
CHAPTER 6: CONCLUSIONS AND FUTURE WORK.....	139
6.1 Concluding statements.....	139
6.2 Recommendations and future work	142

APPENDIX A: RAMAN SCATTERING CONTRIBUTION TO RAYLEIGH SIGNAL	145
A.1 Introduction	145
A.2 Rotational Raman scattering	145
APPENDIX B: THE POISSON DISTRIBUTION	149
B.1 Introduction	149
B.2 Poisson distribution	149
APPENDIX C: CRAMER-RAO LOWER BOUND.....	151
C.1 Introduction	151
C.2 Derivation of the lower bound for an <i>ideal</i> instrument	151
C.3 Sample calculation for an <i>ideal</i> loss-free instrument	155
C.4 Lower bound for a <i>real</i> instrument.....	157
APPENDIX D: NUMERICAL SIMULATION OF RAYLEIGH PHOTON COUNT DATA.....	158
D.1 Introduction	158
D.2 Computation algorithm.....	159
APPENDIX E: DATA ANALYSIS BY MAXIMUM LIKELIHOOD PARAMETER ESTIMATION.....	162
E.1 Introduction	162
E.2 Model function and parameter estimation.....	162
E.3 Algorithm for parameter estimation of experimental data	167
APPENDIX F: VELOCITY BIAS ERROR DUE TO LASER FREQUENCY INSTABILITY	170
F.1 Introduction	170
F.2 Velocity bias error in Rayleigh measurements.....	170
F.3 Laser frequency instability	173
F.4 Quantification of velocity error associated with laser frequency instability	175
F.5 Potential solutions for reducing bias error	176
BIBLIOGRAPHY.....	177

LIST OF TABLES

Table 1.1. Summary of molecular-based optical measurement techniques	31
Table 1.2. Summary of particle-based optical measurement techniques	32
Table C.1. Experiment parameters for 32 kHz data rate and air at 298 K and 1 atm.....	156

LIST OF FIGURES

<p>Figure 1.1. Scattering vector diagram. The incident wave vector is \vec{k}_0 and the scattered wave vector propagating to the detector is \vec{k}_s where χ_s is the scattering angle. These two vectors define an interaction vector in the direction $\vec{K} = \vec{k}_s - \vec{k}_0$ that defines the measured velocity component direction. The plane defined by these vectors is referred to as the scattering plane.....</p>	9
<p>Figure 1.2. Transmission profile of an iodine vapor absorption filter near 532 nm wavelength This plot was taken from Forkey et al. (1997)</p>	19
<p>Figure 2.1. Rayleigh scattering spectrum.....</p>	35
<p>Figure 2.2. Light scattering from a moving particle</p>	37
<p>Figure 2.3. Rayleigh scattering spectrum for various y-parameters</p>	38
<p>Figure 2.4. Fabry-Perot interferometer</p>	40
<p>Figure 2.5. Concentric ring interference pattern from a planar single frequency light source imaged through a Fabry-Perot interferometer operated in the static imaging mode.....</p>	40
<p>Figure 3.1. Optimization of the outer radius of the third concentric mirror from the center of the mirror system</p>	49
<p>Figure 3.2. Radial slice of a fringe pattern showing the annular regions detected by the four PMTs where $r_{o,1}$, $r_{o,2}$, and $r_{o,3}$ are the outer radii of the first three mirrors and r_{max} is the radius of the image of the fiber face.</p>	50
<p>Figure 3.3. Optimization of reference fringe radius.....</p>	50
<p>Figure 3.4. Optimization of reference fringe radius for various flow velocities</p>	51
<p>Figure 3.5. Relative uncertainty for instantaneous density estimates for 32 kHz sampling rate.....</p>	52
<p>Figure 3.6. Absolute uncertainty for instantaneous temperature estimates for 32 kHz sampling rate</p>	53
<p>Figure 3.7. Absolute uncertainty for instantaneous velocity estimates for 32 kHz sampling rate.....</p>	54

Figure 3.8. Effect of aperture and turbulence broadening on the Rayleigh scattering spectrum for $y = 1.0$, $f/3.7$ collection optics and 16% turbulence intensity. (Mielke et al., 2005)	56
Figure 3.9. Effect of aperture and turbulence broadening on the Rayleigh scattering spectrum for $y = 3.2$, $f/3.7$ collection optics and 16% turbulence intensity. (Mielke et al., 2005)	56
Figure 3.10. Simulated time-resolved density data at 32 kHz data rate.....	59
Figure 3.11. Simulated time-resolved temperature data at 32 kHz data rate	59
Figure 3.12. Simulated time-resolved velocity data at 32 kHz data rate	60
Figure 3.13. Temperature rms error based on simulated data analysis over the expected temperature and velocity ranges for a sampling rate of 32 kHz	60
Figure 3.14. Velocity rms error based on simulated data analysis over the expected temperature and velocity ranges for a sampling rate of 32 kHz	61
Figure 3.15. Density power spectrum calculated using the data from figure 3.10	63
Figure 3.16. Temperature power spectrum calculated using data from figure 3.11	63
Figure 3.17. Velocity power spectrum calculated using the data from figure 3.12	63
Figure 3.18. Temperature spectral noise floor based on simulated data analysis over the expected temperature and velocity ranges at a sampling rate of 32 kHz.....	64
Figure 3.19. Velocity spectral noise floor based on simulated data analysis over the expected temperature and velocity ranges at a sampling rate of 32 kHz.....	64
Figure 3.20. Temperature fluctuation amplitude lower bound based on spectral noise floor values presented in figure 3.18	65
Figure 3.21. Velocity fluctuation amplitude lower bound based on spectral noise floor values presented in figure 3.19.....	65
Figure 4.1. Dissection of Fabry-Perot fringe pattern into one circular and three annular regions.....	67
Figure 4.2. Diagram of laser and collection optics for acoustically-excited nozzle flow experiment	70
Figure 4.3. Photograph of acoustically-excited nozzle flow experiment. See figure 4.2 for label descriptions	71

Figure 4.4. Diagram of laser and collection optics for asymmetric oscillating counterflow experiment	74
Figure 4.5. 3D schematic of asymmetric oscillating counterflow experiment. See figure 4.4 for label descriptions	75
Figure 4.6. Photograph of the laser and opposed hot and cold jets in the asymmetric oscillating counterflow experiment. See figure 4.4 for label descriptions	75
Figure 4.7. Photograph of the shadowgraph image plane.....	76
Figure 4.8. Diagram of laser and collection optics for high speed heated jet experiment.....	79
Figure 4.9. Photograph of the high speed heated jet experiment. See figure 4.8 for label descriptions	79
Figure 4.10. Schematic of spectral analysis and detection optics	82
Figure 4.11. 3D schematic of the asymmetric oscillating counterflow experiment collection optics with the laser beam propagation configured for Fabry-Perot stabilization. See figure 4.4 for label descriptions.....	82
Figure 4.12. Photon counting electronics and data acquisition hardware schematic...	84
Figure 5.1. Density calculated from thermocouple and pressure probe data by ideal gas law plotted as a function of PMT 5 photoelectron counts at a 32 kHz sampling rate in the heated jet experiment. The equation of the linear curve fit shown is used to evaluate time-resolved density in the experiment	87
Figure 5.2. Temperature measured by the Rayleigh technique compared to thermocouple measured temperature at the calibration points for 1, 16, and 32 kHz data rates in the heated jet experiment	87
Figure 5.3. Velocity measured by the Rayleigh technique compared to velocity calculated by isentropic flow relations using pressure probe and thermocouple measurements at the calibration points for 1, 16, and 32 kHz data rates in the heated jet experiment	88
Figure 5.4. Mean temperature and velocity error for the calibration data presented in figures 5.2 and 5.3.....	88
Figure 5.5. Simulated velocity data for 50 Hz sinusoidal velocity perturbation with $mean = 12.6$ m/s and $A = 14.6$ m/s, sampled at 16 kHz.....	97

Figure 5.6. Power spectra of simulated velocity data from figure 5.5	97
Figure 5.7. Experimental velocity data for a sinusoidal velocity perturbation with fundamental frequency of 50 Hz, sampled at 16 kHz.....	98
Figure 5.8. Power spectra of experimental velocity data from figure 5.7.....	98
Figure 5.9. Simulated velocity data for 50 Hz sinusoidal velocity perturbation with $mean = 12.6$ m/s and $A = 14.6$ m/s, sampled at 32 kHz.....	99
Figure 5.10. Power spectra of simulated velocity data from figure 5.9.....	99
Figure 5.11. Experimental velocity data for a sinusoidal velocity perturbation with fundamental frequency of 50 Hz. Rayleigh data sampled at 32 kHz and hotwire data sampled at 16 kHz.....	100
Figure 5.12. Power spectra of experimental velocity data from figure 5.11.....	100
Figure 5.13. Power spectrum of speaker diaphragm displacement measured by a scanning laser doppler vibrometer showing harmonic components in the speaker output	101
Figure 5.14. Simulated 16 kHz rate velocity data for 50 Hz fundamental sinusoidal velocity perturbation with $mean = 12.6$ m/s and $A(i) = 14.6, 5.7, 2.6, 1.6, 1.5, 1.1, 1.08, 0.94, 0.72, 0.7$ m/s for $i = 1$ to 10, where $A(1)$ is the amplitude at the fundamental frequency and $A(i)$ is the amplitude at the i^{th} harmonic frequency.....	101
Figure 5.15. Power spectra of simulated velocity data from figure 5.14.....	102
Figure 5.16. Experimental velocity power spectrum for Rayleigh and hotwire data illustrating the benefit of subtracting the noise floor from the Rayleigh power spectrum.....	102
Figure 5.17. Rayleigh velocity data acquired in the asymmetric oscillating counterflow experiment with 100 Hz acoustic modulation compared to simulated non-fluctuating velocity data	104
Figure 5.18. Power spectra of the Rayleigh and simulated velocity data shown in figure 5.17.....	104
Figure 5.19. Simulated 16 kHz rate temperature data for 100 Hz fundamental sinusoidal temperature perturbation with $mean = 360$ K and $A(i) = 65.9, 10.6, 8.4, 4.4$ K for $i = 1$ to 4, where $A(1)$ is the amplitude at the fundamental frequency and $A(i)$ is the amplitude at the i^{th} harmonic frequency.....	107

Figure 5.20. Power spectra of simulated temperature data from figure 5.19.....	107
Figure 5.21. Experimental temperature data for a sinusoidal temperature perturbation with fundamental frequency of 100 Hz. Rayleigh data is sampled at 16 kHz and coldwire data is sampled at 1 kHz.....	108
Figure 5.22. Power spectra of experimental temperature data from figure 5.21	108
Figure 5.23. Simulated 32 kHz rate temperature data for 100 Hz fundamental sinusoidal temperature perturbation with <i>mean</i> and <i>A(i)</i> values same as in figure 5.19.....	109
Figure 5.24. Power spectra of simulated temperature data from figure 5.23.....	109
Figure 5.25. Experimental temperature data for a sinusoidal temperature perturbation with fundamental frequency of 100 Hz. Rayleigh data is sampled at 32 kHz and coldwire data is sampled at 1 kHz.....	110
Figure 5.26. Power spectra of experimental temperature data from figure 5.25	110
Figure 5.27. Simulated 16 kHz rate density data based on the 100 Hz fundamental sinusoidal temperature perturbation presented in figure 5.19. Density was calculated from the temperature input using ideal gas law and assuming atmospheric pressure.....	113
Figure 5.28. Power spectra of simulated density data from figure 5.27	113
Figure 5.29. Experimental density data measured directly by the Rayleigh technique and calculated from coldwire temperature measurements using ideal gas law for a sinusoidal density perturbation with fundamental frequency of 100 Hz. Rayleigh data is sampled at 16 kHz and coldwire data is sampled at 1 kHz	114
Figure 5.30. Power spectra of experimental density data from figure 5.29.....	114
Figure 5.31. Simulated 32 kHz rate density data based on the 100 Hz fundamental sinusoidal temperature perturbation presented in figure 5.23. Density was calculated from the temperature input using ideal gas law and assuming atmospheric pressure.....	115
Figure 5.32. Power spectra of simulated density data from figure 5.31	115
Figure 5.33. Experimental density data measured directly by the Rayleigh technique and calculated from coldwire temperature measurements using ideal gas law for a sinusoidal density perturbation with fundamental frequency of 100 Hz. Rayleigh data is sampled at 32 kHz and coldwire data is sampled at 1 kHz	116

Figure 5.34. Power spectra of experimental density data from figure 5.33	116
Figure 5.35. Density power spectra calculated from Rayleigh and coldwire data acquired in the shear layer of a flow with maximum temperature and velocity of 420 K and 38 m/s	119
Figure 5.36. Low frequency region of the density power spectra shown in figure 5.35.....	119
Figure 5.37. Temperature power spectra calculated from Rayleigh and coldwire data acquired in the shear layer of a flow with maximum temperature and velocity of 420 K and 38 m/s.....	120
Figure 5.38. Low frequency region of the temperature power spectra shown in figure 5.37.....	120
Figure 5.39. Velocity power spectra calculated from Rayleigh data acquired in the shear layer of a flow with maximum temperature and velocity of 420 K and 38 m/s and hotwire data acquired in a room temperature flow with maximum velocity of 38 m/s.....	120
Figure 5.40. Low frequency region of the velocity power spectra shown in figure 5.39.....	120
Figure 5.41. Mean density profile calculated from time-resolved Rayleigh data and measured by a thermocouple for a flow with maximum temperature and velocity of 420 K and 38 m/s.....	122
Figure 5.42. Density fluctuation profile calculated from Rayleigh and coldwire measurements in a flow with maximum temperature and velocity of 420 K and 38 m/s.....	122
Figure 5.43. Mean temperature profile calculated from time-resolved Rayleigh and coldwire data and measured by a thermocouple for a flow with maximum temperature and velocity of 420 K and 38 m/s.....	124
Figure 5.44. Temperature fluctuation profile calculated from Rayleigh and coldwire measurements in a flow with maximum temperature and velocity of 420 K and 38 m/s	124
Figure 5.45. Mean velocity profile calculated from time-resolved Rayleigh and data and measured by a pitot tube in a flow with maximum temperature and velocity of 420 K and 38 m/s and hotwire measurements in a room temperature flow with maximum velocity of 38 m/s.....	126

Figure 5.46. Velocity fluctuation profile calculated from Rayleigh measurements in a flow with maximum temperature and velocity of 420 K and 38 m/s and hotwire measurements in a room temperature flow with maximum velocity of 38 m/s.....	126
Figure 5.47. Density power spectrum calculated from Rayleigh data acquired in the shear layer of a flow with maximum temperature and velocity of 420 K and 110 m/s.....	128
Figure 5.48. Temperature power spectra calculated from Rayleigh temperature and density data acquired in the shear layer of a flow with maximum temperature and velocity of 420 K and 110 m/s	128
Figure 5.49. Velocity power spectra calculated from Rayleigh data acquired in the shear layer of a flow with maximum temperature and velocity of 420 K and 110 m/s and hotwire data acquired in a room temperature flow with maximum velocity of 110 m/s.....	129
Figure 5.50. Mean density profile calculated from time-resolved Rayleigh data and measured by a thermocouple for a flow with maximum temperature and velocity of 420 K and 110 m/s.....	130
Figure 5.51. Density fluctuation profile calculated from Rayleigh measurements in a flow with maximum temperature and velocity of 420 K and 110 m/s	130
Figure 5.52. Mean temperature profile calculated from time-resolved Rayleigh data and measured by a thermocouple for a flow with maximum temperature and velocity of 420 K and 110 m/s.....	131
Figure 5.53. Temperature fluctuation profile calculated from Rayleigh measurements in a flow with maximum temperature and velocity of 420 K and 110 m/s.....	131
Figure 5.54. Mean velocity profile calculated from time-resolved Rayleigh and data in a flow with maximum temperature and velocity of 420 K and 110 m/s and hotwire measurements in a room temperature flow with similar maximum velocity.....	132
Figure 5.55. Velocity fluctuation profile calculated from Rayleigh measurements in a flow with maximum temperature and velocity of 420 K and 110 m/s and hotwire measurements in a room temperature flow with similar maximum velocity.....	132
Figure 5.56. Density power spectrum calculated from Rayleigh data acquired in the shear layer of a flow with maximum temperature and velocity of 775 K and 45 m/s.....	134

Figure 5.57. Temperature power spectra calculated from Rayleigh temperature and density data acquired in the shear layer of a flow with maximum temperature and velocity of 775 K and 45 m/s	134
Figure 5.58. Velocity power spectra calculated from Rayleigh data acquired in the shear layer of a flow with maximum temperature and velocity of 775 K and 45 m/s and hotwire data acquired in a room temperature flow with similar maximum velocity.....	135
Figure 5.59. Mean density profile calculated from time-resolved Rayleigh data and measured by a thermocouple for a flow with maximum temperature and velocity of 775 K and 45 m/s	136
Figure 5.60. Density fluctuation profile calculated from Rayleigh measurements in a flow with maximum temperature and velocity of 775 K and 45 m/s	136
Figure 5.61. Mean temperature profile calculated from time-resolved Rayleigh data and measured by a thermocouple for a flow with maximum temperature and velocity of 775 K and 45 m/s	137
Figure 5.62. Temperature fluctuation profile calculated from Rayleigh measurements in a flow with maximum temperature and velocity of 775 K and 45 m/s.....	137
Figure 5.63. Mean velocity profile calculated from time-resolved Rayleigh data and pitot tube measurements in a flow with maximum temperature and velocity of 775 K and 45 m/s	138
Figure 5.64. Velocity fluctuation profile calculated from Rayleigh measurements in a flow with maximum temperature and velocity of 775 K and 45 m/s and hotwire measurements in a room temperature flow with similar maximum velocity.....	138
Figure A.1. Rotational Raman spectrum for a gas that is composed of 80% N ₂ and 20% O ₂ at room temperature and atmospheric pressure calculated by the CARSFIT code. The individual contributions from O ₂ and N ₂ are shown in green and red, respectively	147
Figure A.2. Rotational Raman shifts closest to the excitation laser frequency for a gas that is composed of 80% N ₂ and 20% O ₂ at temperatures of 300 K and 775 K and atmospheric pressure calculated by the CARSFIT code.....	147
Figure A.3. Rotational Raman lines relative to the Rayleigh line. The right and left wings of the Raman spectral lines are identified as the rotational Stokes and anti-Stokes branches, respectively.	148

Figure B.1. Poisson and Gaussian distributions for $\mu = 25$	150
Figure B.2. Fractional uncertainty $\frac{\sqrt{\mu}}{\mu}$ as a function of mean number of counts μ ..	150
Figure D.1. Numerical Simulation Algorithm	161
Figure F.1. Time resolved Rayleigh velocity data for experiment 3 (case 1) and a radial position of 0 mm. The linear curve fit shows a drift in mean velocity from 36.5 m/s to 30 m/s over the 10 second data acquisition time	172
Figure F.2. Time resolved Rayleigh velocity data for experiment 3 (case 1) and a radial position of -1 mm. The linear curve fit shows a drift in mean velocity from 34.5 m/s to 39.2 m/s over the 10 second data acquisition time	172
Figure F.3. Frequency drift data for the Coherent 10 Watt Verdi laser over a 30 minute period during which the stabilization feedback system is cycled on and off for several minutes at a time	174
Figure F.4. Frequency drift of the Coherent 10 Watt Verdi laser in the 10 minute interval from 17 to 27 minutes shown in figure F.3 during which the Fabry-Perot stabilization is deactivated for the first 5 minutes and is active for the latter 5 minutes. This plot demonstrates the 30 second oscillation period of the laser.....	175

ACKNOWLEDGEMENTS

I would like to thank my adviser, Dr. Jackie Sung, for all of his advice, direction, and sharing of expertise. I would also like to thank Dr. Dick Seasholtz for teaching me everything I know about Rayleigh scattering. Without his mentoring, friendship, and encouragement this dissertation would not have been possible. I thank Dr. Mark Wernet for numerous discussions that have helped immensely in analyzing and understanding my data and improving experimental setups. He continues to be a source of advice and encouragement in the advancement of my research career. Thanks also to Kristie Elam for helping to set up the experiments, writing the LabVIEW programs for experiment control and data acquisition, and sitting in the dark lab with me for countless hours taking data. I would like to express gratitude to Mike Bronczek for constructing the plumbing systems for the jets, Frank Lam for providing mechanical technician support for this project, and Adam Wroblewski for providing the 3D CAD drawings of my experiment. I thank Prof. Tenti for providing his computer code for the 6-moment Rayleigh scattering model. I would also like to thank the members of my defense committee, Prof. Sung, Prof. Kadambi, Prof. Kamotani, Prof. Edwards, and Dr. Wernet, for their time and effort. I would like to express tremendous appreciation and gratitude to Brad, my family, and all of my friends for their support, love, understanding, and encouragement in completing my dissertation and the rest of the Ph.D. requirements. Brad especially has taken the brunt of my frustrations and stress; I sincerely appreciate his understanding and patience. Special thanks go to Ursula for keeping me company during our study sessions at Starbucks. Finally, I would like to acknowledge the NASA Internal Research & Development (IR&D) Program for funding this work.

NOMENCLATURE

A	amplitude of sine wave
a	most probable molecular speed (m s^{-1})
c	speed of light ($= 2.998 \times 10^8 \text{ m s}^{-1}$)
d	Fabry-Perot mirror spacing (m)
d_{beam}	output laser beam diameter (m)
d_{PV}	diameter of focused laser beam (m)
\vec{E}	incident electric field vector (V m^{-1})
F	Fabry-Perot instrument function contrast
f	frequency of scattered light (s^{-1})
$f\#$	focal length of lens divided by the lens diameter
f_0	frequency of incident laser light (s^{-1})
f_{fund}	fundamental frequency (s^{-1})
f_C	collimating lens focal length (m)
f_L	fringe forming lens focal length (m)
f_s	sampling rate (s^{-1})
h	Planck's constant ($= 6.626 \times 10^{-34} \text{ N m s}$)
I_0	Incident light wave intensity ($\text{J s}^{-1} \text{ m}^{-2}$)
I_{FP}	Fabry-Perot instrument function
\vec{K}	interaction wave vector (m^{-1})
K	magnitude of \vec{K} (m^{-1})
\vec{k}_0	incident light wave vector (m^{-1})

\vec{k}_s	scattered light wave vector (m^{-1})
L	length of sub-records in spectral calculations
L_x	probe volume length (m)
l_m	mean free path between molecular collisions (m)
m	molecular mass (kg)
N_e	effective finesse
N_k	photoelectron counts in Rayleigh spectrum over the frequency range f_k to $f_k + \Delta f$
N_q	photoelectron counts in q^{th} annular region
N_R	Rayleigh scattered photoelectrons collected into solid angle Ω
N_r	reflective finesse
n	molecular number density (m^{-3})
P_0	power of incident laser beam (J s^{-1})
P_s	scattered power (J s^{-1})
p	static pressure (N m^{-2})
q	annular region number
R	Fabry-Perot mirror reflectivity
r	radial position in image plane (m)
r_{max}	fiber face image radius (m)
$r_{i,q}$	inner radius of q^{th} annular region (m)
$r_{o,q}$	outer radius of q^{th} annular region (m)
r_R	fringe radius for reference laser light (m)
S_R	Rayleigh scattering spectrum
T	static temperature (K)

u_k	measured velocity component (m s^{-1})
\vec{v}	velocity vector (m s^{-1})
x_f	non-dimensionalized frequency
y	y -parameter
β	angle between \vec{E} and scattering plane (rad)
β_i	unknown parameters in maximum likelihood estimation
Γ	Fisher information matrix
Δr	width of annular region (m)
Δt	integration time (s)
ε	optical system efficiency
η	dynamic viscosity (N s m^{-2})
θ	angle between light ray and optical axis (rad)
θ_R	angle between reference ray and optical axis (rad)
κ	Boltzmann's constant ($= 1.381 \times 10^{-23} \text{ J K}^{-1}$)
Λ	wavelength corresponding to wave vector \mathbf{K} (m)
λ	illumination wavelength (m)
μ	refractive index
ρ	gas density (kg m^{-3})
σ_ρ	uncertainty in density estimate (kg m^{-3})
σ_T	uncertainty in temperature estimate (K)
σ_{u_k}	uncertainty in velocity estimate (m s^{-1})
$\frac{d\sigma}{d\Omega}$	differential scattering cross-section ($\text{m}^2 \text{ sr}^{-1}$)

χ_s	scattering angle (rad)
ψ	phase change between successive reflections
Ω	solid angle (sr)
ω_1	pump frequency (rad s ⁻¹)
ω_2	Stokes frequency (rad s ⁻¹)
ω_3	CARS signal frequency (rad s ⁻¹)

Development of a Molecular Rayleigh Scattering Diagnostic for Simultaneous Time-Resolved Measurement of Temperature, Velocity, and Density

Abstract

by

AMY FLORENCE MIELKE

The scope of this dissertation is to develop and apply a non-intrusive molecular Rayleigh scattering diagnostic that is capable of providing time-resolved simultaneous measurements of gas temperature, velocity, and density in unseeded turbulent flows at sampling rates up to 32 kHz. Molecular Rayleigh scattering is elastic light scattering from molecules; the spectrum of Rayleigh scattered light contains information about the gas temperature and velocity of the flow. Additionally, the scattered signal is directly proportional to the molecular number density. These characteristics are utilized in the development of the measurement technique.

This dissertation results in the following:

1. Development of a point-based Rayleigh scattering measurement system that provides time-resolved simultaneous measurement of temperature, velocity, and density at sampling rates up to 32 kHz.
2. Numerical modeling of the light scattering and detection process to evaluate uncertainty levels and capabilities of the measurement technique.

3. Validation of the developed measurement system in benchmark flow experiments in which velocity and temperature fluctuations were decoupled and independently forced at various amplitudes and frequencies.
4. Demonstration of simultaneous measurement of all three quantities in an electrically-heated free jet facility at NASA Glenn Research Center.
5. Comparison of Rayleigh scattering measurements in all experiment phases with thermal anemometry measurements.

The experimental measurements are presented in terms of first-order time-series results that are measured directly by the technique, and second-order statistics, such as power spectral density and rms fluctuations, which are calculated from the direct time-resolved quasi-instantaneous measurements. Temperature fluctuation results are compared with constant current anemometry measurements and velocity fluctuation results are compared with constant temperature anemometry measurements. Experiments were performed in air flows with densities ranging from 0.45 to 1.15 kg/m³, temperatures from 295 K to 775 K, and velocities from 0 to 110 m/s. Accuracies of 0.02 kg/m³, 5 - 12 K, and 4 - 10 m/s in the mean density, temperature, and velocity measurements were demonstrated, respectively. Fluctuation amplitude measurements of density, temperature, and velocity in the ranges of 0.02 – 0.125 kg/m³, 5 – 60 K, and 10 – 20 m/s with accuracies better than 0.01 kg/m³, 3 K, and 7 m/s were achieved, respectively.

CHAPTER 1

INTRODUCTION

1.1 Introduction and motivation

Currently, non-intrusive temperature measurement techniques available for use in turbulent flow studies where the local pressure is unknown are limited to sampling rates less than a few kHz. There are also no techniques that can provide non-intrusive time-resolved measurement of gas temperature, velocity, and density simultaneously at rates beyond a few kHz. Conventional intrusive measurement devices such as resistance wires, pressure probes, and thermocouples are usually limited in spatial and temporal resolution, disturb the flow under study, and can be damaged by high pressure or temperature. Therefore, a non-intrusive molecular Rayleigh scattering technique is developed to measure time-resolved gas temperature, velocity, and density in unseeded gas flows at sampling rates up to 32 kHz.

The Rayleigh scattering technique presented is unique in that it provides simultaneous temperature, velocity, and density measurements at sampling rates up to 32 kHz. A high power single-frequency continuous-wave (cw) laser beam is focused at a point in an air flow field and Rayleigh scattered light is collected and transmitted via optical fiber to another location where the light is spectrally resolved. The signal strength and spectrum of the light contain information about the density, temperature, and velocity of the flow. A planar mirror Fabry-Perot interferometer (FPI) is used to analyze the spectrum of the scattered light, and photomultiplier tubes (PMTs) record the signal strength and fringe

intensity pattern at high sampling rates enabling time-resolved measurement of the gas flow properties.

1.2 Mission requirements and objectives

The scope of this dissertation is to develop and apply a non-intrusive molecular Rayleigh scattering diagnostic that is capable of providing point-wise time-resolved simultaneous measurements of gas temperature, velocity, and density in unseeded gas flows at sampling rates up to 32 kHz. The Rayleigh scattering measurement system will be validated in benchmark flow experiments in which velocity, temperature, and density fluctuations are induced. After the ability of the system to provide fluctuation measurements is evaluated, and range and accuracy limitations of the technique are determined, the Rayleigh scattering diagnostic will be used to characterize an air flow issuing from an electrically-heated jet equipped with a 1-cm diameter nozzle that can provide flow velocities up to 110 m/s and temperatures up to 775 K. The Rayleigh scattering measurements will be compared with constant current anemometry (CCA) and constant temperature anemometry (CTA) measurements. Numerical modeling of the light scattering and detection process will be validated by comparison with experiments and will be used to further evaluate the abilities of the measurement technique in flow regimes that are of interest to fluid dynamics and aero-acoustic researchers, including flow regimes outside of those studied in this dissertation since the technique is capable of operating over a wide range of flow conditions.

1.3 Application and relevance to the scientific community

The ability to obtain dynamic high frequency response measurements of multiple properties simultaneously is a valuable tool for compressible, turbulent flow research. It is often necessary to resolve the short time scales of turbulent flow processes. Dynamic flow measurements are particularly useful to aeroacoustics researchers who are interested in correlating flow property fluctuations with far field acoustic fluctuations, leading to validation and improvement of computational aeroacoustics (CAA) noise prediction codes. Knowledge of velocity-temperature fluctuation correlations and turbulent Prandtl number are also needed to improve computational fluid dynamic (CFD) models of compressible turbulent flows. The ability to route the signal, and potentially the incident illumination, via fiber optics makes this technique appealing to facilities researchers who typically require flow measurements in harsh environments with tight space constraints.

In response to NASA's mission to reduce aircraft noise levels, experiments are currently in progress to evaluate the contribution of temperature fluctuations to far-field noise by application of the presented Rayleigh scattering technique in the Small Hot Jet Acoustic Rig (SHJAR), which is a heated nozzle facility located in the AeroAcoustic Propulsion Laboratory (AAPL) at NASA Glenn Research Center (GRC). This facility can provide up to Mach 2 flow conditions with maximum temperatures approaching 970 K. Sound pressure fluctuation (microphone) measurements will eventually be acquired simultaneously with Rayleigh measurements allowing correlation between flow property fluctuations and noise generation. Determining sources of jet noise will help engineers to

design quieter, more efficient aircraft. Unfortunately, the testing in this facility will not be completed in time for inclusion in this dissertation.

1.4 Overview of optical flow diagnostic techniques

Various optical techniques are available for temperature, molecular number density, and velocity measurements. Eckbreth (1996) provides the details of several techniques, such as Coherent Anti-Stokes Raman Spectroscopy (CARS), Spontaneous Raman and Rayleigh scattering, and Laser-Induced Fluorescence (LIF), with an emphasis on their use in combustion applications. Other techniques that have been used for flow measurements in various environments include laser-induced gratings (Cummings, 1995; Hart, 1999), Laser-Doppler Velocimetry (LDV) (Tropea, 1995), filtered Rayleigh scattering (Boguszko & Elliott, 2005), collective light scattering (Bonnet et al., 1995), Particle Image Velocimetry (PIV) (Wernet, 2007), Planar Doppler Velocimetry (PDV) (Samimy & Wernet, 2000), and molecular flow tagging techniques (Koochesfahani, 1999). However, none of these techniques can provide high frequency response measurement of all three flow properties simultaneously beyond a few kHz. Brief descriptions of each of these techniques are provided in this section. They are separated into two main categories: molecular-based techniques and particle-based techniques. A category of hybrid techniques that implement multiple techniques simultaneously to obtain additional flow information is also presented.

1.4.1 Molecular-based techniques

A class of flow measurement techniques that involved either elastic (non-energy-exchanging) or inelastic (energy-exchanging) scattering processes from atoms or molecules are described in this section. These techniques are free of problems associated with seeding flows with particulates, such as abrasiveness to equipment and difficulties with achieving proper flow seeding conditions. Since the gas molecule properties are directly determined, these techniques are capable of providing gas temperature and density information not available in particle-based techniques.

1.4.1.1 Raman scattering

Spontaneous Raman scattering is the inelastic incoherent scattering that results in energy exchange between photons and the internal energy modes of molecules and is termed rotational, vibrational, or electronic depending on the type of energy exchange that occurs. In this diagnostic a single laser can be used to monitor all species, regardless of wavelength. In stimulated Raman scattering the incident illumination is tuned to resonances of specific species, usually for the purpose of increased signal strength; however this limits the technique to probe only those species with resonances at the incident frequency (Ahn et al., 2005). The Raman spectral signature is fit to a spectral model to back out the temperature and species concentration measurements. For a more detailed discussion of the phenomena and how it is used in combustion diagnostics refer to Eckbreth (1996). The strength of the scattering scales as the 4th power of the scattering frequency; however even at short wavelengths the signal is very weak because of lower incident laser power at 2nd and 3rd harmonic output and is often corrupted by interference

from flame and background luminosity. The uncertainty in the measurements is dependent on the signal-to-noise and the cleanliness of the flow. This technique is limited to non-sooty flames since the pulsed laser energy may heat the soot particles causing incandescence, which also interferes with the Raman signal. Various applications include the study of clean flames (Kojima & Nguyen, 2004; Toro et al., 2005), measurements in a gas turbine model combustor at elevated pressures (Wehr et al., 2007), atmospheric temperature measurements (Vaughan et al., 1993), and measurements in a plasma wind tunnel facility (Studer & Vervisch, 2007), to name a few.

1.4.1.2 Coherent Anti-Stokes Raman Spectroscopy (CARS)

Coherent anti-Stokes Raman spectroscopy, which is a type of stimulated Raman scattering, is described in detail in Eckbreth's book on combustion diagnostics (1996). Laser beams at frequencies ω_1 (pump frequency) and ω_2 (Stokes frequency) are "mixed" through a geometric phase-matching scheme in which the beams are crossed and focused at the measurement point creating a probe volume typically on the order of $0.2 \times 0.2 \times 2 \text{ mm}^3$. The laser interaction with the medium causes an oscillating polarization at a third frequency ($\omega_3 = 2\omega_1 - \omega_2$) generating a coherent CARS signal or beam. The pump and Stokes beams are shifted in frequency by the vibrational/rotational Raman shift of the molecule(s) of interest. Changing ω_1 and ω_2 allows one to probe different molecules in the flow. Laser sources with pulse durations on the order of 10 ns are used to obtain instantaneous measurements of temperature and species concentration based on the shape of the spectral signature and the intensity of the CARS signal. Due to its high signal conversion efficiency and coherent nature, the CARS signal is orders of magnitude more

intense than the spontaneous Raman signal; however it lacks the advantage of probing all species simultaneously with a single laser source. Many variations of the technique have been developed, such as dual-pump, dual-Stokes, or dual-broadband CARS, which employ some combination of multiple lasers with varying frequencies and linewidths to probe rotational and ro-vibrational transitions of multiple species simultaneously (O'Byrne et al., 2004; Roy et al., 2003; Roy et al., 2004). CARS is most applicable in combustion environments with moderate pressures and where desired species concentrations are on the order of 0.1% and greater. For trace level concentrations (ppm level) LIF techniques are more useful. The accuracy of CARS temperature measurements varies depending on the experiment; typically higher accuracies are obtained at higher temperatures. Standard deviations in single-shot temperature measurements of 2.3% to as much as 12% have been reported (Roy et al., 2004; O'Byrne et al., 2004).

1.4.1.3 Laser-Induced Fluorescence (LIF)

Laser-Induced Fluorescence and planar LIF (PLIF) techniques have been used for both qualitative flow visualization, as well as quantitative measurements of species concentration, temperature, velocity, and pressure (Eckbreth, 1996). LIF techniques usually require a pulsed, tunable wavelength laser source. When the laser wavelength is resonant with an optical transition of a species in the flow some of the laser light is absorbed, exciting the molecules or atoms to higher electronic energy states resulting in re-emission of light at a different wavelength from the incident illumination, referred to as fluorescence. The spectral properties of the fluorescence are dependent on the temperature, pressure, velocity, and species concentration of the flow field. The

fluorescence signal is incoherent and unpolarized. Species concentration is proportional to the intensity of the fluorescence signal; temperature is determined either from the relative signal of two transitions or the line-shape of a single transition; and pressure is determined by measuring the pressure-dependent transition broadening.

The velocity component along the beam propagation axis can be determined by measuring the Doppler shift of the fluorescence signal frequency relative to a reference signal frequency in a stationary flow. The frequency shift $\Delta\omega$ experienced by the light is a function of the velocity vector \vec{v} and the interaction wave vector \vec{K} :

$$\Delta\omega = \frac{1}{2\pi} \vec{v} \cdot \vec{K} \quad (1-1)$$

where the interaction wave vector defines the direction of the velocity component being measured and is the bisector of the incident and scattered light wave vectors \vec{k}_0 and \vec{k}_s , respectively (figure 1.1):

$$\vec{K} = \vec{k}_s - \vec{k}_0 \quad (1-2)$$

This concept is the same for all Doppler shift velocity measurements, although the technique for determining the magnitude of the frequency shift may vary.

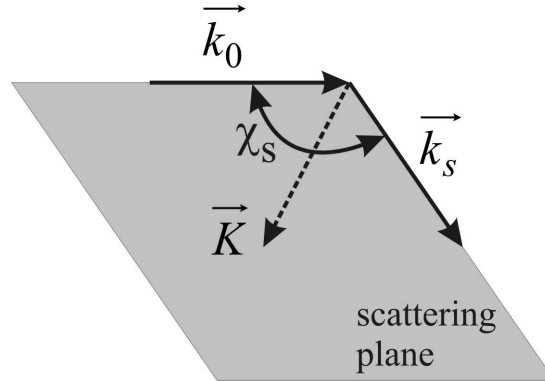


Figure 1.1. Scattering vector diagram. The incident wave vector is \vec{k}_0 and the scattered wave vector propagating to the detector is \vec{k}_s where χ_s is the scattering angle. These two vectors define an interaction vector in the direction $\vec{K} = \vec{k}_s - \vec{k}_0$ that defines the measured velocity component direction. The plane defined by these vectors is referred to as the scattering plane.

The fluorescence signal is usually recorded by photomultiplier tubes for point measurements or charge-coupled devices (CCDs) for planar measurements. Filtering is often necessary to eliminate stray laser light and background light. The time resolution of this technique is limited by the pulse duration and frequency of the pulsed laser source, as well as the lifetime period of the fluorescence, which typically ranges between nanoseconds and milliseconds.

Fluorescence from naturally occurring tracers is used when available, such as OH and NO (McMillin et al., 1994; Palmer & Hanson, 1996). Seeding the flow with a tracer gas or species, such as acetone or iodine (I_2), is a technique often employed to obtain temperature measurements (Thurber et al., 1997; Thurber et al., 1998). Acetone and OH PLIF have been used to study mixing in reacting flows (Miller et al., 1998). Planar time-averaged (averaged for 20-75 seconds) measurements of velocity and temperature in a

low temperature I₂-seeded N₂ hypersonic free jet facility were performed using PLIF to study boundary layers on a sharp leading edge flat plate with impinging Mach 12 rarefied flow (Cecil & McDaniels, 2005). Fluorescence signals were recorded from the hypersonic flow region and from a reference static I₂ cell. Non-linear least squares regression was performed to extract temperature measurements from the fluorescence lineshape, while velocity was measured based on the frequency shift between the flow and reference signals.

Two-line PLIF, where two lasers at different wavelengths are used to excite the molecules or atoms, or two-color PLIF, where two spectral bands of the same dye are measured, as well as single-wavelength PLIF have been used to provide low temporal resolution instantaneous two-dimensional temperature measurements in combusting environments (Giezendanner-Thoben et al., 2005) as well as liquid flows (Bruchhausen et al., 2005). Recent advances in laser and detector technologies have enabled higher temporal resolution measurements in many optical diagnostic areas. Paa et al. (2007) used a tunable, thin-disk laser with a 1 kHz repetition rate and pulse energies in the 5 mJ range to excite and measure turbulence of OH radicals. Dec and Keller (1990) used a detection method similar to that employed in the work of this dissertation whereby a continuous-wave (cw) laser is used in conjunction with high efficiency fast response time detectors to obtain high frequency response measurements. They performed a two-line atomic fluorescence technique using this concept to provide point-wise time-resolved temperature measurements at a sampling rate of 2 kHz. Jiang (2006) demonstrated NO PLIF imaging at > 100 kHz repetition rate in a Mach 2 jet using a megahertz repetition

rate pulse-burst laser system developed at the Ohio State University in combination with a Princeton Scientific Instruments ultra-high frame rate camera.

Common limitations of LIF techniques are that only molecular or atomic species that have optical resonances accessible by available laser wavelengths can be measured. Temperature measurements typically require two laser sources or tuning of a single laser source to access dual transitions. Velocity measurements are really only practical for very high velocity flows ($\text{Mach} \geq 1$). The signal-to-noise is limited by detector shot noise and the signal is subject to interference from fluorescence of other species. Uncertainty in instantaneous temperature measurements of 3-10% are typical and averaging many snapshots can reduce the uncertainty to less than 1%.

1.4.1.4 Laser-induced gratings

Laser-induced gratings are used in point-wise, unseeded techniques that have the potential to measure instantaneous temperature, velocity, and species concentrations. Cummings (1995) exploited laser-induced gratings for gas-phase flow property measurements as reported in his Ph.D. dissertation research in which he coined the technique as Laser-Induced Thermal Acoustics (LITA). Laser-induced grating techniques have been referred to by several other names, such as Transient Grating Spectroscopy (TGS) or Laser-Induced Grating Spectroscopy (LIGS). These techniques excel at high pressures and collision rates where other techniques are invalid. A short-pulse pump, or excitation, laser is split into two beams which are crossed at some angle. Interference between the two beams creates an electric field grating, which results in a density

perturbation, and hence a refractive-index grating, caused by molecular mechanisms of electrostriction and thermalization (Hart et al., 1999). If the two excitation beams differ in frequency a propagating “transient” or “dynamic” grating will result. The grating is illuminated by a long-pulse or cw probe laser at the Bragg phase-matching angle (relative to the bisector of the pump beams). Part of the probe beam is coherently scattered producing the signal beam. If the frequencies of the three incident and the generated beams or waves are equal, the process is called “degenerate” and is referred to by the term degenerate four-wave mixing (DFWM) (Eichler, 1986). The signal beam is detected at high temporal resolution by a PMT or some other optical detector. The modulation frequency of the signal intensity and the fringe spacing of the grating are used to provide speed of sound measurements in the gas; if this is an ideal gas, this also provides gas temperature measurements.

Researchers have used both nonlinear fitting to theoretical models, as well as frequency decomposition techniques to extract the temperature information from the TGS signal. The signal has the potential to provide information about flow velocities and other transport properties as well. Measurement of the signal modulation due to the Doppler effect using a heterodyne detection scheme can provide velocity information in gas flows (Schlamp et al., 2000b; Kozlov et al., 2000). The thermal diffusivity can be evaluated from the exponential decay of the LITA signal (Schlamp et al., 2000a; Cummings et al., 1995). Li et al. (2002) also investigated the use of TGS for measuring acoustic damping rates at elevated pressures, with the intended application of distinguishing between types of gas mixtures so as to determine the state of a combustion process. Single-shot

measurements of speed of sound and thermal diffusivity were reported by Schlamp et al. (2000a) with errors of 0.03%-0.25% and 1-5%, respectively, depending on signal intensity. This work continued with the addition of simultaneous velocity measurement by homodyne (Schlamp et al., 1999) and heterodyne (Schlamp et al., 2000b) detection methods. Schlamp et al. (2000b) reported uncertainties of 0.2 m/s and 0.5% in the velocity and sound speed measurements, respectively, in NO₂-seeded air in a low-speed wind tunnel up to Mach 0.1.

Stampanoni-Panariello et al. (1998) demonstrated temperature measurements using non-resonant laser-induced electrostrictive gratings (LIEG) in a furnace with air temperatures up to 1370 K at atmospheric pressure, and in methane/air, hydrogen/air, and carbon monoxide/air flames exhibiting temperatures up to 2600 K at atmospheric pressure. They presented results with single-shot measurement errors as high as 5% in the furnace experiment. Kozlov et al. (2000) presented a measurement approach to obtain flow velocities using a heterodyne detection LIEG technique and Hemmerling et al. (2000) extended this work by demonstrating simultaneous temperature and velocity measurements in a submerged air jet with temperatures in the range 295-600 K and velocities in the range 10-100 m/s. The movement of the grating caused by the flow velocity causes a frequency shift in the signal beams due to the Doppler effect. High frequency modulation in the signal is related to the speed of sound in the gas while low frequency modulation is related to the flow velocity. Several other research groups have made significant contributions to optical diagnostic research in the area of laser-induced gratings as well (Barker et al., 1999; Paul et al., 1995). Disadvantages of laser-induced

grating techniques include complexity of the setup (2-3 laser beams needed), limited temporal response (limited to laser pulse rate), limited spatial resolution (dependent on how small the grating can be made), and directional ambiguity in the velocity measurement.

1.4.1.5 Molecular tagging techniques

Molecular tagging techniques are a class of flow tagging velocimetry diagnostics in which a line or pattern is written into the flow by means of an optical resonance, and, after a time delay the displaced line or pattern is interrogated using fluorescence or phosphorescence to provide velocity measurements via time-of-flight. This class of techniques is usually considered the molecular counterpart of particle image velocimetry. There are many molecular tagging methods using different tracers and excitation methods. An overview of this class of techniques by Koochesfahani (1999) discusses the various tagging approaches. The molecular tracers may be naturally occurring in the flow or may be artificially seeded into the flow of interest. In one version referred to as Molecular Tagging Velocimetry (MTV) the flow is seeded by molecular tracers, such as biacetyl, which are excited by a pulsed laser source causing fluorescence or phosphorescence to occur. The phosphorescence signal has a significantly longer lifetime than the fluorescence signal and therefore is the signal utilized in this technique. The region of the flow must be illuminated by a grid of intersecting laser lines to allow multi-point two-component velocity measurements. The molecular motion is imaged at some time delay relative to the initial laser pulse. A spatial correlation using a sub-region of the image surrounding each grid intersection is performed between the reference laser image

and the phosphorescence image to provide the displacement vector of the molecular tracers, and hence the spatial average of the velocity within the sub-region. Most of the work in this field has been in liquid flows (Lempert et al., 1993; Koochesfahani et al., 1996); however more recently it has been demonstrated in gaseous flows at very low velocities (~ 10 m/s) (Stier & Koochesfahani, 1999), as well as high speed flows up to Mach 2 (Lempert et al., 2003). Gas flow measurements using MTV are limited by available tracers. A commonly used gaseous flow tracer (biacetyl) experiences extinction of its phosphorescence signal in the presence of oxygen and therefore can only be used in oxygen-free environments. Recent advances of the technique have taken advantage of the temperature dependence of the phosphorescence lifetime to provide simultaneous temperature measurements via a ratio of intensities during two delayed integration times within the phosphorescence lifetime. The Molecular Tagging Velocimetry and Thermometry (MTV&T) technique has been demonstrated in the wake of a heated cylinder in a water channel where accuracies of 2.5% and 0.1°C were reported for the instantaneous velocity and temperature measurements, respectively (Hu & Koochesfahani, 2006).

Raman Excitation and Laser Induced Electronic Fluorescence (RELIEF) is a molecular oxygen-based flow tagging method in which two co-linear or co-planar laser pulses whose frequencies differ by the vibrational frequency of oxygen induce stimulated Raman excitation to “tag” the flow. The interrogation laser pulse which causes the vibrationally excited oxygen molecules to fluoresce is typically provided by an ArF excimer laser. Alternative tagging and interrogation wavelengths have been investigated

to eliminate the need for the ArF laser, as it is not very portable and requires the use of toxic gases (Lempert et al., 2006). Tracking the molecular motion by fluorescence imaging allows measurement of flow velocities, as well as diffusion and transport properties of the molecules. The vibrational lifetime of oxygen is sufficiently long and the signal is strong enough to make this technique useful over a wide range of flow conditions; however this technique typically suffers in the presence of humidity. Miles et al. (2000) applied RELIEF in a wind tunnel operated over the range Mach 0.08 to 0.8 as well as in the study of mixing of Helium and air in a co-flowing jet at Mach 1.8 and reported accuracies in the instantaneous velocities of 0.5% or less. Miles et al. (1993) measured the diffusion rate of the vibrationally excited oxygen molecules in air at temperatures up to 362 K, from which they extracted instantaneous temperature measurements.

Several flow tagging techniques take advantage of atoms or molecules that are naturally present in the flow. Two such techniques are Ozone Tagging Velocimetry (OTV) and Hydroxyl Tagging Velocimetry (HTV). In OTV a 193 nm laser pulse induces photodissociation of O_2 and subsequent chemical formation of O_3 (ozone) to write the pattern in the flow. A 248 nm laser pulse photodissociates O_3 and fluoresces the vibrationally-excited O_2 product to interrogate the flow displacement. O_3 produced from O_2 is relatively long-lived and insensitive to the presence of water vapor providing an alternative to RELIEF which is limited to high-speed dry flows and MTV which is limited to oxygen-free environments. Pitz et al. (1998) used OTV for velocity measurements in room temperature air flows and showed through modeling of ozone

concentrations that the technique is applicable at pressures and temperatures expected in aeromechanical testing of jet engines. In HTV an ArF laser photodissociates water to produce OH and the movement of the pattern is interrogated at some time later using LIF. A 7×7 grid pattern was used to provide 49 velocity vectors in an air nozzle and a hydrogen/air flame (Ribarov et al., 2004). Lahr et al. (2006) demonstrated the technique using an 11×11 grid pattern yielding 120 velocity vectors in a Mach 2 scramjet combustor with a wall cavity flameholder under non-reacting low- and high-backpressure conditions.

1.4.1.6 Rayleigh Scattering

Rayleigh scattering is the elastic scattering of light from molecules, or particles with dimensions much smaller than the wavelength of the light, where the signal strength, Doppler frequency shift, and spectral linewidth of the scattered light provide measurements of density, velocity, and temperature, respectively. Since no energy exchange takes place between the photons and molecules, any laser frequency is applicable, although shorter wavelengths are typically desired since the scattering strength scales by λ^{-4} . Miles et al. (2001) provide a review of Rayleigh scattering principles and techniques. In a non-spectroscopic approach, Rayleigh scattering has been used to measure density and temperature in flames by a direct intensity measurement and applying the ideal gas law; however assumptions must be made about the local gas composition and pressure in this type of work. Unlike Raman scattering, the Rayleigh signal is not species specific and therefore cannot provide individual species concentrations or mole fractions; however the gas composition does affect the Rayleigh

signal and must be known in order to provide quantitative gas density and temperature measurements. Also, this non-spectroscopic approach requires that the molecular scattering cross-section does not vary greatly in the flow and it is only applicable in clean (non-sooting) flames. One example of such work is an experiment in which two-point temperature measurements were made at a rate of 10 kHz in a turbulent non-premixed jet flame at a Reynolds number of 15,200 using a pulsed Nd:YAG laser (Wang et al., 2005).

Rayleigh techniques that take advantage of the spectral content of the scattered light to provide flow measurements do so in a variety of ways. Typical Rayleigh linewidths are on the order of a GHz; hence a very narrow linewidth laser (~ 5 MHz), usually one equipped with an etalon to operate in a single axial mode, and an extremely high resolution filter are required to resolve the spectrum. The most common techniques involve either the use of atomic or molecular absorption filters (filtered Rayleigh scattering) or filters based on interference phenomena, such as the Fabry-Perot etalon (interferometric Rayleigh scattering) to resolve the spectrum of the light. Atomic or molecular absorption filters that have a sharp edge and smooth transition between their minimum and maximum transmission are useful for measuring the frequency shifts and spectral linewidths typically encountered in molecular scattering experiments. Iodine vapor filters are often used because of their strong absorption features in the visible with transitions from strong absorption to full transmission for frequency ranges of ± 1 GHz (± 0.03 cm⁻¹). Forkey et al. (1997) developed a computational code to calculate the iodine absorption profiles, such as the one shown in figure 1.2.

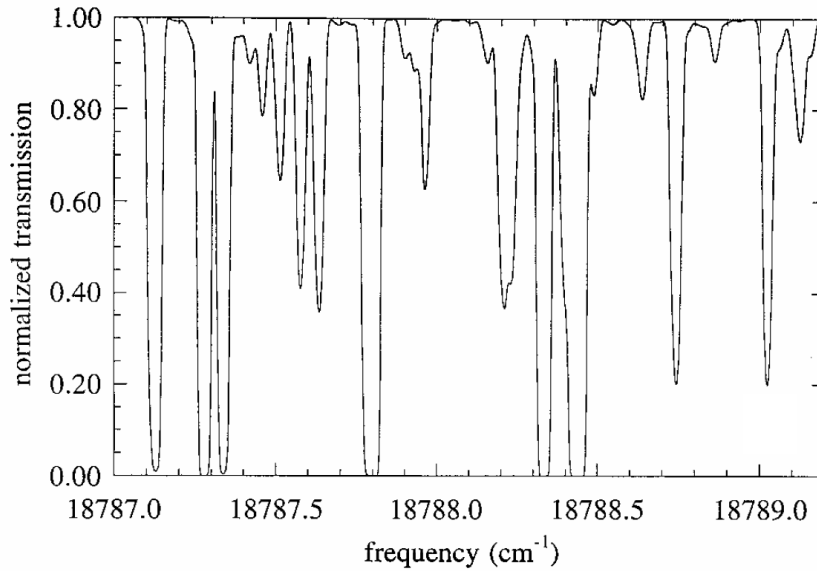


Figure 1.2. Transmission profile of an iodine vapor absorption filter near 532 nm wavelength. This plot was taken from Forkey et al. (1997).

In one version of filtered Rayleigh scattering, the laser frequency is scanned while the scattered light is imaged through an iodine vapor cell. The transmission profile is a convolution of the filter's absorption spectrum and the Rayleigh lineshape. Numerical models of the absorption spectrum and the Rayleigh spectrum are used to deconvolve the signal and provide measurements of velocity, temperature, and pressure. This technique was used to provide planar measurements in a Mach 2 free jet with uncertainties of 2% - 3% in velocity, 2% in temperature, and 4% - 5% in pressure (Forkey et al., 1998). In another version referred to as filtered angularly resolved Rayleigh scattering (FARRS) the scattered light from a single-frequency laser source is collected over a solid angle of ± 20 degrees and imaged through an iodine absorption filter into a narrow line on an intensified CCD camera. The filtered signal is absorbed with varying strength over the collection angle range. An unfiltered reference image is acquired on the same detector. The unfiltered image provides fluid density measurement. The observation angle and

fluid property dependence of the scattering spectrum are used to provide instantaneous pressure, temperature, and streamwise velocity by fitting the signal to a scattering model. Relative errors in temperature and pressure were reported as 1.6% - 2.9% and 5.9% - 9.6%, respectively, based on a free jet experiment and an energy deposition experiment. The velocity measurement uncertainty was 7 m/s in a 242 m/s flow and 6.3 m/s in a flow that was practically at rest (Boguszko & Elliott, 2005). Molecular filters have also been used as a means of background suppression in light scattering experiments. For example, a Light Detection and Ranging (LIDAR) system used atomic vapor filters to remove scattering from aerosols in the atmosphere and analyze light scattered from molecules for atmospheric temperature measurements (Shimizu et al., 1986). Molecular filters are also useful for filtering laser light scattered from surfaces in Rayleigh scattering experiments in wind tunnels or other enclosed experiment chambers (Seasholtz et al., 1997).

Interferometric Rayleigh scattering, which is the approach taken in this dissertation, utilizes a Fabry-Perot etalon to resolve the Rayleigh lineshape. A Fabry-Perot etalon consists of two parallel planar reflective plates or surfaces and is typically used in the imaging mode (constant spacing between plates) for interferometric Rayleigh scattering (Vaughan, 1989). An etalon may be air-spaced or consist of a solid transparent optical material. When light is imaged through the etalon an interference pattern results which is a function of the spectrum of the light convolved with the instrument function of the Fabry-Perot. The Fabry-Perot instrument function is the well-known airy pattern. A model function utilizing a Rayleigh spectrum model and the airy pattern function is fit to the recorded interference pattern to provide temperature and velocity measurements.

Spatially-resolved measurements can be obtained by imaging scattered light from a laser line or sheet directly through the etalon (Seasholtz et al., 1997; Bivolaru, 2006). Using an optical fiber to collect and transmit the scattered light to the interferometer and detection equipment provides measurements at a point or a finite distance (on the order of 0.5 – 1.0 mm) along a focused laser beam. Previous works using fiber optics in molecular Rayleigh scattering experiments to make time-averaged temperature, velocity, and number density measurements in harsh environments (Seasholtz & Greer, 1998; Panda & Seasholtz, 1999; Mielke et al., 2005), and dynamic density and velocity measurements in supersonic free jets (Seasholtz et al., 2002) have been reported. Rayleigh scattering can be performed using high energy pulsed lasers or high power cw lasers. The uncertainty in the measurements is limited mainly by shot noise; therefore uncertainty increases with decreasing signal strength. Accuracies in mean values are typically within 5% however the uncertainties in instantaneous measurements can be quite a bit higher depending on signal strength. The current dissertation research utilizes a cw laser and fiber optic collection along with photomultiplier tube detectors operated in the photon counting mode to provide point-wise temperature, velocity and density measurements with temporal resolution up to 31.25 μ sec (Mielke et al., 2007).

1.4.1.7 Collective light scattering

Collective light scattering (CLS) is a non-particle laser anemometry technique based on elastic scattering for the special case of scattering from a large collection of molecules where the scattered field is radiated from a fluctuating dielectric medium having scales larger than the mean free path of the atoms or molecules (Bonnet et al., 1995; Lading et

al., 1997). In this special case, the scattered field properties reflect the characteristics of a spatially continuous medium. Propagating and nonpropagating refractive index fluctuations result from sound waves and fluid convection, respectively. This technique requires that the wavelength of the incident light is larger than the mean free path of the atoms or molecules. Incoherent molecular scattering normally has a very broad spectrum due to the thermal velocity of the molecules making it unsuitable for standard laser anemometry where the velocity information is inferred from a cross-correlation function since the spectral broadening may exceed the frequency shift due to the fluid velocity. Coherent collective scattering provides a signal with a much narrower spectral width and greater signal strength than that of the thermally-broadened incoherent molecular scattering spectrum. A hybrid detection scheme proposed by Lading et al. (1997) combines a reference beam Doppler configuration with a time-of-flight anemometer. The correlation function for this technique will generally be asymmetric and will consist of three peaks: two caused by counter propagating fluctuations and one caused by nonpropagating fluctuations. Lading et al. (1997) analyzed the effects of the convection velocity distribution, sound velocity magnitude, and thermal diffusivity on the correlation function. They determined that the peak of the cross-correlation function is a good measure of the mean flow velocity if the turbulence intensity is less than 10%, the sound velocity is at least two times larger than the convection velocity, and the decay caused by thermal diffusion is slower than the time-of-flight. CLS also provides a measure of sound speed via measurement of the 'acoustic' line frequencies corresponding to the propagating sound waves relative to the 'convection' line frequency. Measuring sound speed in addition to the convection velocity allows the calculation of local Mach number

and gas temperature. Bonnet et al. (1995) performed CLS measurements in a supersonic mixing layer and determined mean velocity, Mach number, velocity probability distribution, and mean square density fluctuations within a 60 millisecond time period during which the photodetector signal was processed by the spectrum analyzer to provide the 10 kHz resolution CLS spectrum. They found good agreement between the CLS velocity measurements and conventional particle-based laser Doppler velocimetry measurements.

1.4.1.8 Diode Laser Absorption

Diode laser absorption utilizes the dependence of absorption on temperature and partial pressure of the absorbing gas, via the Beer-Lambert law, to extract line-of-sight (LOS) measurements of flow parameters such as species concentrations, temperature, and pressure. It is also possible to obtain velocity measurements by resolving the Doppler shift of the absorption profiles. Allen (1998) gives an overview of the theory utilized for diode laser absorption sensors, as well as typical measurement strategies and sensor applications. Wavelength multiplexing has made it possible to measure multiple absorption features simultaneously. Gas temperature can be determined from the ratio of absorbance at two different wavelengths. Once temperature is known, the absorption signal at either of the wavelengths can be used to determine the pressure and concentration of individual species. The choice of wavelength is based on where the species of interest has the strongest absorption features. Chang et al. (1991) demonstrated simultaneous measurement of velocity, temperature, pressure and mass flux in a shock tube. A diode laser-based mass flux sensor was developed for subsonic aer propulsion

inlets by Miller et al. (1996). Hanson and Jeffries (2006) review various applications of diode laser sensors to provide kHz rate measurements of gas temperature, pressure, and C_2H_4 concentration in a pulse detonation engine (PDE) using a single laser in a wavelength-scanning approach, and gas temperature and water vapor concentration in a gas turbine sector rig as well as a scramjet test facility using wavelength-multiplexed approaches. Their research group has performed measurements at a wide range of flow conditions with pressures exceeding 40 atm, temperatures exceeding 3000 K, and velocities greater than Mach 3. Ever advancing tunable diode laser technologies allow continual extension and improvement of laser absorption measurement techniques. Due to the robust, low power, and compact nature of these sensors and their ability to provide fast response time measurements of multiple flow quantities, they are very practical for use in a wide variety in-situ diagnostics in propulsion and combustion systems and other ground test applications. Although this technique can provide high frequency response measurements of multiple flow properties it cannot provide the frequency content of the fluctuations since it is a path-integrated measurement.

1.4.2 Particle-based techniques

Particle-based optical flow diagnostics typically provide velocity information only. These techniques involved Mie scattering or elastic scattering from particles whose physical dimensions are larger than the wavelength of light. Due to the large size of the particles compared to molecules, the scattering spectrum does not exhibit thermal broadening and has a narrow linewidth comparable to the linewidth of the incident illumination. The scattered radiation is Doppler shifted in frequency, just as in elastic scattering from

molecules. These techniques measure the particle velocity, and therefore it is critical to choose seed particles that will accurately follow the flow fluctuations (minimal particle lag time). Obtaining optimal flow seeding conditions unique to each technique is critical to the success of the measurements.

1.4.2.1 Laser Doppler Velocimetry (LDV)

Laser Doppler Velocimetry is a particulate based technique in which the Doppler frequency shift of elastically scattered light is used to provide velocity measurements, usually at a point or within a finite probe volume. The incident and scattered light wave directions define the direction of the measured velocity component. Early LDV systems utilized a heterodyne configuration in which a single laser source was used and light scattered from particles was mixed with the incident light at a detector. A spectrum analyzer was used to determine the beat frequency of the signal which is equal to the Doppler shift, and hence is proportional to the flow velocity (Yeh & Cummins, 1964). In this configuration, the signal is independent of flow direction and therefore has directional ambiguity. By crossing two laser beams of different frequencies the output signal becomes dependent on the sign of the velocity component and removes the directional ambiguity (Jernquist & Johansson, 1974). A review article by Tropea (1995) discusses the advancements and challenges of LDV in terms of miniaturization of systems, multi-point and multi-component systems, data and signal processing challenges, uncertainty estimation, and calibration procedures. Most systems now use fiber optics and diode lasers, reducing the size and making them easier to implement in test facilities. A problem which has received much attention is the difficulty in spectral

estimation due to the irregularity in temporal sampling since the velocity is sampled in time by random passages of tracer particles through the measurement volume.

Algorithms have been developed to provide equidistant re-sampling in time to allow for spectral estimation (Bell, 1982; Benedict et al., 2000). Measurement volumes are usually on the order of $0.1 \times 0.1 \times 1 \text{ mm}^3$. Temporal resolution is on the order of kHz.

Uncertainties of 0.1% can be expected in velocity when thousands of data values are averaged.

1.4.2.2 Planar Doppler Velocimetry (PDV) / Doppler Global Velocimetry (DGV)

Another particle-based Doppler velocimetry technique which provides velocity measurements in a planar region rather than at a single point is called Planar Doppler Velocimetry. Other research groups refer to this technique as Doppler Global Velocimetry. A review of planar velocity techniques, including PDV is given by Samimy and Wernet (2000). In PDV, elastically scattered light from particles entrained in the flow and illuminated by a stable-frequency narrow linewidth laser light sheet is imaged through an atomic or molecular vapor filter. The application of the vapor filters here is conceptually similar to their use in filtered Rayleigh scattering except in this case only the frequency shift of the scattered light must be resolved. The absorption features of the filter allow discrimination of the frequency shift of the scattered light, which is related to the amount of light transmitted through the filter. The Doppler shifted light is split into two paths; one path is imaged directly and in the other the light is imaged through the molecular filter. Many systems image both the reference and signal images side by side on a single CCD detector to reduce the number of cameras needed. With a single

observation direction only a single velocity component is measured. For three-component measurements three to six CCD cameras are required. This technique provides very high spatial resolution. It works best at very high velocities with typical accuracies of 1 – 2.5 m/s. McKenzie (1996) used analytical models of iodine vapor filters, noise sources associated with CCD detectors, and PDV signals to show that the dynamic range of a typical PDV system is approximately 200 m/s with accuracy of 1.5 m/s. A high speed PDV system using a pulse burst laser system and high speed cameras was used for 250 kHz rate velocity measurements in a Mach 2 jet (Thurrow et al., 2005). Weaknesses of this technique are the complexity of multi-component systems and the high cost of these systems, which are not commercially available.

1.4.2.3 Particle Image Velocimetry (PIV)

Particle Image Velocimetry is another particulate based measurement that provides two or three components of velocity. Unlike Doppler shift techniques such as LDV and PDV, PIV measures the physical particle displacements in order to provide velocity vectors in a planar region of a flow field. A laser provides two short-duration laser pulses at two closely spaced instances in time. The laser light is formed into a thin sheet which defines the measurement plane, and elastically scattered light from tracer particles is detected and recorded by a CCD camera at an orthogonal viewing direction. The images are analyzed by correlating respective subregions in each image to provide spatially-averaged particle displacements between exposures, and hence velocity of the particles within the subregion. Very high spatial resolution (< 1 mm) can be obtained with this measurement technique; spatial resolution is determined by the imaging optics, detector pixel size, and

subregion size used in the data processing. A single camera configuration provides two-component velocity measurements and using two cameras in a stereo imaging configuration provides three-component measurements. (Raffel et al., 1998) Three-component measurements have also been demonstrated with a hybrid technique using conventional PIV for the in-plane velocity components and a planar Doppler technique for the out-of-plane component (Wernet, 2004). PIV is applicable in a wide range of flow environments ranging from cold flows to hot combustion environments and from low velocity to supersonic flows. Most PIV systems to date have used Nd:YAG lasers with repetition rates on the order of 10-100 Hz. Recent advancements in laser and camera technology have enabled PIV measurements at rates as high as 25 kHz (Wernet, 2007). Uncertainties in PIV measurements are typically 1% of full scale, even in the high repetition rate systems. The main limitations of the technique involve seeding issues, such as difficulties in obtaining uniform seeding at sufficient concentration levels, and choosing particles that are small enough to follow the flow but large enough to be effective light scatterers (Melling, 1997).

1.4.3 Hybrid techniques

Many combined techniques exist to take advantage of the different measurement capabilities and provide multiple flow properties simultaneously. Rayleigh scattering and (P)LIF techniques are commonly employed simultaneously. Rayleigh thermometry is used to provide temperature measurements which may then be used to correct the LIF signal for temperature effects while the LIF signal provides species concentrations and mixture fraction (Dégardin et al., 2004; Chen & Mansour, 1997). In some work, Raman

scattering has been combined in addition to Rayleigh and LIF to provide additional species concentration information (Nooren et al., 2000). Fajardo et al. (2006) combined PIV and PLIF to measure simultaneous scalar and velocity fields at data rates up to 12 kHz. They used a single laser and wavelength separation to record the PIV and red-shifted fluorescence signals on separate cameras. Planar measurements of velocity, concentration, and strain rate were reported in a biacetyl and oil droplet seeded atmospheric air jet at a Reynolds number of 2000. This technique is limited to low speed flows (4 m/s in the reported work) because the laser is a single-head system which limits the temporal spacing between consecutive image pairs to the repetition rate of the laser. A combined CARS and interferometric Rayleigh scattering technique has been developed at NASA Langley Research Center in which CARS provides temperature and species concentration measurements while the Doppler shifted Rayleigh signal, which is detected at two different observation angles and heterodyned with reference light, provides two components of velocity (Tedder et al., 2007). Due to the very high temperatures present in the combustion environments where this system is used, the thermal broadening of the Rayleigh spectrum degrades the accuracy with which the frequency shifts can be measured. Chen et al. (1988) combined CARS and LDV to make temporally and spatially resolved simultaneous velocity and temperature measurements in a turbulent premixed conical flame. Lemoine et al. (1999) demonstrated simultaneous 2-D velocity and temperature measurements via a combined LDV and PLIF system in a turbulent heated water jet. Raman and LDV have been combined to provide simultaneous velocity, density, and temperature measurements in gaseous flows (Hillard et al., 1974). Optical techniques have also been combined with physical probe measurements, such as the work

by Pietri et al. (2000) where LDV and coldwire measurements were implemented simultaneously to provide temperature-velocity correlations as well as turbulent Prandtl number measurements, which are critical information for computational modeling of turbulent flows.

1.4.4 Summary

Tables 1.1 and 1.2 give summary lists of the molecular-based and particle-based measurement techniques, respectively. These tables provide an overview of the parameters that each technique is capable of measuring and the maximum demonstrated data rates. The temporal response of most of the optical measurement techniques is typically limited by the repetition rate of pulsed lasers; usually on the order of 10-100 Hz. One can potentially take many snap shots to obtain rms turbulence measurements, but the snapshots must be acquired at repetition rates greater than most standard pulsed lasers to provide power spectral content. Advances in laser and camera technology have led to recent developments of temporally resolved measurements with pulsed lasers at rates exceeding 10 kHz. Signal strength of the scattering process can also limit the temporal response. Rayleigh scattering has several advantages over other light scattering techniques; the Rayleigh scattering cross-section is three orders of magnitude greater than the Raman scattering cross-section, and Rayleigh scattering is generally much simpler and lower cost to implement than techniques that require multiple lasers and have other complicating factors.

Using a cw laser has many advantages over a pulsed-laser for obtaining quasi-instantaneous time-resolved Rayleigh scattering measurements. CW lasers have stable output power eliminating the need to sample the input beam to account for shot-to-shot pulse energy variations as with pulsed lasers. Pulsed lasers operating at the repetition rate needed to provide sufficient time resolution to fully recover the turbulence frequencies in high speed jets (> 25 kHz) are pushing the limit of existing laser technologies. Although high repetition rate lasers exist, they do not have the narrow linewidth, stable frequency, and high beam quality typically needed in spectroscopic Rayleigh scattering flow diagnostics. Collecting Rayleigh scattered light over a finite length of a high power cw laser beam, spectrally filtering the light, and sampling the number of photons collected during very short integration periods provides point-wise multi-property measurements with spatial resolution of approximately $0.1 \times 0.1 \times 1 \text{ mm}^3$ at high temporal resolution without the need for multiple lasers and complex alignment requirements.

Table 1.1. Summary of molecular-based optical measurement techniques.

Technique	Measured Properties	Max rate
Raman scattering	<i>temperature, density</i> (species specific)	< 100 Hz
CARS	<i>temperature, density</i> (species specific)	< 100 Hz
LIF	<i>temperature, velocity, density, pressure</i> (species specific)	2 kHz
Laser-induced gratings	<i>temperature, velocity, density</i>	< 100 Hz
Molecular tagging	<i>temperature, velocity</i>	< 100 Hz
Collective light scattering	<i>temperature, velocity, density fluctuations</i>	< 100 Hz
Rayleigh scattering	<i>temperature, velocity, density, (pressure)</i>	> 30 kHz
Diode laser absorption	<i>temperature, velocity, density, pressure</i> (species specific); path-integrated measurement	\sim kHz

Table 1.2. Summary of particle-based optical measurement techniques.

Technique	Measured Properties	Max rate
Laser Doppler Velocimetry	<i>velocity</i> , single or multi-component; point measurement	~ kHz
Planar Doppler Velocimetry / Doppler Global Velocimetry	<i>velocity</i> , single or multi-component; planar measurement	250 kHz
Particle Image Velocimetry	<i>velocity</i> , 2- or 3-component; planar measurement	> 25 kHz

1.5 Organization of dissertation

Chapter 2 reviews Rayleigh scattering theory and Fabry-Perot interferometer, and discusses how the concepts are applied in this work.

Chapter 3 discusses the uncertainty analysis and the numerical simulation developed to model and analyze optical system configurations.

Chapter 4 describes the two experiments used to validate the measurement technique and the third experiment that demonstrates the use of this technique in an electrically-heated jet facility.

In Chapter 5, the results from validation and application experiments are discussed. An acoustically modulated nozzle flow was used to validate the velocity fluctuation and frequency measurements, and an asymmetric oscillating counterflow with unequal enthalpies was used to verify the temperature and density fluctuation and frequency measurements by comparison with hotwire and coldwire probe measurements. Sinusoidal fluctuations of the properties of interest were induced in these flows at various

frequencies and amplitudes to verify that the Rayleigh scattering system was able to accurately recover the fluctuations. Measurements in a high speed electrically-heated air flow were made in a lab-scale version of a larger aero-acoustic facility at the NASA Glenn Research Center.

Chapter 6 summarizes the results and conclusions from this work and provides recommendations for future improvements and implementations in various flow characterization ground test facilities.

1.6 Publications

The following publications have resulted from this work.

Mielke, A. F., and Elam, K. A. (2005) Molecular Rayleigh scattering diagnostic for measurement of high frequency temperature fluctuations. Proceedings from *SPIE Optical Diagnostics Conference*, 5880, Bellingham, WA.

Mielke, A. F., Elam, K. A., & Sung, C. J. (2006) Rayleigh Scattering Diagnostic for Measurement of Temperature, Velocity, and Density Fluctuation Spectra. *44th AIAA Aerospace Science Meeting*, paper # AIAA-2006-0837, Reno, NV.
*Winner of 2006 AIAA Northern Ohio Section Best Young Professional Paper Award

Mielke, A. F., Elam, K. A., & Sung, C. J. (2006) Molecular Rayleigh Scattering Diagnostic for Dynamic Temperature, Velocity, and Density Measurements. *25th AIAA Aerodynamic Measurement Technology and Ground Testing Conference*, paper # AIAA-2006-2969, San Francisco, CA.

Mielke, A. F., Elam, K. A., & Sung, C. J. (2007) Development of a Rayleigh scattering diagnostic for time-resolved gas phase flow velocity, temperature, and density measurements in aerodynamic test facilities. Proceedings from *the 22nd International Congress on Instrumentation in Aerospace Simulation Facilities*, Pacific Grove, CA.

CHAPTER 2

RAYLEIGH SCATTERING THEORY AND SPECTRAL ANALYSIS USING FABRY-PEROT INTERFEROMETRY

2.1 Introduction

Molecular Rayleigh scattering is the result of elastic light scattering from gas molecules. This chapter presents the theory describing this light scattering phenomenon and explains the operation of a Fabry-Perot interferometer and how it is used in the current experiment to resolve the Rayleigh scattering spectrum, allowing gas flow velocity, temperature, and density to be evaluated.

2.2 Rayleigh scattering theory

In molecular Rayleigh scattering an incident electric field interacts with an atom or molecule inducing a dipole moment that oscillates and radiates at the frequency of the incident field. It is considered an elastic scattering process because the internal energy of the molecule is unchanged and the frequency of the light is changed only by the Doppler effect due to the molecular motion. When light from a single frequency laser beam passes through a gas, the scattered light is shifted in frequency by the Doppler effect due to the thermal as well as the bulk motion of the molecules. The frequency spectrum of the scattered light contains information about the gas density, bulk velocity, and temperature. Figure 2.1 shows a Rayleigh scattering spectrum containing the narrow laser line and a typical Rayleigh spectral peak to illustrate how the flow property measurements are obtained from the spectral information. If the gas composition is fixed, the total intensity of the Rayleigh scattered light is directly proportional to the gas density. The frequency

shift between the laser peak and the Rayleigh peak is proportional to the bulk flow velocity. The width of the spectrum is related to the gas temperature.

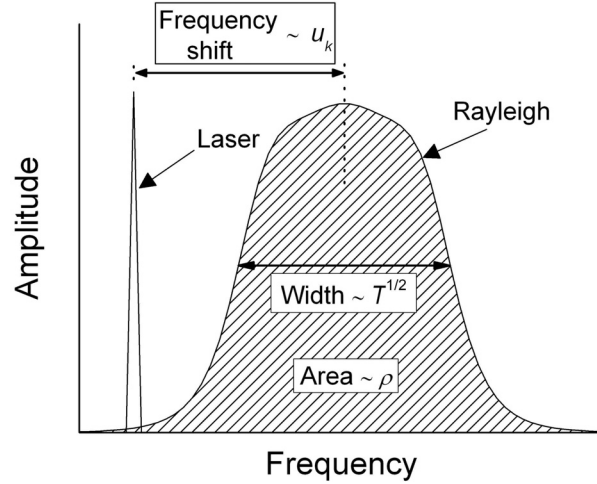


Figure 2.1. Rayleigh scattering spectrum.

The shape of the spectrum is dependent on gas pressure p and temperature T , and the scattering angle χ_s (Tenti et al., 1974). A non-dimensional parameter y , which represents the ratio of the wavelength of the scattering grating $\left(A = \frac{\lambda}{2 \sin \frac{\chi_s}{2}} \right)$ to the mean free path between molecular collisions $\left(l_m = \frac{a\eta}{n\kappa T} \right)$, is used to establish spectral shape regimes:

$$y = \frac{A}{2\pi l_m} = \frac{p}{\eta\kappa a} \quad (2-1)$$

where a is the most probable molecular speed:

$$a = \sqrt{\frac{2\kappa T}{m}} \quad (2-2)$$

λ is the illumination wavelength, η is the dynamic viscosity of the gas, n is the molecular number density ($n = \frac{\rho}{m}$, where ρ is the gas density and m is the molecular mass), and κ is Boltzmann's constant. The interaction wave vector \vec{K} , which defines the direction of the velocity component being measured, is the bisector of the incident and scattered light wave vectors, \vec{k}_0 and \vec{k}_s , respectively (figure 2.2). The interaction wave vector and its magnitude K are given by:

$$\vec{K} = \vec{k}_s - \vec{k}_0 \quad (2-3)$$

$$K = |\vec{K}| = \frac{4\pi}{\lambda} \left[\sin \frac{\chi_s}{2} \right] \quad (2-4)$$

The geometry of the optical arrangement in an experiment can be designed such that the desired component of the velocity u_k is measured:

$$u_k = \frac{\vec{K} \cdot \vec{v}}{K} \quad (2-5)$$

Experiments are typically arranged such that the electric field vector \vec{E} is perpendicular to the scattering plane defined by the incident and scattered light wave vectors ($\beta = 90^\circ$, 's'-type polarization (figure 2.2)). In this situation scattering is independent of the scattering angle. In the opposite situation where $\beta = 0^\circ$ and \vec{E} is in the scattering plane ('p'-type polarization) the scattering is dependent on scattering angle and approaches zero as χ_s approaches 90° .

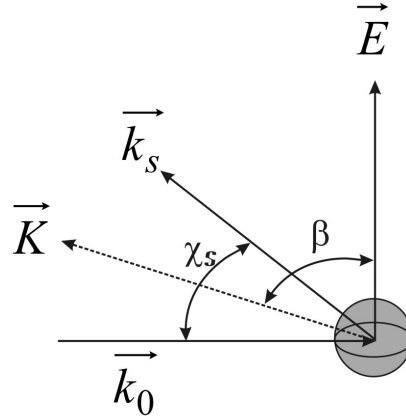


Figure 2.2. Light scattering from a moving particle.

Three spectral shape regimes are defined for typical $\chi_s = 90^\circ$ scattering (Yip & Nelkin, 1964; Tenti et al., 1974; Sandoval & Armstrong, 1976). The shape regimes are illustrated in figure 2.3, where the normalized frequency is defined as:

$$x_f = \frac{2\pi(f - f_0)}{Ka} \quad (2-6)$$

where f_0 is the frequency of the incident laser light. For low density gases where $y \ll 1$ the probability of molecular interactions is small and the molecular motion is thermally dominated. In this case the Rayleigh spectrum is determined only by the molecular velocity distribution which is accurately modeled by a Gaussian function for a Maxwellian velocity distribution. The gas is said to be in the Knudsen or collisionless regime. For higher density gases where $y \gg 1$ and molecular motions become correlated, collective effects become significant. The Rayleigh spectrum broadens and eventually develops sidebands and the lines shapes become Lorentzian. These sidebands are caused by thermally excited acoustic waves that cause density fluctuations to move at the speed of sound and are referred to as Brillouin-Mandel'shtam scattering (Landau & Placzek,

1934). This case is referred to as the hydrodynamic or continuum regime where molecular collisions are the dominant process and analysis involving the Fluctuation-Dissipation Theorem becomes necessary (Callen et al., 1952; Clark, 1975). Finally, for $0.2 \leq y \leq 2$, as is the case in the present experiments, the gas is in a transition region between the collisionless and hydrodynamic regimes, and a kinetic theory model is required. The line shape in this case is governed by both acoustic and thermal processes.

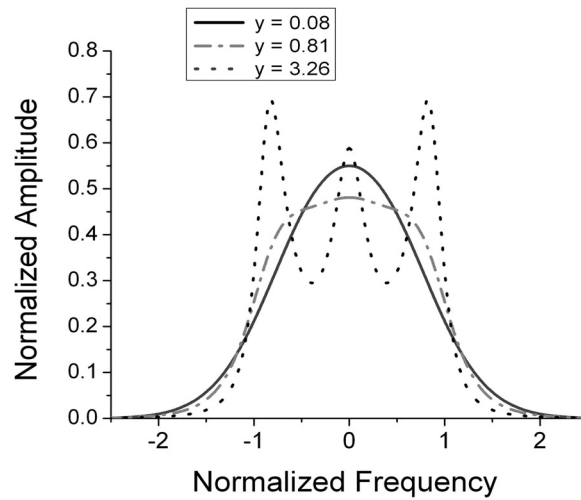


Figure 2.3. Rayleigh scattering spectrum for various y -parameters.

A kinetic theory model developed by Professor G. Tenti (TENTI S6: 6-moment Rayleigh scattering model) provides the Rayleigh-Brillouin spectrum for diatomic gases in all density regimes (Boley et al., 1972; Tenti et al., 1974). This is the most accurate model currently available, although it is not exact since it assumes a single species and does not account for additional scattering processes, such as Raman scattering, which may fall in close proximity to the elastic scattering regime. Appendix A discusses the contribution of rotational Raman scattering to the Rayleigh signal and demonstrates that, for our purposes, neglecting the Raman signal in the spectral model is acceptable. The TENTI S6 model requires values for shear viscosity, thermal conductivity, molecular weight,

internal specific heat, and bulk viscosity of the gas in addition to the y -parameter in order to generate the spectral information. The shear viscosity, thermal conductivity, and mean molecular weight for air, and nitrogen values of internal specific heat and bulk viscosity (as air values were not available) were used for generation of the Rayleigh spectrum using the TENTI S6 model calculated using a computer code provided by Professor G. Tenti. This spectrum model was used to generate the information displayed in figures 2.1 and 2.3, and is incorporated in the model function used in maximum likelihood estimation (MLE) analysis of the experimental data.

2.3 The Fabry-Perot Interferometer (FPI)

The spectrum of the Rayleigh scattered light is analyzed using a planar mirror FPI (figure 2.4) (Vaughan, 1989). The Fabry Perot etalon consists of two parallel planar mirrors with their reflective surfaces facing each other. Maximum transmission occurs when the optical path-length difference (OPD) between each transmitted beam is equal to an integer multiple of the wavelength, or

$$OPD = 2\mu d \cos \theta = m_i \lambda , \quad (2-7)$$

where m_i are integer values representing the order of interference; the maximum reflectivity, or minimum transmission occurs when the OPD is equal to half of an odd multiple of the wavelength. By varying either the mirror spacing d or the index of refraction μ of the medium in the cavity between the mirrors transmission of different frequencies will occur and recreate the Rayleigh spectrum. In this scenario light from a point source is collimated into the etalon and either the mirror spacing is scanned by a piezoelectric element or the index of refraction is varied by changing the pressure in the

etalon cavity. This mode of operation is considered the “scanning mode” and can only be used for time-averaged measurements. In the static “imaging mode” the plate spacing and medium refractive index are held constant while the angle of the incoming light ray θ is varied by imaging points off-axis. A lens at the etalon output images the light source at the image plane where a detector is located. A planar source emitting monochromatic light provides an image of the source modulated in intensity by concentric light rings at locations associated with angles that meet the criterion of Eq. (2-7) as shown in figure 2.5.

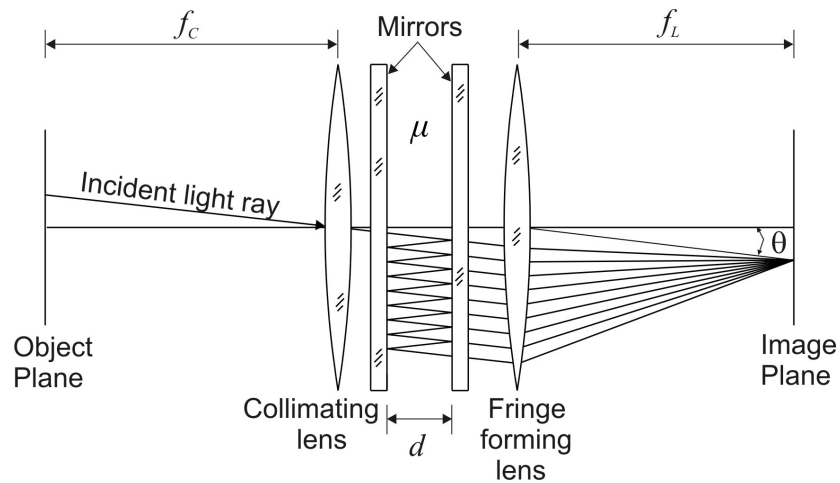


Figure 2.4. Fabry-Perot interferometer.

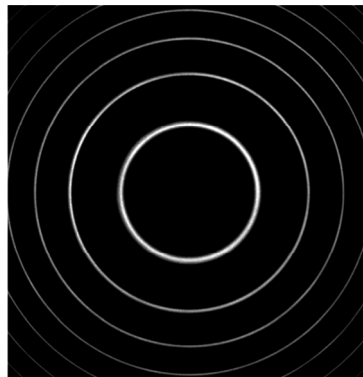


Figure 2.5. Concentric ring interference pattern from a planar single frequency light source imaged through a Fabry-Perot interferometer operated in the static imaging mode.

The fringes have unequal spacing that is directly related to the free spectral range (*FSR*) of the instrument, which is the change in frequency needed to shift the fringe system by one fringe and can be evaluated by the following relation:

$$FSR = \frac{c}{2d\mu} \quad (2-8)$$

where c is the speed of light. The transmission bandwidth of the etalon is a function of the mirror reflectivity R and is described by the *reflective* finesse (N_r) of the instrument:

$$N_r = \frac{\pi\sqrt{R}}{1-R} \quad (2-9)$$

The *effective* finesse, N_e , includes additional contributions from beam divergence, finite clear aperture of the etalon, and defects such as surface irregularities, curvature of the mirror surfaces, and plate parallelism. Etalons with high finesse have sharper transmission peaks and lower transmission minima than an etalon with low finesse. The ratio of the *FSR* to the finesse provides the full-width at half-maximum (*FWHM*) of the instrument function. Due to the fact that high finesse requires very high mirror reflectivity, the amount of light that is transmitted through the etalon is greatly reduced, which can be restrictive in situations of very low signal levels. If the incoming light has a very narrow linewidth the imaged intensity pattern will essentially be a delta function convolved with the Airy function. For spectrally broadened light, such as Rayleigh scattered light, the rings will broaden accordingly. The linewidth of the rings provides a measure of temperature from Rayleigh scattered light. The frequency shift of the light associated with the bulk flow velocity can be determined by a spatial shift in the ring positions in the image. The imaging mode allows instantaneous and time-resolved

measurements to be obtained, provided that enough light is available and a high sensitivity detector with fast response time is available.

2.4 Model development for the recorded interference pattern

In this work the FPI is operated in the static imaging mode. The fringe intensity pattern is a function of both the Rayleigh spectrum and the Fabry-Perot instrument function. The Fabry-Perot instrument function as a function of normalized frequency x_f and radial position in the image plane r is given by the following relation:

$$I_{FP}(x_f, r) = \frac{1}{1 + F \sin^2 \frac{\psi(x_f, r)}{2}} \quad (2-10)$$

where F is the instrument function contrast defined as:

$$F = \frac{1}{\sin^2 \left(\frac{\pi}{2N_e} \right)} \quad (2-11)$$

and ψ is the phase change between successive reflections:

$$\psi = \frac{4\pi\mu d}{\lambda} \left[\frac{\theta_R^2 - \theta^2}{2} + \frac{\lambda a}{cA} x_f \right] \quad (2-12)$$

$$\text{where } \theta = r/f_L \quad (2-13)$$

f_L is the fringe forming lens focal length, and θ_r is the angle between the optical axis and the light ray associated with the incident laser frequency.

Rayleigh scattered light from a defined probe volume is collected into a multimode optical fiber. The power P_s scattered into solid angle Ω from a volume of size L_x^3 illuminated by a plane wave of intensity I_0 is:

$$P_s = I_0 n L_x^3 \Omega \left(\frac{d\sigma}{d\Omega} \right) \sin^2 \beta \quad (2-14)$$

where $\frac{d\sigma}{d\Omega}$ is the differential scattering cross-section. In this experiment the incident laser beam with power P_0 is focused to a diameter smaller than the imaged field size. In this case, the power collected is proportional to the length of the probe volume L_x set by the field size of the collection optics.

$$P_s = P_0 n L_x \Omega \left(\frac{d\sigma}{d\Omega} \right) \sin^2 \beta \quad (2-15)$$

It is often convenient to express the total collected Rayleigh scattered power in terms of expected photoelectron counts $\langle N_R \rangle$:

$$\langle N_R \rangle = \frac{\varepsilon P_0 n L_x \lambda \Omega \Delta t}{h c} \left(\frac{d\sigma}{d\Omega} \right) \sin^2 \beta \quad (2-16)$$

where the overall system efficiency ε includes detector quantum efficiency and other losses, Δt is the integration time over which photoelectrons are counted, and h is Planck's constant. The solid angle Ω is fixed by the $f/\#$ of the collection optics:

$$\Omega = \frac{\pi}{4(f/\#)^2} \quad (2-17)$$

The differential scattering cross-section is defined as (Eckbreth, 1996):

$$\frac{d\sigma}{d\Omega} = \frac{4\pi}{\lambda^4 n^2} (\mu - 1)^2 \quad (2-18)$$

The scattering cross-section is negligibly dependent on temperature and pressure but has a strong dependence on wavelength which leads to the use of shorter wavelengths in most Rayleigh scattering experiments. The scattering cross-section at the laser wavelength of 532 nm is obtained using published refractive index data for air as $5.9 \times 10^{-32} \text{ m}^2/\text{sr}$.

The light exiting the fiber is collimated and directed to the FPI, and a lens at the interferometer output focuses the interference fringe pattern at the image plane. With the interferometer in the light path, the interference fringe pattern is equivalent to the intensity of the image of the fiber face without the Fabry-Perot modified by the transmission properties of the FPI. The expected amount of energy collected from the q^{th} annular region of the interference pattern, which has been dissected into one circular and three annular regions, in terms of photoelectron counts, can be expressed by the following model function:

$$\langle N_q \rangle = \frac{\langle N_R \rangle}{\pi r_{\max}^2} 2\pi \int_{r_{i,q}}^{r_{o,q}} \int_{-\infty}^{\infty} S_R(x_f) I_{FP}(x_f, r) r dx_f dr \quad (2-19)$$

where r_{\max} is the radius of image of the fiber face, $r_{i,q}$ and $r_{o,q}$ are the inner and outer radii of the q^{th} annular region, respectively, and the Rayleigh spectrum S_R is evaluated using the TENTI S6 model. The developed model function given by Eq. (2-19) is used to evaluate the lower bound measurement uncertainty, which will be presented in Chapter 3, and is incorporated in the numerical model developed to generate simulated “noisy” data

(Appendix D), and is used as the model function in the MLE analysis of the experimental data (Appendix E).

The Fabry-Perot used in the experiments discussed in this dissertation has a *FSR* of 8.7 GHz and effective finesse of approximately 15, which provides an instrument function with *FWHM* of 0.58 GHz. The width of the Rayleigh spectrum is set by the molecular thermal motion. For a temperature of 300 K the Rayleigh spectral linewidth is approximately 1.1 GHz; hence the resolution of the interferometer is sufficient to resolve the Rayleigh spectrum. The imaged fringe pattern is limited by the finite diameter of the optical fiber face that is imaged through the Fabry-Perot. The image diameter in the current experiments is equivalent to a partial fringe order and therefore, only the innermost fringe of the pattern is detectable. The outer diameter of the image is equivalent to approximately 0.4 times the *FSR* of the instrument, which is equivalent to a maximum frequency shift of approximately 3.5 GHz. This means that the maximum velocity that can be measured must result in a frequency shift of less than this amount. The velocity associated with a 3.5 GHz frequency shift for the current experimental arrangement is 1300 m/s. This would require a reference fringe that is right at the edge of the image and a Doppler shifted fringe at the origin of the concentric pattern. In reality, this would be an impossible situation to measure. A more realistic velocity measurement limit would be approximately half of this or 650 m/s.

CHAPTER 3

UNCERTAINTY ANALYSIS AND NUMERICAL SIMULATION

3.1. Introduction

In photon counting experiments, the dominant noise source typically is statistical shot noise. A Cramer-Rao lower bound uncertainty analysis is presented in this chapter, including the determination of experiment parameters by uncertainty minimization and a summary of the lower bound uncertainties in the estimates of instantaneous density, temperature, and velocity for the range of values expected in the experiments. The results of numerical simulations of “noisy” data based on the model function determined in Chapter 2 and the generation of statistical shot noise are presented that evaluate the uncertainty levels expected in 2nd order statistical calculations such as power spectra and fluctuation levels.

3.2 Lower bound for measurement uncertainty

The lower bound on the uncertainty in temperature, velocity, and density measurements using Rayleigh scattering is set by the photon statistical (shot) noise. Shot noise can be modeled by a Poisson distribution as discussed in Appendix B. Estimates of the measurement uncertainty in the unknown parameters for the Rayleigh measurement technique were obtained by Cramer-Rao lower bound analysis (Whalen, 1971). For a measurement that is a function of a set of unknown parameters $\beta_i = [\beta_1, \beta_2, \beta_3, \dots]$ the variance σ_i^2 of the estimates $\hat{\beta}_i$ of the parameters is:

$$\sigma_i^2 \geq [\Gamma^{-1}]_{ii} \quad (3-1)$$

where the Fisher information matrix for Poisson statistics is given by:

$$\Gamma_{i,j} = \sum_k \frac{1}{\langle N_k \rangle} \frac{\partial \langle N_k \rangle}{\partial \beta_i} \frac{\partial \langle N_k \rangle}{\partial \beta_j} \quad (3-2)$$

If a Gaussian spectrum is assumed, the lower bounds for uncertainty or standard deviation in the instantaneous temperature T , velocity u_k , and density ρ measurements for an ideal instrument are:

$$\begin{aligned} \sigma_T &= \left(\frac{2T^2}{\langle N_R \rangle} \right)^{1/2} \\ \sigma_{u_k} &= \left(\frac{a^2}{2\langle N_R \rangle} \right)^{1/2} \\ \sigma_\rho &= \left(\frac{\rho^2}{\langle N_R \rangle} \right)^{1/2} \end{aligned} \quad (3-3)$$

Appendix C provides the detailed derivation of Eq. (3-3) as well as a sample calculation for the lower bound uncertainty in temperature, velocity, and density estimates for air at a temperature of 298 K and standard atmospheric pressure for an ideal loss-free instrument that samples the data at a rate of 32 kHz. This analysis resulted in the following lower bounds on the uncertainties in these parameter estimates:

$$\sigma_T \geq 1.65 \text{ K} \quad \sigma_{u_k} \geq 1.14 \text{ m/s} \quad \sigma_\rho \geq 0.0046 \text{ kg/m}^3$$

For any *real* instrument, these measurement uncertainties will be higher. Using the model function (Eq. 2-19) developed for $\langle N_q \rangle$, the lower bound measurement uncertainty in each parameter estimate was determined by calculation and inversion of the Fisher

information matrix. The model function takes into account the FPI, quantum efficiency of the PMTs, and additional signal loss throughout the optical system due to coupling losses into the optical fiber and other transmission losses. The TENTI S6 spectral model was used to calculate the Rayleigh scattering spectrum in this analysis rather than using the simpler, less accurate Gaussian model used in the analysis above (Boley et al., 1972; Tenti et al., 1974). The uncertainty analysis was performed for a sampling rate of 32 kHz, a probe volume length of 1.1 mm and $f/4$ collection optics.

3.2.1 Experiment optimization

The Cramer-Rao lower bound analysis was used to optimize the experiment parameters, such as reference fringe radius (r_R) and the radii of the fringe dissection mirrors. The parameters were varied in the model until the uncertainty levels in both T and u_k were minimized. A sample optimization analysis is presented here using a temperature of 298 K and velocity of 0 m/s. First, using an arbitrarily chosen r_R value, the dissection mirror radii were varied over a range of reasonable values until minimum uncertainty in the temperature and velocity estimates were achieved. Figure 3.1 illustrates the selection of the outer radius of the third concentric mirror from the center of the mirror system as $r_{o,3} = 8$ mm based on prior selections of first and second mirror radii of 2.5 mm and 6 mm, respectively. These values for the mirror radii provided maximum sensitivity of the amount of light in each region to small changes in velocity and temperature. Figure 3.2 illustrates the locations of the mirror radii ($r_{o,1}$, $r_{o,2}$, and $r_{o,3}$) and the radius of the outer edge of the image of the fiber face (r_{max}) with respect to the Rayleigh fringe and the regions detected by each PMT. The 2nd and 3rd mirrors divide the central portion of the

fringe at its peak, maximizing sensitivity to changes in peak location and velocity. The 1st and 2nd mirrors and 3rd and 4th mirrors are positioned to divide the fringe along the sloped sides such that sensitivity to changes in fringe width and temperature is maximized. After the mirror radii values were chosen, r_R was varied over a reasonable range and a value of $r_R = 6.5$ mm was chosen based on the point where uncertainty levels were minimized, as illustrated in figure 3.3. A minimum in uncertainty exists because the value chosen for r_R sets the location of the Doppler shifted Rayleigh fringe, which must be optimized so that as little information as possible is lost into the center of the image or outside of the imaged diameter. The optimum r_R value may change depending on the flow velocity, as illustrated in figure 3.4. In these experiments r_R was maintained at 6.5 mm regardless of flow velocity. Therefore the uncertainty in the measurements may be slightly greater than it would be if r_R were adjusted for each velocity setting. For example, figure 3.5 shows that the velocity uncertainty for $u_k = -120$ m/s, which is nearly the maximum velocity studied in this dissertation, increases from 26.5 m/s at its optimum r_R of 7.5 mm to 32 m/s at r_R of 6.5 mm.

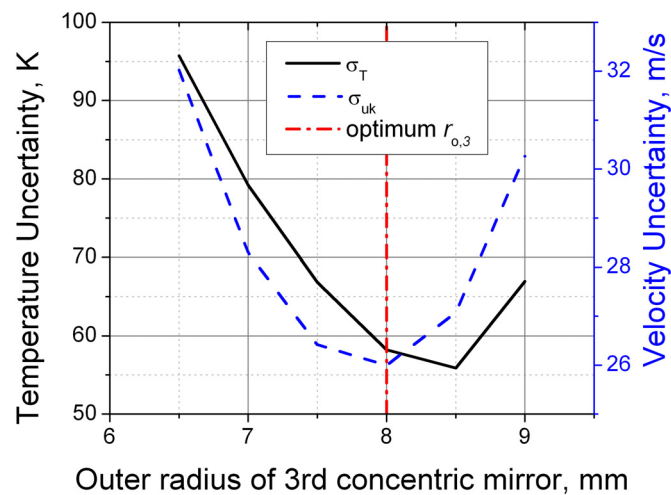


Figure 3.1. Optimization of the outer radius of the third concentric mirror from the center of the mirror system.

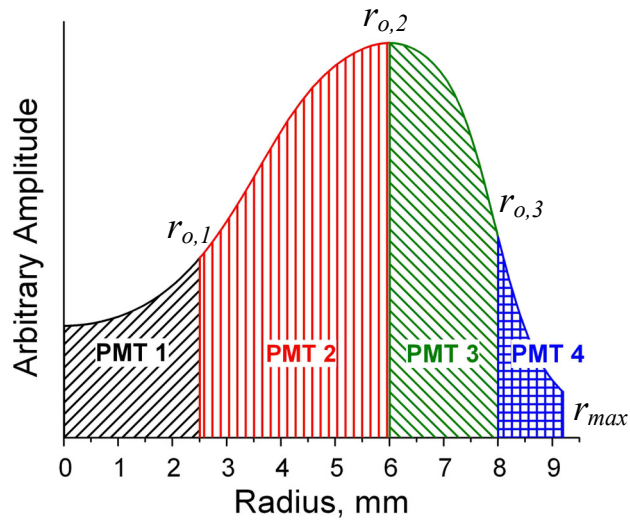


Figure 3.2. Radial slice of a fringe pattern showing the annular regions detected by the four PMTs where $r_{o,1}$, $r_{o,2}$, and $r_{o,3}$ are the outer radii of the first three mirrors and r_{max} is the radius of the image of the fiber face.

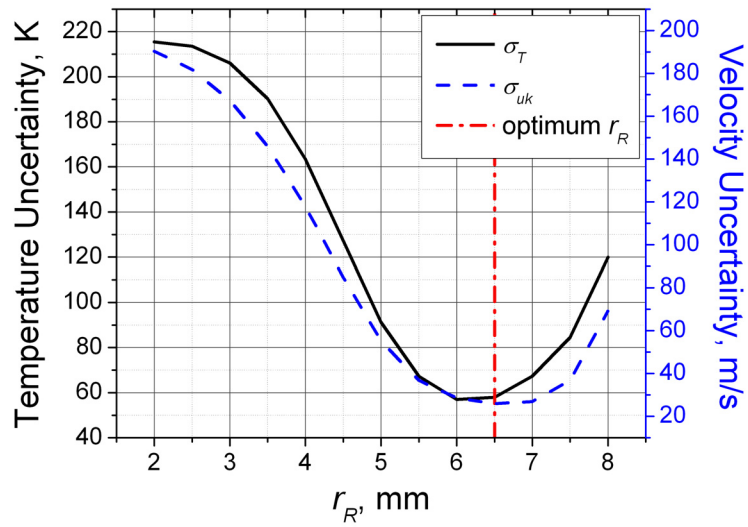


Figure 3.3. Optimization of reference fringe radius.

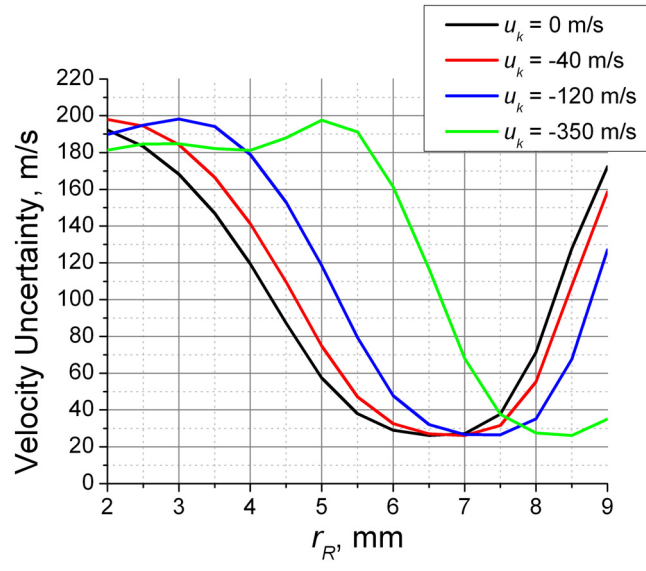


Figure 3.4. Optimization of reference fringe radius for various flow velocities.

3.2.2 Experiment measurement uncertainty

The optimum experiment parameters determined in the preceding section were used in the analysis of the measurement uncertainty over the expected range of flow conditions at a data acquisition rate of 32 kHz. Figure 3.5 shows the relative uncertainty in the instantaneous density estimates over the range expected in these experiments. The uncertainty in the density estimate is inversely related to the square-root of the number of photons detected by the PMT used for the density measurement, including the efficiency of the detector and loss through the fiber, as shown by Eq. (3-3). Therefore, as the number of detected photons increases the relative uncertainty decreases as shown in figure 3.5.

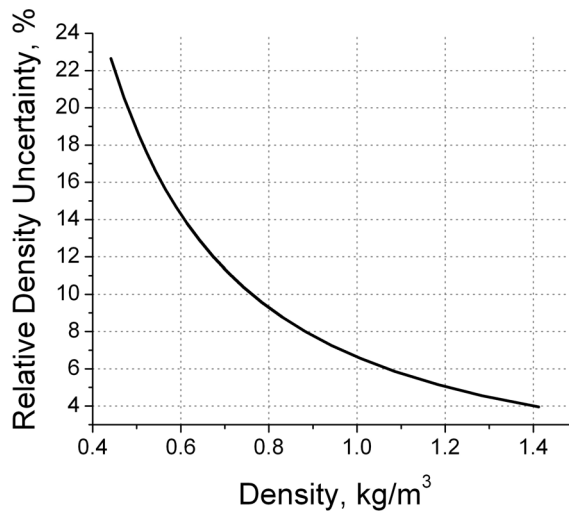


Figure 3.5. Relative uncertainty for instantaneous density estimates for 32 kHz sampling rate.

Figure 3.6 shows the absolute uncertainty in the instantaneous temperature estimates for a static temperature range from 298 K to 773 K and a range of velocities from -400 m/s to 200 m/s, and figure 3.7 shows the absolute uncertainty in instantaneous velocity estimates for the same range of temperatures and velocities. The optical system has been optimized for the velocity range from -120 m/s to 0 m/s expected in these experiments; hence, the region of the curves exhibiting minimum uncertainty occurs in this velocity range. The uncertainty increases outside of this velocity range since the shifted fringe is located either too close to the center of the image or too close to the outer edge of the image such that information is lost outside of the imaged region and the uncertainty in the parameter estimates is significantly increased. Measurement uncertainty for T and u_k increases as temperature increases as shown in figures 3.6 and 3.7. The uncertainty in both temperature and velocity is inversely related to the square-root of the number of photoelectron counts as indicated by Eq. (3-3). The number of photon counts decreases as

temperature increases; this is attributable to the lower gas density at higher temperatures, resulting in fewer scattering molecules, and hence fewer scattered photons. Although the uncertainty in the parameters is rather high for instantaneous measurements, long data records allow for calculation of higher accuracy statistical quantities such as power spectra and mean square fluctuations. Also, implementing certain optical system modifications can improve the number of photon counts and reduce the instantaneous measurement uncertainty. Obviously increasing the incident laser power is one way to improve the signal strength; however the maximum output power for single-frequency cw lasers is limited to about 18 Watts at a wavelength of 532 nm in current state-of-the-art laser technology. There are alternative ways to improve the detected signal strength, but each comes with a downside as discussed below.

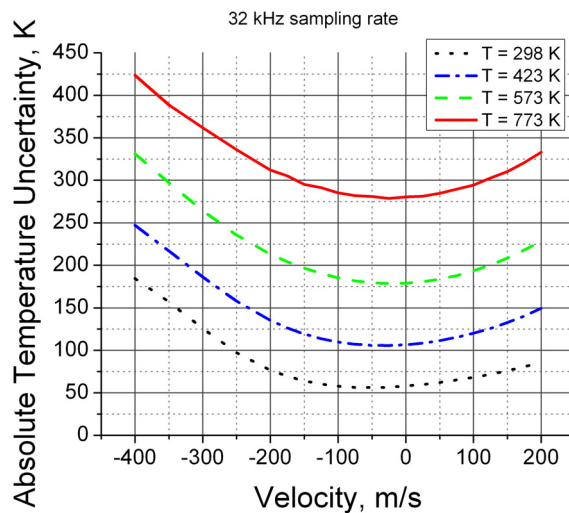


Figure 3.6. Absolute uncertainty for instantaneous temperature estimates for 32 kHz sampling rate.

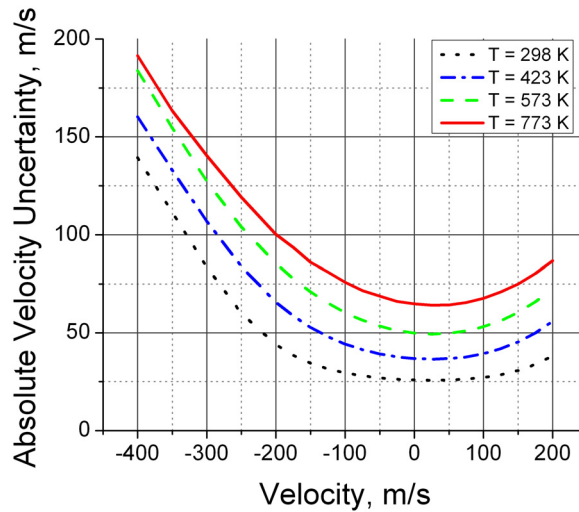


Figure 3.7. Absolute uncertainty for instantaneous velocity estimates for 32 kHz sampling rate.

Decreasing the sampling rate increases the photon counting integration time for each quasi-instantaneous data sample. Experimental data was acquired at a lower sampling rate of 16 kHz in addition to the 32 kHz rate used in the above uncertainty analysis. The photon count values double for a sampling rate of 16 kHz since the integration time over which photons are collected for each individual sample is lengthened by a factor of 2; therefore the uncertainty levels in the instantaneous measurements are a factor of $\sqrt{2}$ better than those at the higher sampling rate of 32 kHz. In order to capture the contributions of fluctuations over the greatest range of frequencies it is ideal to sample at the highest rate possible. Also, as sampling rate increases, the integration time of each sample shortens, approaching a more *instantaneous* type of measurement. One way to counteract the increase in uncertainty due to increasing the sampling rate is to increase the number of scattered photons in some other way, such as increasing laser power, increasing the probe volume size, or increasing the collection cone angle by reducing the

lens $f/\#$. If the signal strength is doubled by using twice the laser power or twice the probe volume length the uncertainty levels will decrease by a factor of $\sqrt{2}$. Decreasing the $f/\#$ by a factor of 2 increases Ω and the signal strength by a factor of 4; hence the uncertainty levels are improved by a factor of 2. In the current experiment, the probe volume length was 1.1 mm, which was approximately 1/10 of the jet diameter. In larger facilities an increase in probe volume size may be a viable solution for reducing uncertainty levels as long as the ratio of probe volume length to the facility length scale is kept reasonably small, and large temperature or velocity gradients are not experienced across the probe volume length. As the collection cone angle increases, so does the range of scattered light wave vectors collected across the lens aperture. For $f/4$ collection optics, the collection angle range is $\pm 7^\circ$ about the mean scattering angle, which means that the velocity measurement is actually an average of the velocity components measured by this range of scattering angles. The center of the spectral peak is still centered at the location of the desired velocity component and therefore does not affect the accuracy of the velocity measurement. However, the broadening of the spectrum due to this effect (often referred to as aperture broadening) will induce a bias in the temperature measurements. The affect of this broadening was modeled and presented by Mielke et al. (2005). For the y -parameters used in these experiments ($y \leq 1$), the change in the width and shape of the spectrum is negligible compared to the overall width and shape of the spectrum due to thermal broadening as shown in figure 3.8; therefore aperture broadening is neglected in the data analysis. However, the effect may not be negligible under other circumstances, such as in experiments with large y -parameter values, as shown in figure 3.9.

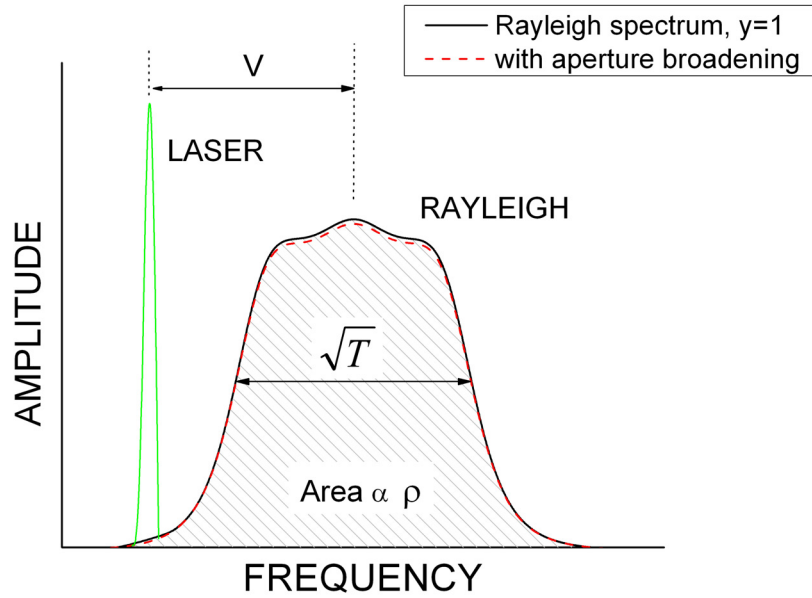


Figure 3.8. Effect of aperture and turbulence broadening on the Rayleigh scattering spectrum for $y = 1.0$, $f/3.7$ collection optics and 16% turbulence intensity. (Mielke et al., 2005)

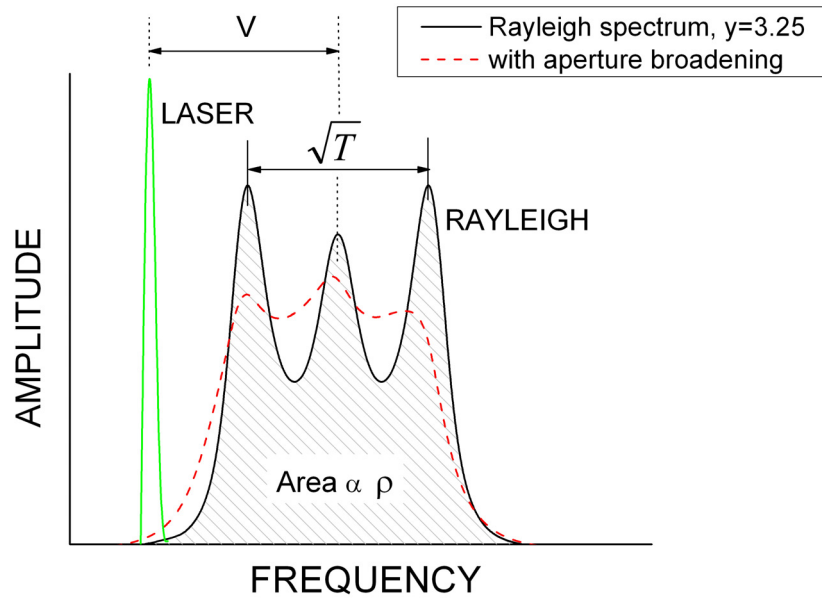


Figure 3.9. Effect of aperture and turbulence broadening on the Rayleigh scattering spectrum for $y = 3.25$, $f/3.7$ collection optics and 16% turbulence intensity. (Mielke et al., 2005)

3.3 Simulation of *noisy* data

The model function given by Eq. (2-19) was used to generate photon count data based on input velocity and temperature values. A time record of temperature and velocity values similar to the values expected in the experiments was provided as input for the simulation. Pressure was assumed to be atmospheric and the ideal gas law was used to calculate the density values. For each sample in the time record ideal (noise-free) data were computed in terms of expected photon counts from each of the five PMTs. Photon count values were generated with Poisson noise for each sample and recorded in a data file. The simulated data record was then read into another program that performed MLE using the photon counts in the record to determine instantaneous velocity and temperature values, identical to the data analysis performed on *experimental* data. The purpose of the simulation exercise is three-fold:

1. To understand noise contributions in the experiment
2. To evaluate baseline noise levels in the current experiment
3. To provide a design/optimization tool for future experiments in other test facilities

Further details on the algorithm and procedure of the simulation analysis can be found in Appendix D. A description of the MLE data analysis procedure can be found in Appendix E.

Simulated data were generated for a range of steady temperatures and velocities at a data rate of 32 kHz. The entire time records are 1.28 seconds long but only the first 0.1 seconds are shown for a sample case with mean density, temperature, and velocity of 0.83 kg/m^3 , 423 K and -40 m/s, respectively with zero amplitude turbulence levels. The

simulated records of time-resolved density, temperature, and velocity data for this sample case are presented in figures 3.10, 3.11, and 3.12, respectively. The red line represents the actual values provided as input in the simulation code and the blue line represents the resulting values determined by MLE analysis of the noisy photon count data. The rms error is indicated in each figure. Similar data was generated for velocities ranging from 0 to -200 m/s and temperatures of 298 K, 423 K, and 573 K. The rms error in temperature and velocity for the range of cases explored are summarized in figures 3.13 and 3.14, respectively. The rms error should be greater than the lower bound uncertainty estimates shown in figures 3.6 and 3.7 since any estimator for a parameter has a variance which cannot be less than the Cramer-Rao lower bound. Analysis was attempted for a temperature of 773 K however extremely low signal-to-noise levels caused severe instabilities in the MLE analysis causing the data analysis program to crash. This indicates that a lower sampling rate should be used for experiments involving flows exceeding ~600 K for the optical system parameters used in this work. A general figure of merit to use when configuring an experiment is that the total counts detected at the output of the interferometer ($N_{PMT 1} + N_{PMT 2} + N_{PMT 3} + N_{PMT 4}$) should be greater than 110.

In figures 3.11 and 3.12, large excursions in the temperature and velocity measurements that exceed the expected measurement variance and cause the variation of the measurements to be asymmetrical about the mean value are evident. The common feature among these statistical outliers is that they either took more than 10 iterations to converge or never converged (maximum iterations was set to 40). The majority of data that falls

within the expected variance limits converged in 6 iterations or less. The solutions that fail to converge properly tend to march in the same direction (towards higher temperature or more negative velocity) as the iterations increase in an attempt to converge on a solution which causes the asymmetry in the data. Statistical outliers such as these can be avoided by setting stricter limitations on the maximum number of iterations or replacing the statistical outliers with an average of surrounding data points.

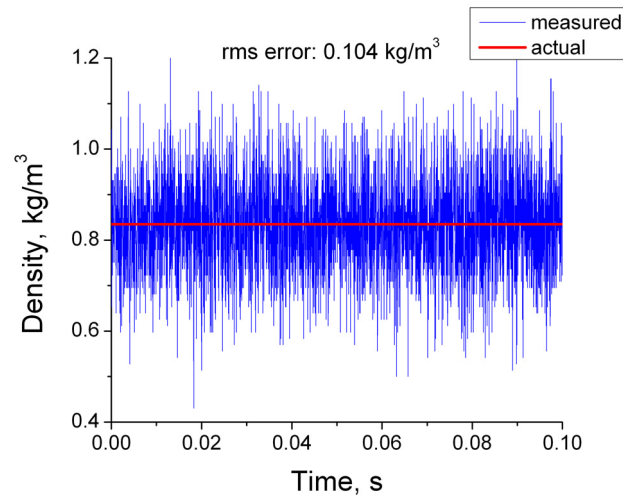


Figure 3.10. Simulated time-resolved density data at 32 kHz data rate.

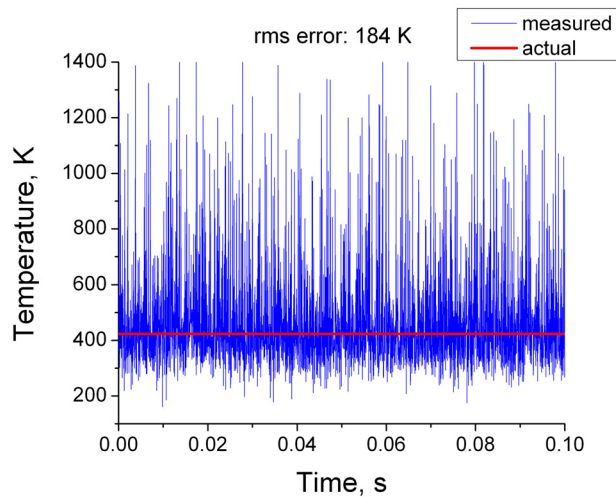


Figure 3.11. Simulated time-resolved temperature data at 32 kHz data rate.

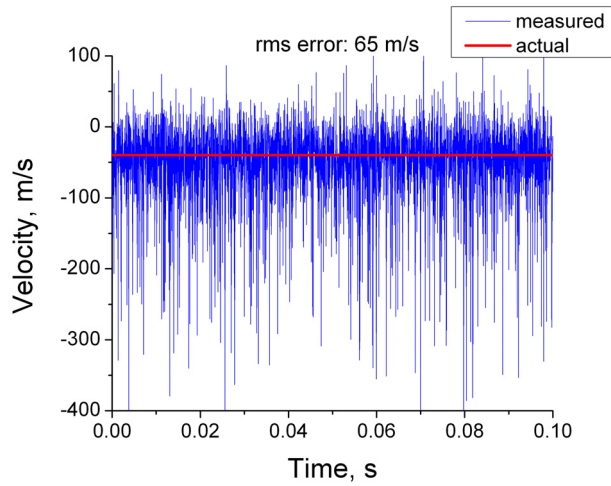


Figure 3.12. Simulated time-resolved velocity data at 32 kHz data rate.

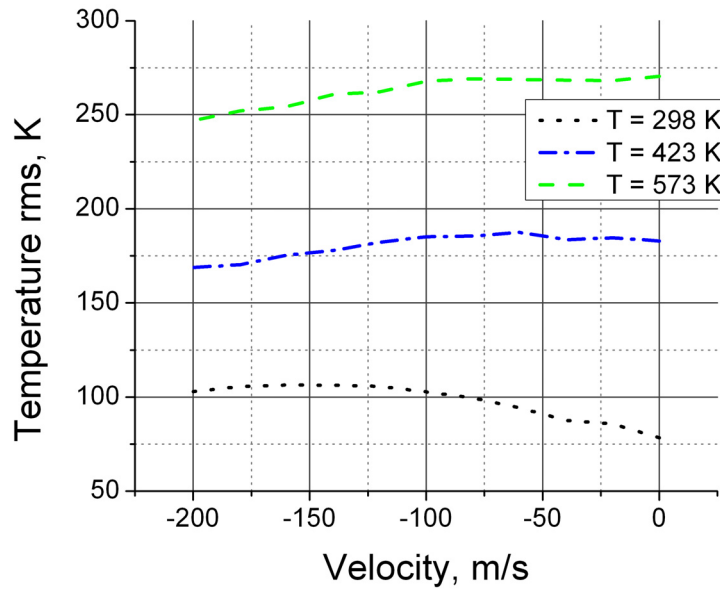


Figure 3.13. Temperature rms error based on simulated data analysis over the expected temperature and velocity ranges for a sampling rate of 32 kHz.

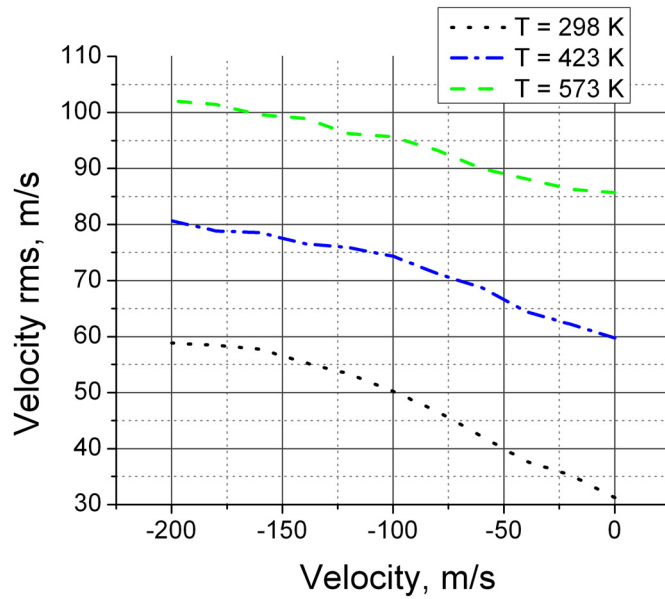


Figure 3.14. Velocity rms error based on simulated data analysis over the expected temperature and velocity ranges for a sampling rate of 32 kHz.

The mean density, temperature, and velocity were subtracted from their respective time history records to provide zero-mean records, which were used to calculate the power spectral densities of the property fluctuations. The power spectra of the 1.28 second time records were calculated using a technique called the Welch method of modified periodograms, which provides an average of several shorter overlapped periodograms to minimize the variance in the spectral estimates (Welch, 1967). The resulting power spectra provide fluctuation information out to 16 kHz with 7.8125 Hz resolution, and the sum of all points in the spectra is equivalent to the mean square fluctuations. Figures 3.15, 3.16, and 3.17 show the density, temperature, and velocity power spectra calculated from the data represented in figures 3.10, 3.11, and 3.12, respectively. Since the actual data is steady (no fluctuations) in these simulation studies the power spectrum calculations provide insight into the uncertainty or noise levels in these calculated second

order statistical values. The broadband shot noise causes a pedestal or offset in the power spectrum. This baseline noise floor provides the lower limit of measurable property fluctuations. The fluctuation baseline or lower limit was calculated using the spectral noise floor and frequency resolution of the power spectrum and is indicated in figures 3.15-3.17 for simulated data at 423 K and -40 m/s. A summary of the temperature and velocity spectral noise floors for the range of temperatures and velocities explored in these simulation cases are provided in figures 3.18 and 3.19, respectively. The temperature and velocity fluctuation amplitude lower bound calculated from the spectral noise floor values are summarized in figures 3.20 and 3.21, respectively. The uncertainty in the fluctuation estimates (2nd order statistics) is significantly lower than the uncertainty in instantaneous value estimates. This conclusion is based on comparison of figure 3.13, which provides the rms error in instantaneous temperature estimates and figure 3.20, which provides the lower bound of temperature fluctuation estimates, and likewise comparisons of figures 3.14 and 3.21 for instantaneous velocity and fluctuation estimates.

Simulated data were also generated to compare with experimental data acquired in the velocity and temperature fluctuation validation studies. In these simulations a time record of oscillating temperature or velocity similar to the values expected in the experiments was provided as input for the simulation by assuming a sinusoidal flow response to a sinusoidal acoustic excitation. The results of these simulation studies will be discussed in Chapter 5 with the experimental data.

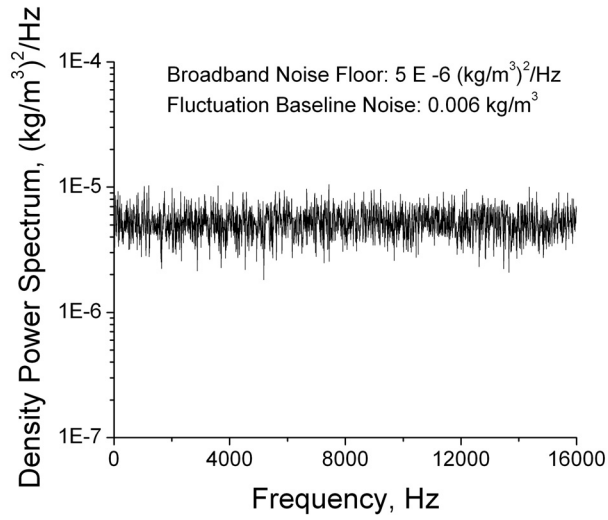


Figure 3.15. Density power spectrum calculated using the data from figure 3.10.

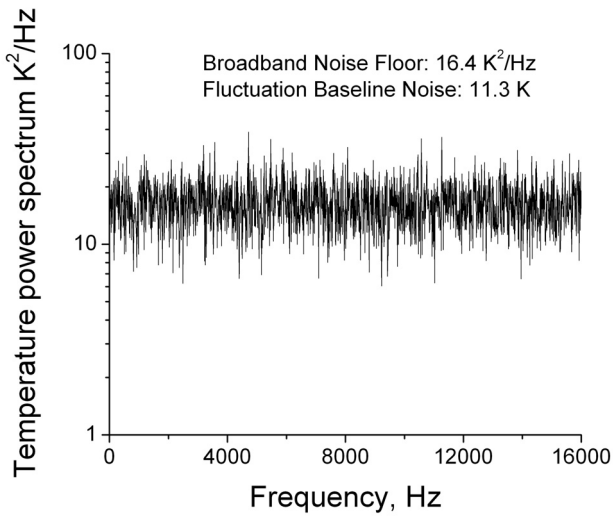


Figure 3.16. Temperature power spectrum calculated using data from figure 3.11.

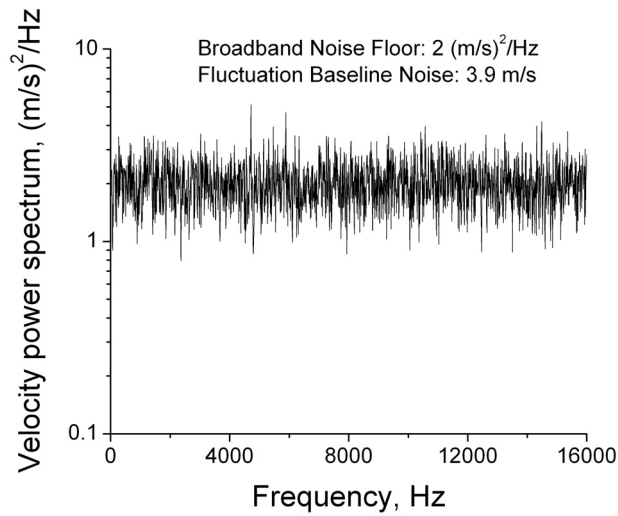


Figure 3.17. Velocity power spectrum calculated using the data from figure 3.12.

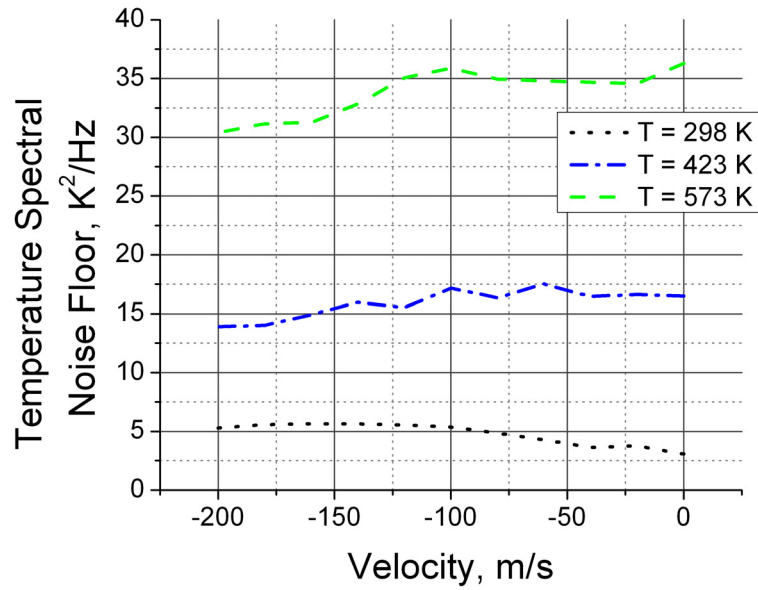


Figure 3.18. Temperature spectral noise floor based on simulated data analysis over the expected temperature and velocity ranges at a sampling rate of 32 kHz.

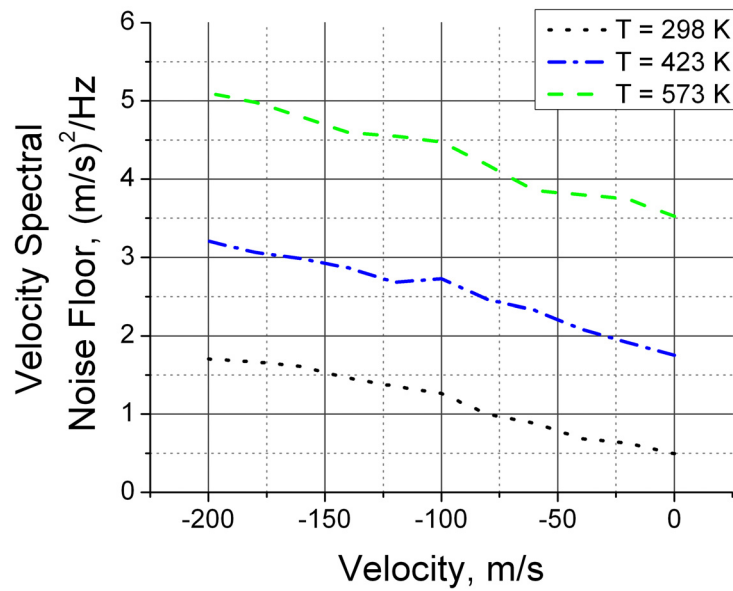


Figure 3.19. Velocity spectral noise floor based on simulated data analysis over the expected temperature and velocity ranges at a sampling rate of 32 kHz.

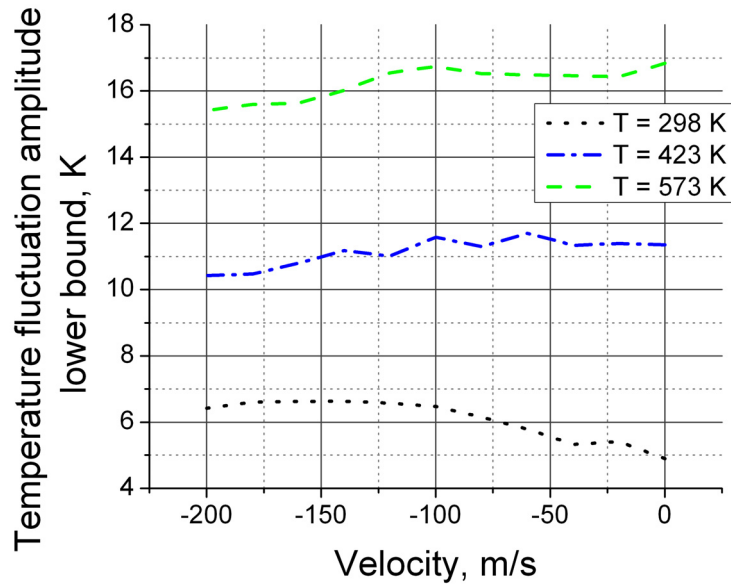


Figure 3.20. Temperature fluctuation amplitude lower bound based on spectral noise floor values presented in figure 3.18.

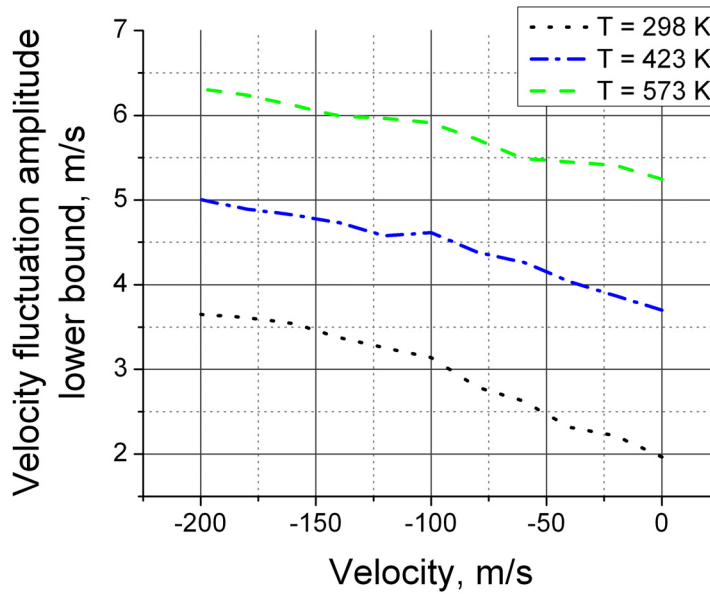


Figure 3.21. Velocity fluctuation amplitude lower bound based on spectral noise floor values presented in figure 3.19.

CHAPTER 4

EXPERIMENTAL SETUP AND PROCEDURE

4.1 Introduction

Three jet flow systems were used to evaluate the performance of the Rayleigh scattering flow diagnostic. First, an acoustically modulated unheated nozzle flow was used to validate velocity fluctuation measurements. The amplitude and frequency of the velocity fluctuations were verified by constant temperature anemometry (CTA) or hotwire measurements. Next, an asymmetric oscillating counterflow with unequal enthalpies was used to evaluate the ability of Rayleigh scattering to measure temperature and density fluctuations accurately by comparison with constant current anemometry (CCA) or coldwire measurements. Finally, a high speed electrically-heated jet flow was used to evaluate the ability to measure all three flow properties simultaneously in a relevant flow facility. The details of the three experiments will be discussed in this chapter.

4.2. Measurement approach

A high power continuous-wave laser beam is focused at a point in the air flow field and Rayleigh scattered light is collected and spectrally resolved. The spectrum of the light, which contains information about the temperature and velocity of the flow, is analyzed using a Fabry-Perot interferometer. The circular interference fringe pattern is divided into four concentric regions, as shown in figure 4.1, using an image dissector that will be described in section 4.6. The total light in the innermost circular region of the fringe image is focused on the detector of PMT 1. The total light in the annular region closest to the center circular region is focused on the detector of PMT 2. The light in the next

annular region is detected by PMT 3, and the light in the outermost annular region is measured by PMT 4. The photons are sampled at rates up to 32 kHz using photon counting electronics such that each sample consists of the number of photons detected during the integration time (i.e., 31.25 μ s for 32 kHz sampling rate). Monitoring the relative change in intensity within each region allows for measurement of gas temperature and velocity. Independently monitoring the total scattered light intensity provides a measure of gas density.

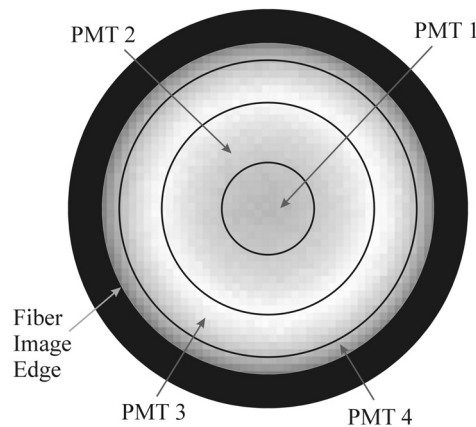


Figure 4.1. Dissection of Fabry-Perot fringe pattern into one circular and three annular regions.

4.3. Acoustically modulated nozzle flow

In the first experiment, flow measurements were performed in an air stream issuing from a jet consisting of a converging nozzle with a 10 mm exit diameter (figure 4.2). The jet was coupled to a loudspeaker (AUDAX model HT130F0 Bass Midrange Fiberglass Cone Driver), which provided pressure waves that induced velocity fluctuations of a known driving frequency in the exiting flow. A function generator (Stanford Research model DS345) provided a sine wave input to the amplifier (Altec Lansing model 1268), which

allowed variation of the signal amplitude sent to the speaker diaphragm. Since the measurement technique relies on having particulate free gas flow, a series of filters were placed in line with the air plumbing to remove dust, oil and water from the air supply; however due to the lack of a surrounding filtered co-flow, measurements could only be made in the clean core flow of the jet stream to avoid scattering from particles entrained from the surrounding room air. Figure 4.2 shows the layout of the optics around the jet, which were used to collect Rayleigh scattered light from gas molecules in the flow. A photograph of the jet system, laser beam and collection optics is shown in figure 4.3. Most of the beam propagation path from the laser head to the probe volume location has been covered over with black aluminum foil to eliminate stray laser light from corrupting the Rayleigh scattering signal. The jet was mounted such that the main flow direction was parallel to the table. A Coherent Verdi model V-10 10W, 532 nm wavelength, single-frequency, Nd:Vanadate cw laser provided incident light for the system. The laser beam was focused with a 250 mm focal length lens (L1) to a $70 \mu\text{m } 1/e^2$ diameter at the probe volume d_{PV} , as determined by the beam waist diameter calculation from Gaussian beam propagation analysis: $d_{PV} = \frac{4\lambda f_{L1}}{\pi d_{beam}}$, where f_{L1} is the focal length of lens L1 and d_{beam} is the laser output beam diameter. The beam was oriented in the horizontal plane, at a 45° angle to the primary flow direction. Light was collected at a 90° scattering angle, collimated by a $f/4$ 200 mm focal length lens (L2) that provided a solid angle of 0.05 steradians, and focused by a $f/2$ 100 mm focal length lens (L3) onto a 0.55 mm diameter multimode optical fiber with numerical aperture of 0.22. The numerical aperture of the $f/2$ focusing lens nearly matched that of the optical fiber to maximize the amount of light coupled into the fiber. Since the pair of lenses provided 1:2 imaging, the length of the

probe volume in the beam propagation direction was 1.1 mm; however the resolution in the axial direction, which the direction of the velocity gradient of interest, was 0.78 mm. The incident and scattering wave vectors were arranged such that the axial component of the jet velocity was measured, as shown by the \vec{K} vector in figure 4.2. The 1.1 mm probe volume was positioned two jet diameters from the nozzle exit on the flow centerline. The probe volume could not be positioned any closer to the nozzle exit in this configuration due to clipping of the laser beam by the jet hardware. The jet was operated at a mean (steady flow) exit velocity of approximately 10 m/s and static temperature of 295 K, giving a Reynolds number (Re) on the order of 10^4 . An oscillating (unsteady) flow field was produced by driving the loudspeaker at a frequency of 50 Hz at fixed amplitude.

For calibration purposes, the mean temperature, density, and velocity at the probe location in a steady flow were calculated via isentropic flow and ideal gas relations using total pressure and temperature measurements acquired by pressure probe and type K thermocouple measurements in the jet plenum and static pressure measurements from an ambient pressure probe. The calibration data was obtained at jet conditions covering a plenum (total) pressure range of 100 – 110 kPa, which provided axial velocities in the jet core of 10 – 140 m/s (Mach 0.03 – 0.40) and temperatures of 289 – 298 K. The ambient pressure was 98.5 kPa. The velocity fluctuations were verified using a CTA (hotwire anemometry) system. A TSI probe (model 1210-T1.5) with a single 3.8 μm diameter, 1.25 mm long platinum-coated tungsten resistance wire with temperature coefficient of resistance of $4.2 \times 10^{-3} \text{ K}^{-1}$ was used with a TSI model IFA-100 thermal anemometry system operated in a constant temperature configuration using an overheat ratio of 1.4.

The frequency response of the CTA system was measured to be greater than 100 kHz for the flow velocities encountered in this experiment. The CTA measurements were obtained at the same location and jet conditions as the Rayleigh data, but were acquired on a different day. Hotwire anemometry has the disadvantage of directional ambiguity in the velocity measurements; the Rayleigh scattering technique is capable of measuring both positive and negative velocities in the direction of the \vec{K} vector. The interference fringe radius will increase for positive velocities and decrease for negative velocities.

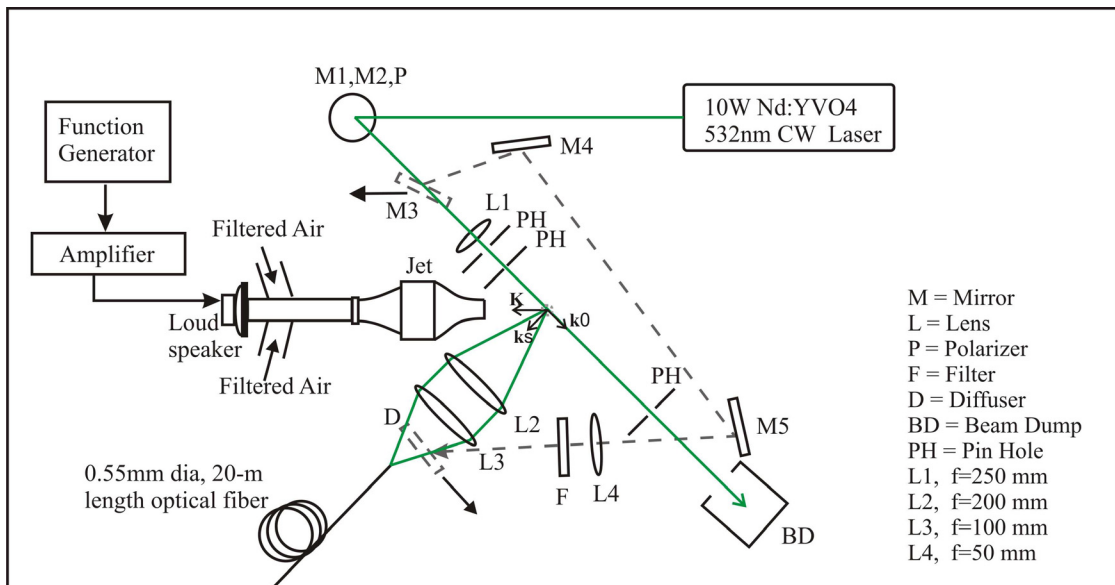


Figure 4.2. Diagram of laser and collection optics for acoustically-excited nozzle flow experiment.

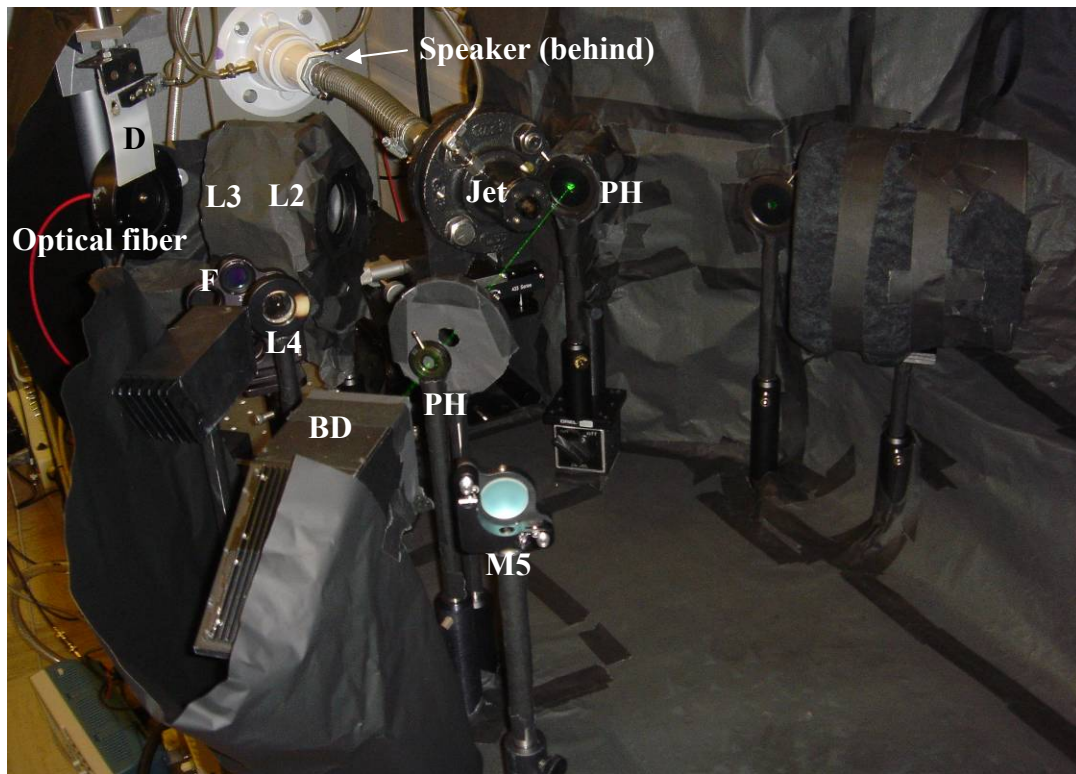


Figure 4.3. Photograph of acoustically-excited nozzle flow experiment. See figure 4.2 for label descriptions.

4.4 Asymmetric oscillating counterflow with unequal enthalpies

In the second experiment, measurements were performed in the flow between opposed heated and unheated air jets issuing from nozzles with 10 mm exit diameters and 20 mm separation distance (figure 4.4). The unheated jet hardware was identical to that described in the previous section. The filtered air issuing from the opposing jet was heated by applying voltage to coils of kanthal wires inside the jet plenum. The output temperature remained sufficiently steady by applying a constant voltage to the wires while maintaining a fixed air mass flow rate. The temperature of the heated jet was set by monitoring a 30 gauge wire (0.25 mm bead diameter) open-bead type K thermocouple placed at the jet exit. The loudspeaker was used in this experiment to generate an

oscillating flow providing large temperature fluctuations at the probe volume location. Figure 4.4 shows the layout of the optics around the opposed jet system. Figure 4.5 shows a 3D rendering of the opposed jet system along with the laser beam and optical components, and figure 4.6 provides a photograph of the opposed jets with the laser beam passing in the region between the nozzle exits. The jets were mounted such that the main flow direction was parallel to the table and the nozzle exits were separated by two jet diameters. The Coherent Verdi 10W, 532 nm wavelength laser beam was focused with a 250 mm focal length lens (L1) to a $70 \mu\text{m}$ $1/e^2$ diameter at the probe volume. The beam was oriented in the vertical direction, orthogonal to the primary flow direction. Light was collected at a 90° scattering angle using identical collection optics as described in the previous section, which imaged a 1.1 mm length of the focused beam at the fiber face. The probe volume was oriented such that the beam waist, which provides the smallest probe volume dimension, was oriented in the direction of the maximum temperature gradient (the axial direction). Therefore, the resolution in the direction of interest is $70 \mu\text{m}$. The incident and scattering wave vectors were arranged such that the radial component of the jet velocity was measured, as shown by the \vec{K} vector in figure 4.4b. This arrangement was chosen so that velocity fluctuations were minimized since the radial component of the centerline velocity is approximately 0 m/s. The unheated air jet was operated at a mean axial velocity of approximately 10 m/s at the exit and static temperature of 295 K ($\text{Re} \sim 10^4$). The heated air jet was operated at a static temperature of 425 K and the location of the maximum temperature gradient was positioned approximately half-way between the two nozzles by adjusting the heated jet flow rate. A shadowgraph system was used to monitor the location of the maximum temperature

gradient in the flow. The shadowgraph system consisted of a collimated 18 mm diameter HeNe laser beam that propagated through the flow perpendicular to the main flow direction and was projected onto an imaging screen located approximately 300 mm from the jet flow centerline. Figure 4.7 shows a photograph of the shadowgraph image plane. The imaging screen contains 1 mm x 1 mm squares. Outlines of the nozzle locations are indicated on the left and right sides of the 18 mm diameter laser spot. The region of reduced light intensity (outlined in white) that is centered approximately 9 mm from the hot jet exit is due to deflection of the collimated light rays resulting from the large temperature gradient in the flow. The Rayleigh probe volume was positioned 7 mm from the hot jet exit on the flow centerline where the temperature fluctuations were maximized for an excitation frequency of 100 Hz, as determined by CCA temperature probe measurements.

For system calibration purposes, steady flow static temperature and pressure measurements at the probe location were measured by a 30 gauge wire type K thermocouple and an ambient pressure gauge (Mensor model 2101). Gas density information was derived from these measurements using the ideal gas law. For calibration, the mean radial velocity component was assumed to be 0 m/s while the heated jet was operated over a temperature range of 298 K to 528 K. A CCA (coldwire thermometry) system provided static temperature fluctuation measurements in unsteady flows to validate the dynamic Rayleigh technique. A TSI probe (model 1276-P.5) with a 1.3 μm diameter, 0.9 mm long platinum resistance wire with temperature coefficient of resistance of $3.85 \times 10^{-3} \text{ K}^{-1}$ was used with a TSI 1745 constant current anemometer at a

current setting of 0.4 mA. The smallest wire diameter offered from TSI was chosen to minimize thermal inertia and maximize the frequency response of the instrument. The frequency response of the CCA system to a step input, based on the 3 dB point, was measured to be 1 kHz for a flow velocity of 10 m/s. Pietri et al. (2000) recommend a wire length-to-diameter ratio of 700 or greater to minimize end effects due to heat loss through the prongs and the development of boundary layers around the prongs. The length-to-diameter ratio is approximately 700 for the probe chosen here. The anemometry module consists of a Wheatstone bridge, which includes the coldwire in one of its branches, and an amplification stage with a tuning gain and an off-set. The gain and off-set were set such that the full range of the digitization board (± 10 V) was optimized for temperatures ranging from room temperature to 423 K, which was the maximum operating temperature for the platinum wire. CCA measurements were obtained at the same jet conditions as the Rayleigh data; however they were not obtained simultaneously.

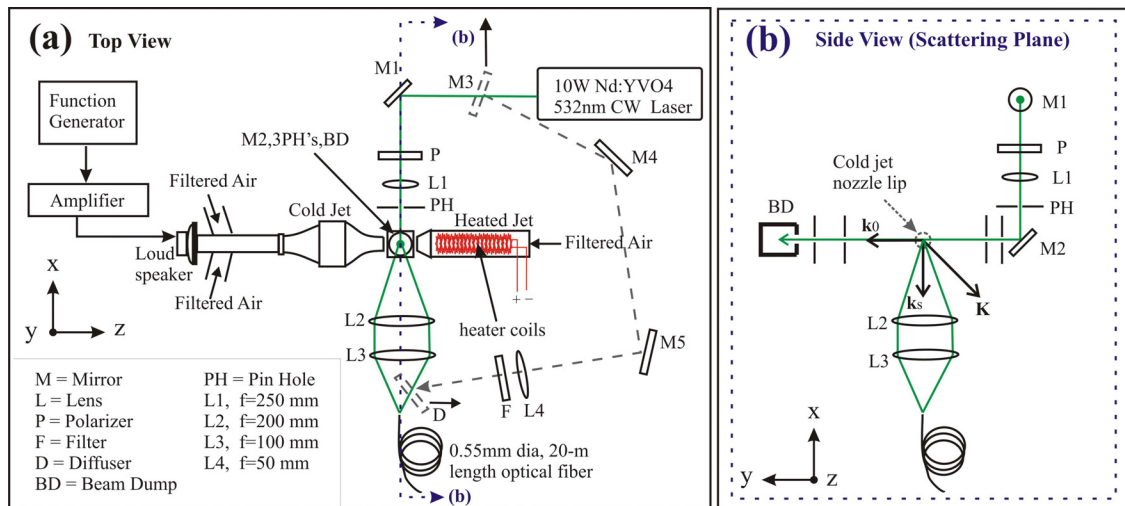


Figure 4.4. Diagram of laser and collection optics for asymmetric oscillating counterflow experiment.

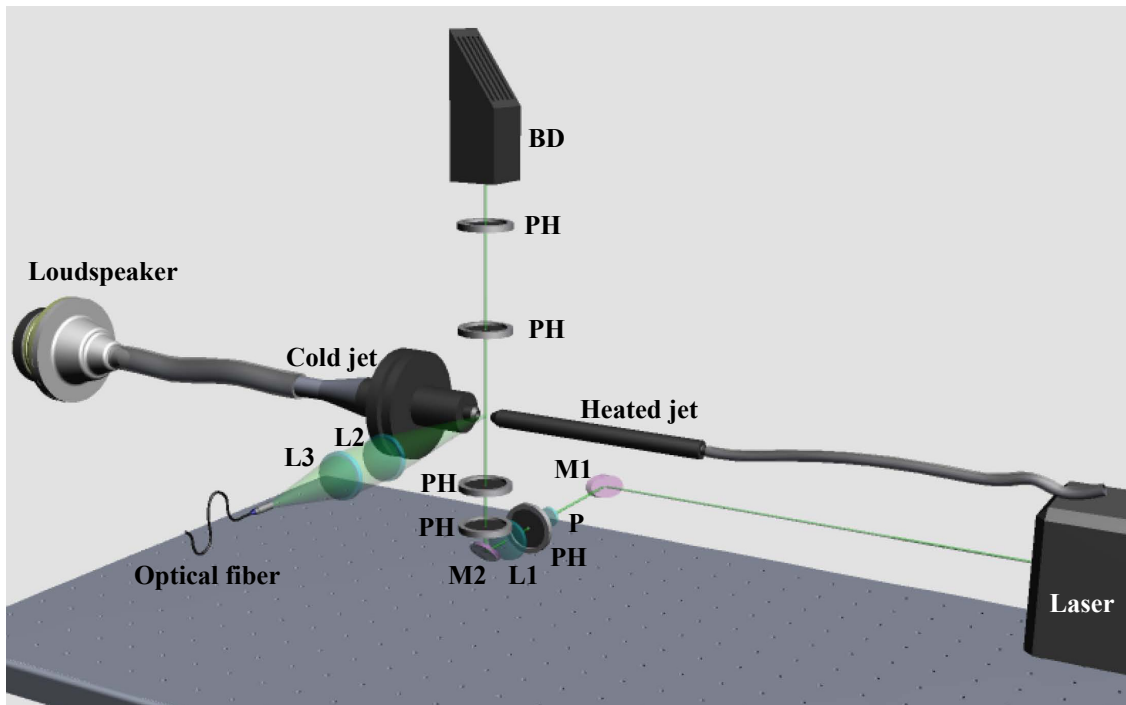


Figure 4.5. 3D schematic of asymmetric oscillating counterflow experiment. See figure 4.4 for label descriptions.

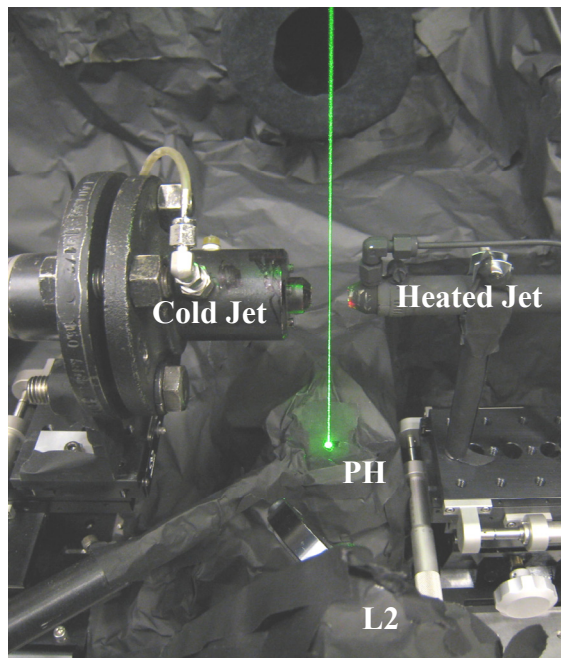


Figure 4.6. Photograph of the laser and opposed hot and cold jets in the asymmetric oscillating counterflow experiment. See figure 4.4 for label descriptions.

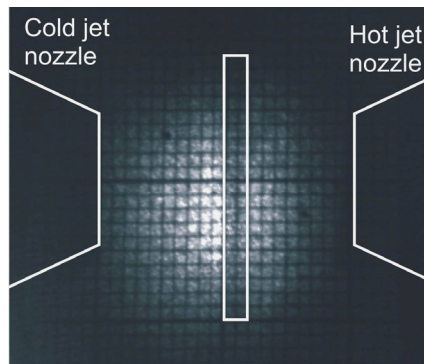


Figure 4.7. Photograph of the shadowgraph image plane.

4.5 High speed electrically-heated jet

In the final experiment, flow measurements were acquired in an electrically heated air flow issuing from a 10 mm exit diameter convergent nozzle with a 200 mm diameter 10 m/s filtered air co-flow (figure 4.8). The air supplied to the nozzle passed through a series of filters in line with the air plumbing to remove dust, oil and water from the air supply prior to entering the nozzle flow system. The co-flow was provided by an air blower system equipped with submicron HEPA filters. Figure 4.8 shows the layout of the optics around the jet, which were used to collect Rayleigh scattered light from gas molecules in the flow, and figure 4.9 shows a photograph of the experiment setup. The jet was mounted such that the main flow direction was parallel to the table. The Coherent Verdi 10W, 532 nm wavelength cw laser provided incident light for the system. The laser beam was focused with a 250 mm focal length lens (L1) to a $70 \mu\text{m } 1/e^2$ diameter at the probe volume. The beam was oriented in the horizontal plane, at a 45° angle to the primary flow direction. Light was collected at a 90° scattering angle, collimated by a $f/4$ 200 mm focal length lens (L2), and focused by a 100 mm focal length lens (L3) onto a 0.55 mm diameter multimode optical fiber. Since the pair of lenses provided 1:2 imaging, the

length of the probe volume was 1.1 mm. The incident and scattering wave vectors were arranged such that the axial component of the jet velocity was measured, as shown by the \vec{K} vector in figure 4.8. The jet was mounted on vertical and horizontal translation stages so that the probe volume could be positioned anywhere in the jet plume. The probe volume with resolution of 0.78 mm was positioned two jet diameters from the nozzle exit and was scanned radially at 1 mm increments across the flow providing velocity, density, and temperature profiles at various flow conditions. The jet was operated at a mean (steady flow) exit velocity that covered a range of approximately 10 – 110 m/s and static temperature range of 295 - 775 K, giving a Reynolds number range of $10^3 - 10^5$. The jet temperature was set by observing the output of a thermocouple in the jet plenum. A fixed power level was applied to the coils, which maintained a fixed air temperature for a fixed flow rate.

For calibration purposes, temperature, density, and velocity measurements were acquired in a steady laminar flow in the jet core. The mean static temperature at the probe volume location and the ambient air temperature were measured by 36 gauge wire (0.13 mm bead diameter) type K thermocouples. Since thermocouples measure the temperature of the metal probe bead rather than the gas temperature, there may be a difference between the actual gas temperature and the thermocouple measurement. These differences result from conduction losses down the thermocouple wire and radiation losses to the surroundings. The error in thermocouple-measured gas temperature was estimated to be less than 5 K for the temperatures studied here. Two Mensor model 2101 digital pressure gauges measured the ambient (static) pressure and the jet plenum (total) pressure. The velocity

and density at the probe location within the core flow were calculated via isentropic flow and ideal gas equations using total and static pressure and ambient temperature measurements. The calibration data was acquired in the core flow over a temperature range of 298 K to 765 K and a velocity range of 14 m/s to 115 m/s. The velocity and temperature fluctuations were verified using the CTA (hotwire anemometry) and CCA (coldwire anemometry) systems discussed previously. The hotwire and coldwire systems could not be used at all flow conditions due to physical limitations of the devices. Both of the fine wire probes were limited to a maximum temperature of 423 K. Also, the single wire hotwire system is not valid in flows with large temperature fluctuations, and the calibration must be performed at the flow temperature in which measurements are desired. Therefore, the hotwire measurements were performed in unheated flows with similar mean velocities as the corresponding heated cases. The coldwire probe broke when it was subjected to a flow velocity of 110 m/s; therefore CCA data is only available at low speed flow conditions. The jet velocity profiles at heated conditions were evaluated from total pressure measurements with a 0.5 mm I.D. pitot probe and SETRA model 239 differential pressure gauge; however these measurements provided mean velocity information only. The CTA, CCA, and pitot probe measurements were obtained at the same location as the Rayleigh data, but were acquired on a different day.

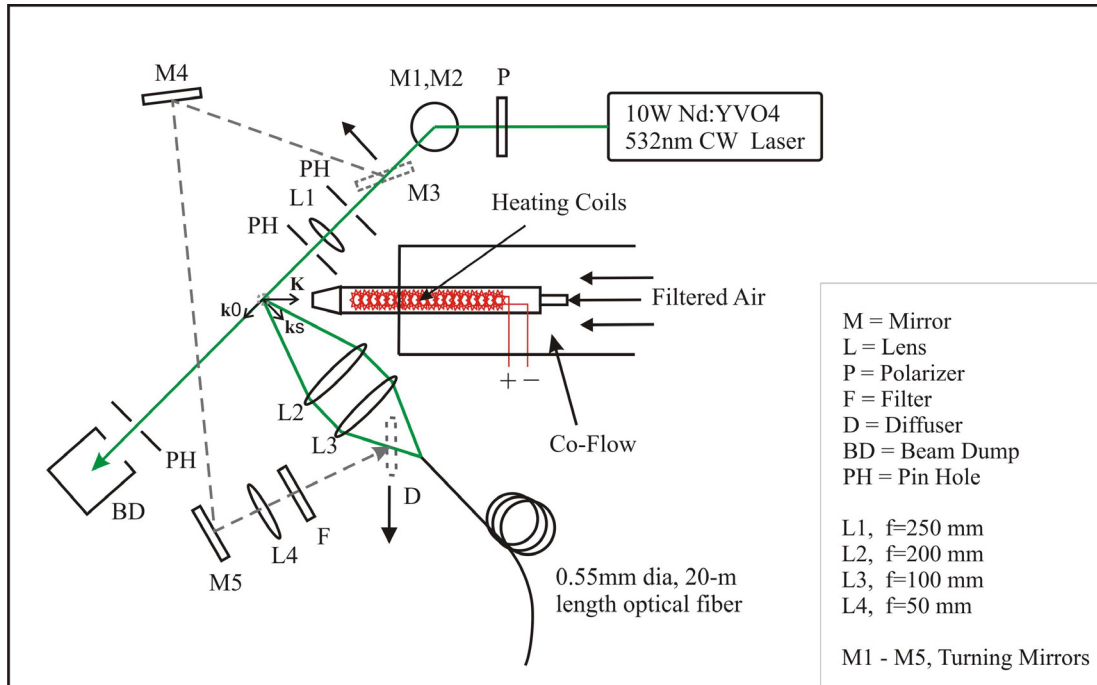


Figure 4.8. Diagram of laser and collection optics for high speed heated jet experiment.

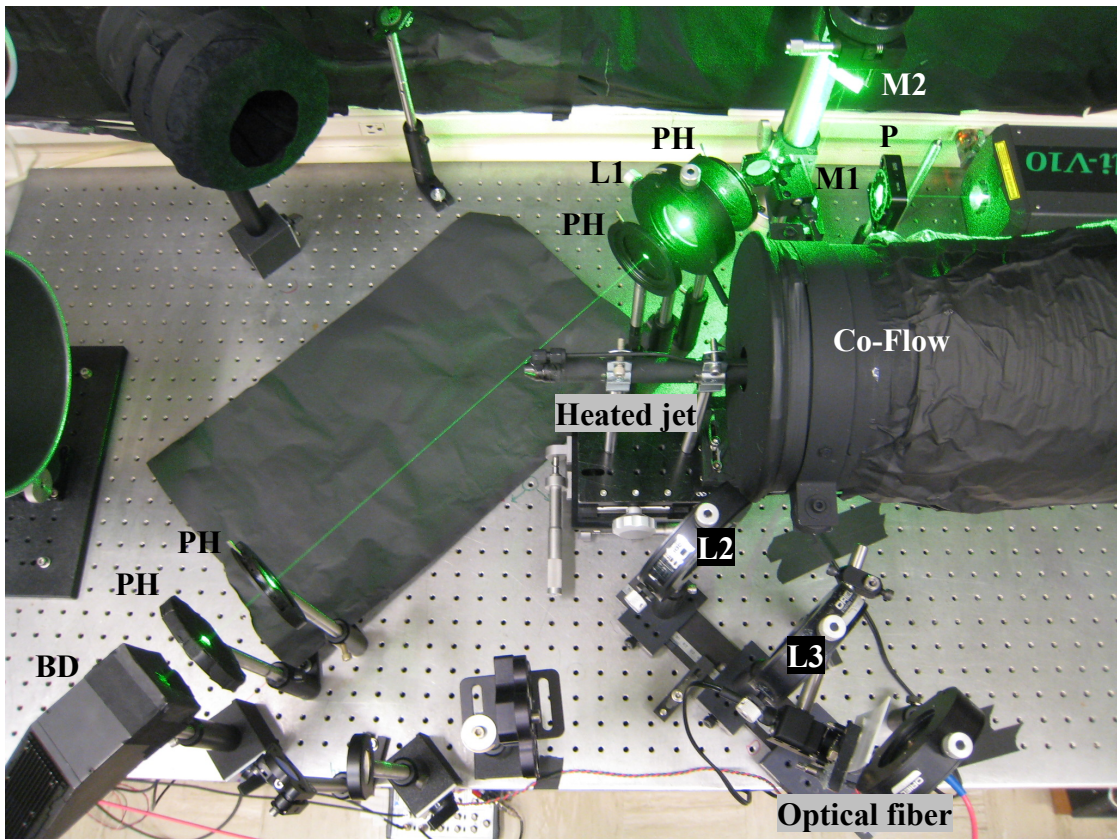


Figure 4.9. Photograph of the high speed heated jet experiment. See figure 4.8 for label descriptions.

4.6 Spectral analysis and detection optics

The spectral analysis and detection optics were identical for all three experiments. Upon collection of the Rayleigh scattered light by the 0.55 mm diameter multimode fiber, it was routed to a separate optical table, shown schematically in figure 4.10. The light exiting the fiber was collimated by an 80 mm focal length $f/1.6$ lens (L5) and was directed through the planar mirror Fabry-Perot interferometer. The FPI had 70 mm diameter mirrors with 80% reflectivity, 8.7 GHz free spectral range (*FSR*), and reflective finesse of approximately 15. The Fabry-Perot is an extremely sensitive instrument; even the smallest vibrations or temperature changes can cause the mirrors to drift out of parallel alignment, resulting in increased uncertainty. Therefore, a stabilization system was utilized to maintain parallelism of the mirrors during testing. Between Rayleigh scattering measurements, a mirror and diffuser (shown in dashed gray lines in Figs. 4.2, 4.4, and 4.8) were placed in the beam path by linear actuators to direct some of the incident laser beam into the optical fiber and through the FPI. Figure 4.11 shows a 3D rendering of the laser beam routing for Fabry-Perot stabilization in the asymmetric oscillating counterflow experiment. A set of reflecting prisms mounted on a linear actuator (figure 4.10) were positioned in the optical path at the output of the interferometer to direct the light from three regions of the interferometer mirrors to a video camera. Live video of the three fringe images was used in a feedback control loop to adjust the mirror positions by controlling the voltage applied to piezoelectric transducers on the mirror mounts until the three fringes were equal in diameter indicating that the mirrors are equally spaced at all three locations. This system was also used to set

the fringe diameter of the incident reference light to 13 mm, which was the optimum fringe diameter determined from the uncertainty analysis.

When flow measurements were acquired, the prisms, mirror, and diffuser were removed from the optical path and the Rayleigh scattered light exiting the FPI was focused by a fringe forming lens (L6) having an effective focal length of approximately 2700 mm, which provided a 18.6 mm diameter image of the fiber face. Light from circular and annular sections of the image were directed toward PMTs by a concentric elliptical mirror system, which was designed and fabricated specifically for this application. A photograph of the 'image dissector' is shown in the upper left corner of figure 4.10. The mirrors were machined from 6061 aluminum and the 12° elliptical surfaces were diamond polished to a mirror finish with about 90% reflectivity. The mirror diameters, from innermost to outermost, are 5 mm, 12 mm, 16 mm, and 25 mm. Each mirror sends the respective portion of the fringe image toward PMTs 1, 2, 3, and 4 (figure 4.1). A 19.2 mm diameter aperture was centered at the image plane to eliminate stray light and ghost images outside of the fiber image region from being directed by the outermost mirror onto the detector of PMT 4.

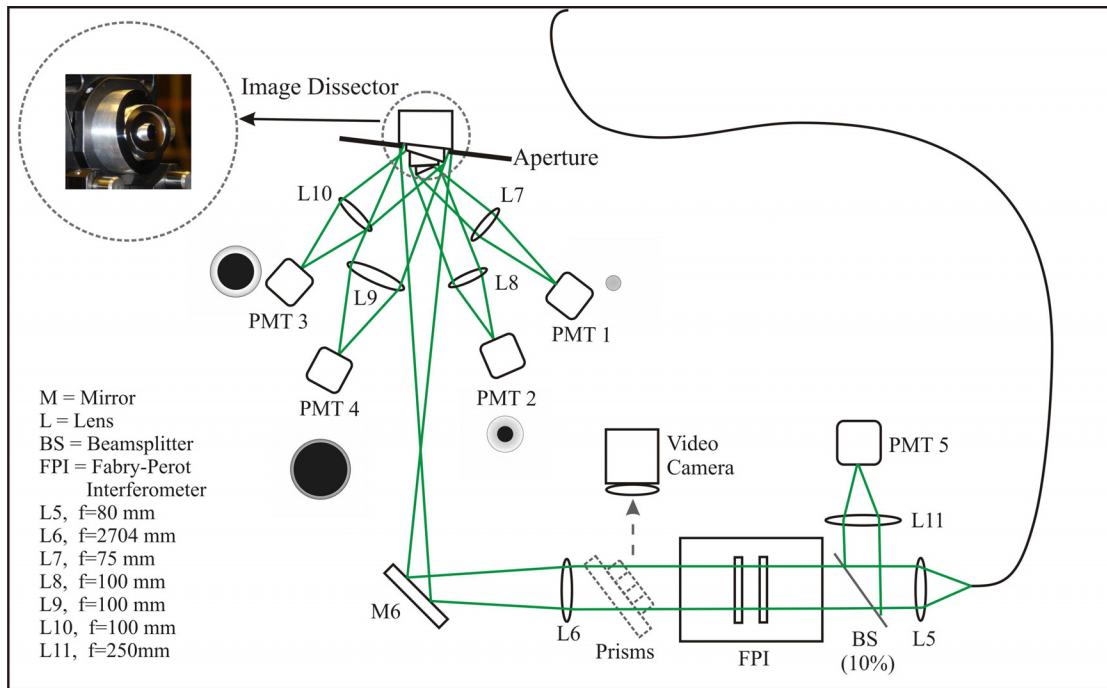


Figure 4.10. Schematic of spectral analysis and detection optics.

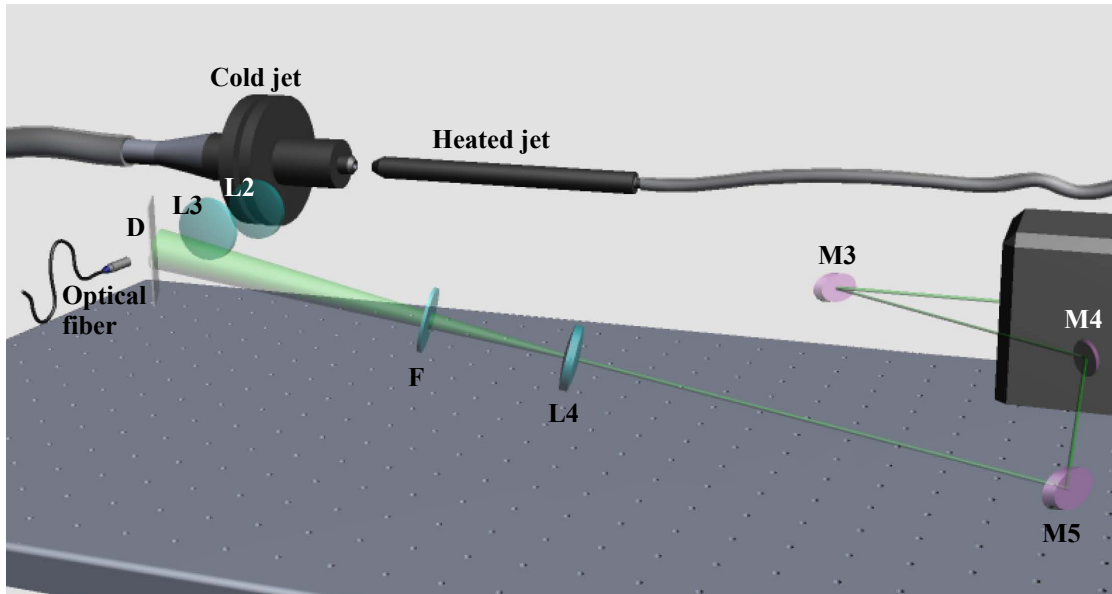


Figure 4.11. 3D schematic of the asymmetric oscillating counterflow experiment collection optics with the laser beam propagation configured for Fabry-Perot stabilization. See figure 4.4 for label descriptions.

The PMTs were operated in the photon counting mode to acquire fringe intensity data. Figure 4.12 provides a schematic of the pulse counting and data acquisition hardware. Each PMT was supplied with 1200 V and equipped with a “snubber” consisting of a 0.25-m length of RG-58 cable terminated with a 0 – 40 Ω variable resistance potentiometer. The resistance of the potentiometer was set by monitoring individual photoelectron pulses using a high bandwidth oscilloscope and adjusting the resistance until the shape of the pulse was optimized (i.e., narrow pulse with minimal post-pulse ringing). The varying amplitude photoelectron pulses from the five PMTs were amplified by Stanford Research model SR445 pre-amplifiers with a gain of 5 and were counted by Stanford Research model SR400 photon counters, which output 6 ns wide NIM level (-700 mV) pulses for each incoming photoelectron pulse having an amplitude exceeding the threshold level. Typical threshold levels ranged from -25 mV to -50 mV for the five PMTs. Canberra model 2126 constant fraction discriminators converted the NIM level pulses to 8 ns wide TTL level (+2.5 V) pulses that were counted by two National Instruments model 6602 counter-timer boards. Typical photoelectron count rates for this work were on the order of 1 MHz. A PC-based data acquisition system utilizing National Instruments data acquisition hardware and LabVIEW software was used to record the signals from the PMTs. Each signal channel was digitized at 1, 16 or 32 kHz sampling rate for 60 seconds (or 10 seconds in the case of the 32 kHz rate), resulting in 60,000, 960,000, or 320,000 samples per channel. The intensity information from the Fabry-Perot fringe sampling was used to obtain temperature and velocity measurements. The density measurement was much simpler, requiring only an overall intensity measurement. A beamsplitter located just in front of the FPI input (figure 4.10) directed approximately

10% of the incoming Rayleigh scattered light to a lens (L11), which focused the light at PMT 5 for the density measurement.

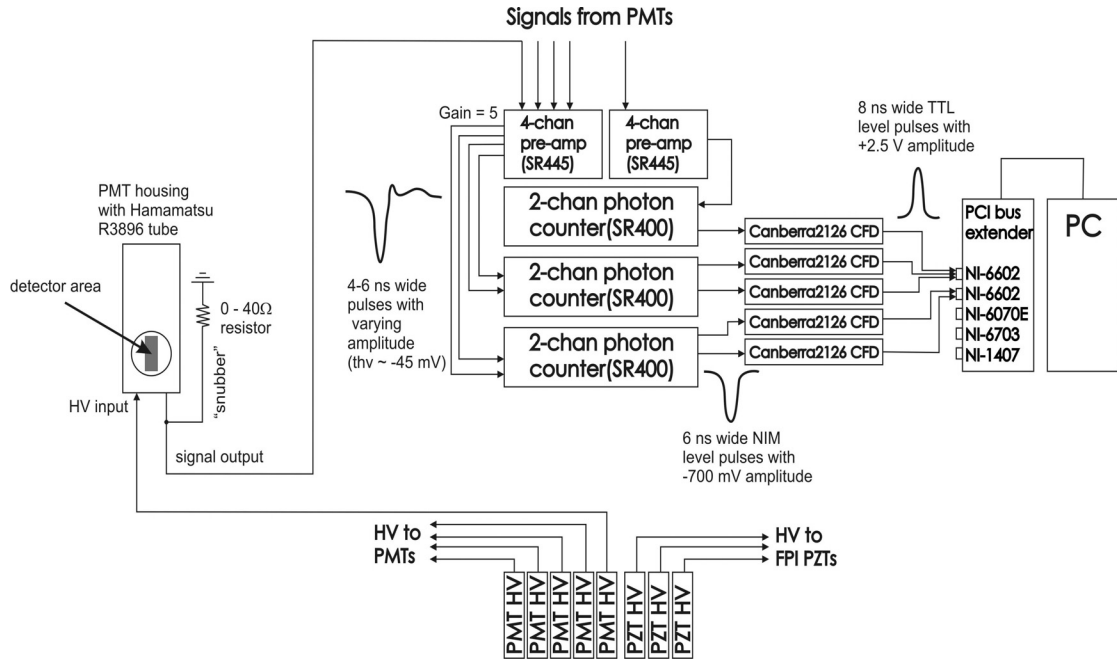


Figure 4.12. Photon counting electronics and data acquisition hardware schematic.

CHAPTER 5

RESULTS AND DISCUSSION

5.1 Introduction

The results of the Rayleigh measurements in three jet flow experiment configurations used to evaluate the performance of the Rayleigh scattering flow diagnostic are presented in this chapter. Velocity fluctuation measurements acquired in an acoustically modulated unheated nozzle flow are compared with hotwire measurements. Temperature and density fluctuations in an asymmetric oscillating counterflow with unequal enthalpies are compared with coldwire measurements. Finally, measurements in a high speed electrically-heated jet are used to evaluate the ability to measure all three flow properties simultaneously in a relevant flow facility. Rayleigh measurements in the heated jet facility are compared with hotwire and coldwire measurements where applicable.

5.2 Experiment calibration and data analysis method

5.2.1 Calibration

The technique was calibrated over a range of steady flow operating points in each flow system. The unheated nozzle flow in the acoustically modulated nozzle flow experiment was operated over a static temperature range of 289 – 298 K and velocity range of 10 – 140 m/s. The heated jet in the asymmetric oscillating counterflow experiment was operated over a static temperature range of 298 – 528 K with mean radial velocity component assumed as 0 m/s. The unheated jet was not operating (i.e., no air flow and no acoustic modulation) for the calibration portion of the second experiment. The heated jet in the third experiment was operated over a static temperature range of 298 – 765 K and

velocity range of 14 – 115 m/s. The photoelectron counts recorded by PMT 5 are linearly related to density, as shown by the heated jet density calibration data for 32 kHz sampling in figure 5.1. The photon count measurement from PMT 5 provides an independent yet simultaneous measurement of density along with the velocity and temperature measurements from spectroscopic analysis. The axial or radial velocity component and temperature were measured by analyzing the light from the circular and annular regions of the interference fringe pattern at the output of the FPI. The model of the fringe pattern (Eq. (2-19)), was used in the MLE analysis to estimate unknown parameters from the intensity data, such as velocity and temperature, or unknown optical system parameters, such as lens focal lengths, properties of the FPI, or detection efficiencies. The MLE method and the algorithm used in the data analysis software are discussed in detail in Appendix E. For calibration, mean temperature, velocity, density, and pressure measured by physical probes or calculated from the isentropic flow and ideal gas relations were used as known values in the model function. Several unknown parameters were evaluated by MLE analysis of the mean photon count data at the calibration points. These unknown parameters included system detection efficiencies, effective finesse of the FPI, and fringe forming lens focal length. Once determined, these parameters were input into the model function for use in MLE analysis of the PMT counts for temperature and velocity measurements. Figures 5.2 and 5.3 show the mean temperature and velocity measured by the Rayleigh technique using the mean PMT values compared with thermocouple measurements and velocity calculated using isentropic flow relations, respectively, at the calibration points sampled at 1, 16, and 32 kHz data rates in the heated jet experiment. The errors in the measured mean temperatures and velocities are plotted versus the

expected isentropic velocity in figure 5.4, where temperature is also varying over the range shown in figure 5.2. The mean temperatures measured by the Rayleigh technique are within ± 7 K of the expected values for a majority of the data points and the mean velocities are within ± 7 m/s of their expected values.

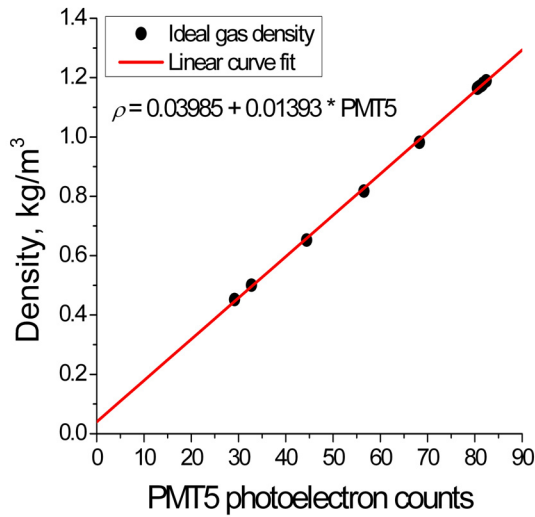


Figure 5.1. Density calculated from thermocouple and pressure probe data by ideal gas law plotted as a function of PMT 5 photoelectron counts at a 32 kHz sampling rate in the heated jet experiment. The equation of the linear curve fit shown is used to evaluate time-resolved density in the experiment.

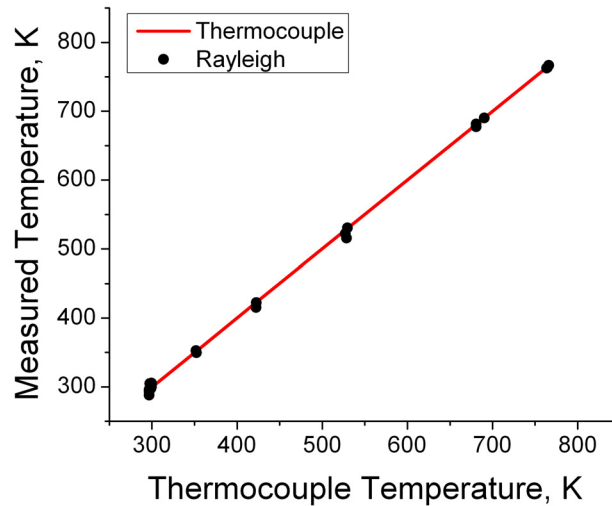


Figure 5.2. Temperature measured by the Rayleigh technique compared to thermocouple measured temperature at the calibration points for 1, 16, and 32 kHz data rates in the heated jet experiment.

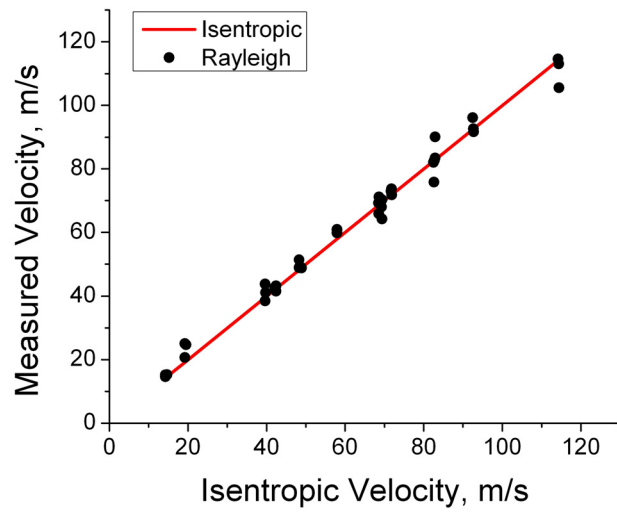


Figure 5.3. Velocity measured by the Rayleigh technique compared to velocity calculated by isentropic flow relations using pressure probe and thermocouple measurements at the calibration points for 1, 16, and 32 kHz data rates in the heated jet experiment.

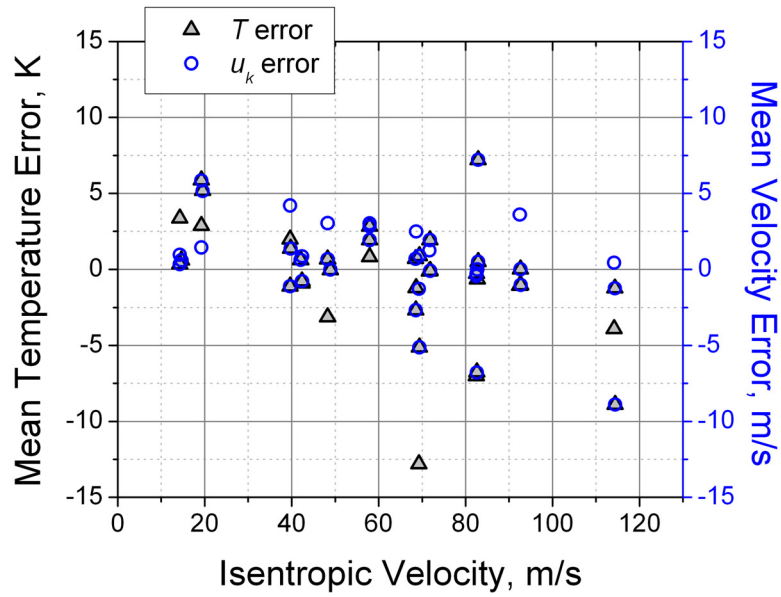


Figure 5.4. Mean temperature and velocity error for the calibration data presented in figures 5.2 and 5.3.

5.2.2 Data analysis and simulations

Using the linear relation between PMT 5 photon counts and density, and MLE analysis of the photon counts from PMTs 1-4, time histories of instantaneous density, temperature, and velocity were evaluated. Although a constant static pressure equivalent to the ambient pressure is probably a valid assumption in these free jet experiments, the pressure was assumed to be unknown. The density measured by PMT 5 and the temperature estimate from MLE analysis of PMT 1-4 photon counts were used to determine the local pressure using the ideal gas law to demonstrate that this measurement technique is applicable in flows where the pressure is unknown and the ideal gas law is valid. Details of the parameter estimation procedure are provided in Appendix E.

The numerical simulation described in Appendix D was used to generate simulated “noisy” data. A time record of oscillating temperature and velocity similar to the values expected in the validation studies (experiments 1 and 2) was provided as input for the simulation by assuming a sinusoidal flow response to a sinusoidal acoustic excitation. For each sample in the time record ideal (noise-free) data were computed in terms of expected photon counts from each of the five PMTs. Photon count values were generated with Poisson noise for each sample and recorded in a data file. The simulated data record was then read into another program that performed MLE analysis of the photon counts in the record to determine instantaneous velocity and temperature values. This analysis procedure is identical to the data analysis performed on experimental data (Appendix E). The simulated data are presented in this chapter along with the corresponding experimental data for comparison and validation of the numerical model.

5.2.3 Power spectral calculations

The mean velocity, temperature, and density were calculated and subtracted from their respective time history records to provide zero-mean records, which were used to calculate the power spectral densities of the property fluctuations. Because of the shot noise in the PMT signals, it was necessary to use relatively long data records and calculate power spectra using a technique known as the Welch method of modified periodograms (Welch, 1967). Due to extensive processing time of the Rayleigh data (approximately 1000 samples/minute), only the first 2.56 seconds of the data were analyzed in the validation studies (experiments 1 and 2) and the first 10.24 and 5.12 seconds were analyzed for the 16 kHz and 32 kHz data rates, respectively, in the third experiment. In the Welch method, a data record sampled at a rate $f_s = 16$ kHz (32 kHz) was subdivided into smaller records of length $L = 2048$ (4096) samples, which were overlapped by 50%. The modified periodograms of each sub-record were calculated using a data window. These individual periodograms were then averaged to obtain the estimate of the power spectrum. The number of individual periodograms used to calculate the averaged power spectrum depends on the length of the record used. The 2.56 second data records resulted in 38 overlapped segments, the 5.12 second data records resulted in 78 overlapped segments, and the 10.24 second data records resulted in 158 overlapped segments. The frequency resolution of the resulting spectra is $f_s / L = 7.8125$ Hz. The hotwire data was sampled at 16 or 32 kHz rates, but the coldwire data was sampled at only 1 kHz due to the response limit of the system. Sampling rates were chosen so that the power spectra for all rates resulted in the same frequency resolution, and the power levels in each frequency bin could be directly compared. Overlapping the segments by

50% provided a near maximum reduction in the variance in the spectral estimate. The resulting power spectra from the Rayleigh scattering measurements provide fluctuation information up to half of the sampling frequency (8 kHz or 16 kHz), and the sum of all points in the spectra is equivalent to the mean square fluctuations.

Two numerical processing methods exist that are commonly used to eliminate noise from power spectra. Shot noise is broadband noise that contributes equally over all frequencies; therefore it causes a constant offset or noise floor in the spectrum. If the spectrum flattens out at high frequencies due to the lack of significant fluctuations, then the average value of this noise floor can be estimated and subtracted from every point in the spectrum, eliminating the broadband shot noise contribution. This procedure was used to eliminate shot noise in the Rayleigh data in experiment 3. The second method, which is only possible if you have two simultaneous measurements of the same property, is to take the cross-spectrum of the two simultaneous, independent measurements (Oppenheim & Schaffer, 1975). Any uncorrelated noise will be eliminated from the final spectrum. One way to obtain the two simultaneous measurements is to split the light into two separate paths and individually analyze each beam path. This would require a secondary set of all spectral analysis and detection equipment, which is not very practical. Therefore, the noise floor subtraction method is the one used in this work.

5.3 Experiment 1: Acoustically modulated jet experiment: velocity fluctuation validation study

The unheated nozzle flow was operated at a mean velocity of 10 m/s while the flow velocity was perturbed by acoustically-induced pressure waves emanating from a loudspeaker which was driven by a sinusoidal voltage input with a frequency of 50 Hz. Other excitation frequencies and fluctuation amplitudes were investigated; however only this representative case is presented. Flow measurements were made using the Rayleigh technique and hotwire anemometry (CTA). The hotwire instrumentation was sampled at 16 kHz; however Rayleigh measurements were acquired at 16 and 32 kHz sampling rates. While all three flow parameters (ρ , T , u_k) were measured using the Rayleigh technique, only velocity results are presented here since the temperature and density fluctuations were expected to be very small; this assumption was verified by the Rayleigh measurements. The temperature and density measurements exhibited fluctuation levels similar to the lower bound predicted by the simulation analysis, which indicates that if any temperature and density fluctuations are present they are less than the measurement limit of this technique. Simulated velocity data was generated assuming a purely sinusoidal flow response at the fundamental frequency of 50 Hz.

A short segment of the time-history record of the simulated velocity measurements for a sampling rate of 16 kHz is shown in figure 5.5 and the corresponding power spectrum calculated from the full time-history record is shown in figure 5.6. The input (ideal) velocity function is shown for comparison. A monochromatic sinusoidal response at the fundamental frequency (f_{fund}) of 50 Hz was assumed with *mean* velocity of 12.6 m/s and amplitude (A) equal to 14.6 m/s using the following velocity signal input function:

$$signal = A \sin(2\pi f_{fund} t) + mean \quad (5-1)$$

The time-history records and power spectra of experimental velocity data (Rayleigh and hotwire measurements) acquired at 16 kHz sampling rate in a similar flow scenario as that of the simulation are presented in figures 5.7 and 5.8, respectively. Power spectral information is available up to half of the sampling frequency, however only the first 1000 Hz of the spectra are shown in figures 5.6 and 5.8 because the spectra are very flat beyond that point due to lack of significant fluctuations at high frequencies. Simulated data for the same flow conditions are shown for a sampling rate of 32 kHz in figures 5.9 and 5.10, and the corresponding Rayleigh and hotwire data are shown in figures 5.11 and 5.12. The experimental power spectra for both the Rayleigh and hotwire data indicate that fluctuations are present at the fundamental driving frequency as well as harmonics of that frequency. The source of these harmonic fluctuations was investigated by measuring the displacement of the speaker diaphragm during operation using an Ometron VPI sensor (model 8330) scanning laser doppler vibrometer. Figure 5.13 shows the power spectrum of speaker displacements determined by the vibrometer measurements, which verifies the presence of harmonic frequency components in the speaker output. The presence of these harmonic disturbances leads to the asymmetric nature of the periodic velocity fluctuations. Figures 5.14 and 5.15 show a time-history record and corresponding power spectra of simulated velocity data having an input function that is a summation of sinusoidal components at the fundamental and nine harmonic frequencies as given by the following equation, where $N = 10$ and $A(i)$ is the signal amplitude at the i^{th} multiple of the fundamental frequency (f_{fund}):

$$signal = \sum_{i=1}^N [A(i) \sin(2\pi(f_{fund} \cdot i)t)] + mean \quad (5-2)$$

The simulated flow response function has an asymmetric nature similar to that of the experimental data. This is a very simplistic model of flow response to a multiple-frequency sinusoidal disturbance. Many other factors have been ignored in the model, such as viscous effects; however the purpose of this exercise is not to model the flow phenomena, but rather to demonstrate that the Rayleigh experiment simulation can accurately model the light scattering and detection processes and provide insight into the measurement application.

The time-history plots of the experimental and simulated Rayleigh data show that random noise levels are comparable. This is further verified by the baseline noise levels calculated from the power spectra. In each figure showing power spectral data (figures 5.6, 5.8, 5.10, 5.12, and 5.15) a baseline noise level has been indicated, which was found by averaging the power levels over the last 1000 Hz of the spectrum where insignificant flow fluctuations exist and the spectrum has leveled out. Based on a frequency bin width of 7.8125 Hz, the baseline power level was used to calculate the lower bound of the velocity fluctuation level that can be measured via these second-order statistical calculations. Recall from the earlier uncertainty analysis in Chapter 3 that the lower bound on the instantaneous velocity measurements was on the order of 17 m/s for a data rate of 16 kHz and 25 m/s for 32 kHz data rate. The lower-bound uncertainty in velocity fluctuation amplitude calculated from second-order statistics here is on the order of 2 m/s, which is in agreement with the lower bound calculated in the simulation analysis of Chapter 3, which was presented in figure 3.21. Notice that the lower-bound values

determined from the simulated data are nearly equivalent to the values determined from the experimental data. The baseline noise level is mostly due to Poisson noise inherent in the photon detection process. Poisson noise is random and therefore contributes equally over all frequencies; hence the baseline noise level can be subtracted from all points in the power spectrum to provide a more accurate spectral estimation, as discussed in section 5.2.3. Figure 5.16 demonstrates the benefit of subtracting the noise floor from Rayleigh velocity power spectrum that was presented in figure 5.12; the baseline level is reduced such that the power spectrum indicates fluctuation levels similar to those measured by the hotwire probe. This is a unique feature of the power spectrum that allows uncorrelated shot noise contribution to be ‘filtered’ from second-order statistical quantities, such as mean square fluctuations.

An additional observation to note about the experimental power spectra is the good comparison between the spectra acquired from Rayleigh and hotwire measurements up until the point where the velocity fluctuation levels fall below the lower-bound of the Rayleigh measurement capability. Slight amplitude differences exist due to the noise pedestal of the Rayleigh power spectra, as well as minor dissimilarities in the flow at the time of the two non-simultaneous measurements. Keep in mind that the hotwire is a physical probe that intrusively provides the velocity measurement. The probe itself may be the cause of some of the dissimilarities mentioned. One major difference between the Rayleigh and hotwire measurements is a band of large velocity fluctuations in the 640 – 700 Hz frequency range that are observed in the Rayleigh power spectra but are not present in the hotwire spectra. These velocity fluctuations are not actually present in the

flow. The laser used in these experiments has a tendency to exhibit resonance in its output at various frequencies. These resonances are often amplified when external noise sources, like the loudspeaker output, are present. A peak in this same frequency range was observed in other velocity measurements acquired using this same laser, even in flows where no acoustic modulation was present. The velocity is determined by measuring the location of the Doppler shifted interference fringe associated with the Rayleigh scattered light relative to the location of the reference fringe associated with the incident laser light. The reference fringe location is not monitored during Rayleigh data acquisition; it is assumed fixed at the location set by the Fabry-Perot stabilization system. Any change in the reference fringe location due to modulation or drift of the laser frequency shows up as apparent velocity fluctuations or velocity bias error in the Rayleigh measurements.

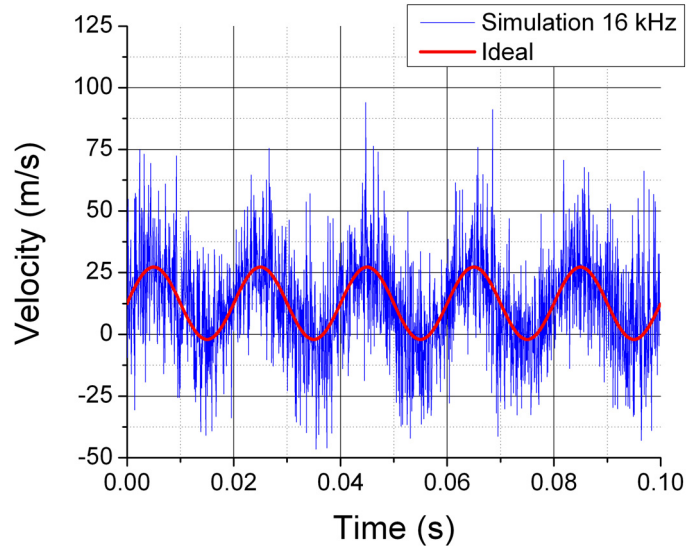


Figure 5.5. Simulated velocity data for 50 Hz sinusoidal velocity perturbation with $mean = 12.6$ m/s and $A = 14.6$ m/s, sampled at 16 kHz.

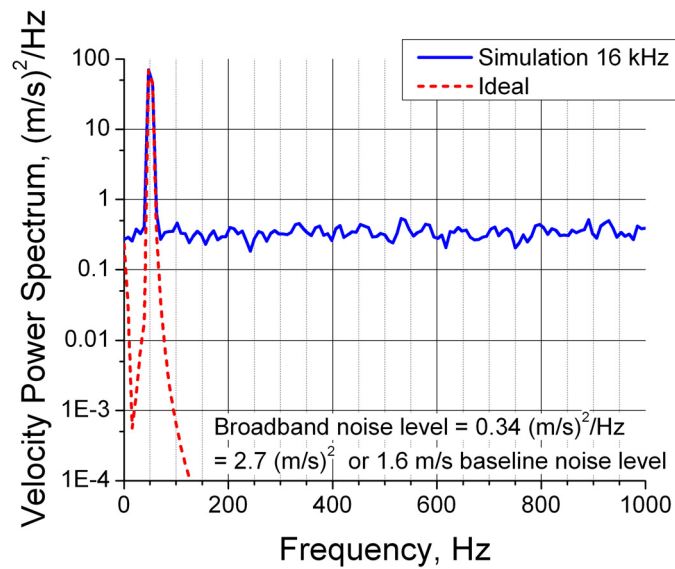


Figure 5.6. Power spectra of simulated velocity data from figure 5.5.

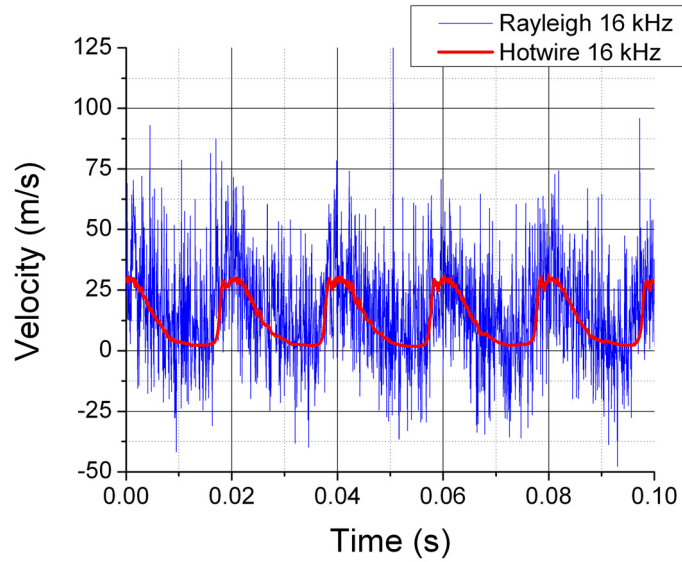


Figure 5.7. Experimental velocity data for a sinusoidal velocity perturbation with fundamental frequency of 50 Hz, sampled at 16 kHz.

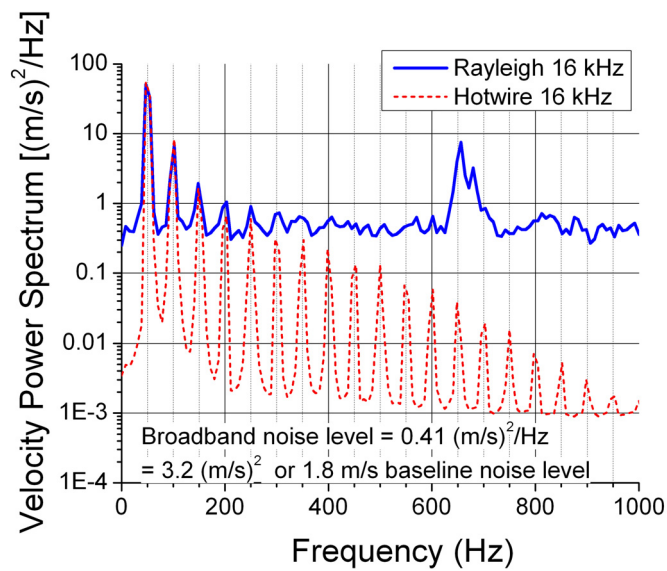


Figure 5.8. Power spectra of experimental velocity data from figure 5.7.

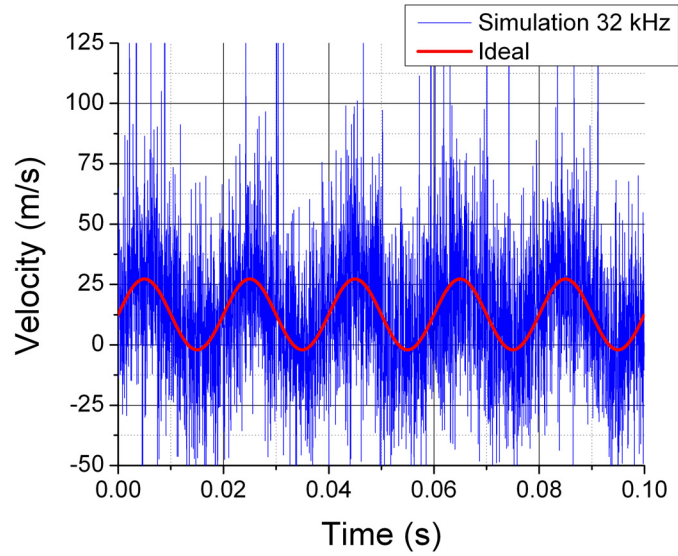


Figure 5.9. Simulated velocity data for 50 Hz sinusoidal velocity perturbation with $mean = 12.6$ m/s and $A = 14.6$ m/s, sampled at 32 kHz.

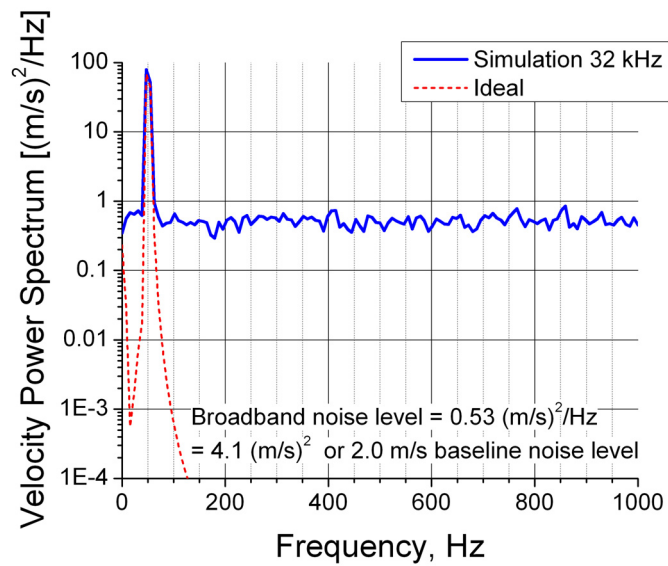


Figure 5.10. Power spectra of simulated velocity data from figure 5.9.

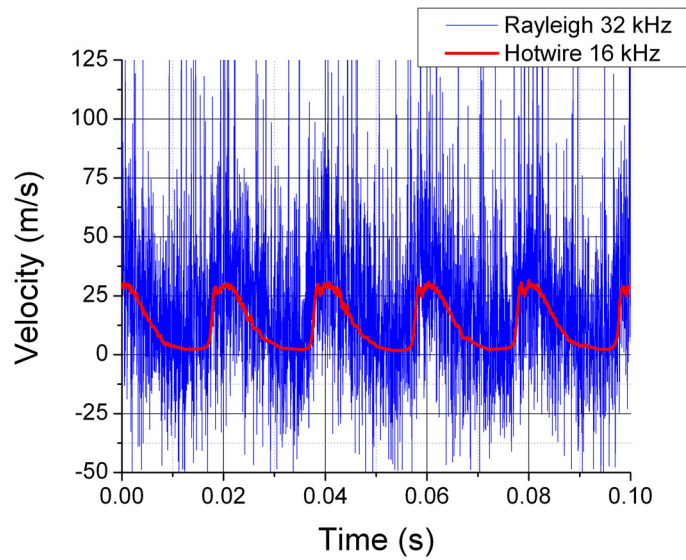


Figure 5.11. Experimental velocity data for a sinusoidal velocity perturbation with fundamental frequency of 50 Hz. Rayleigh data sampled at 32 kHz and hotwire data sampled at 16 kHz.

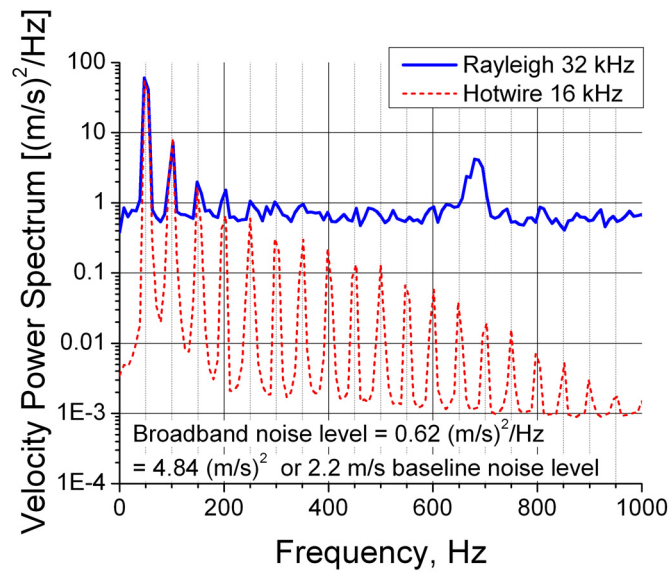


Figure 5.12. Power spectra of experimental velocity data from figure 5.11.

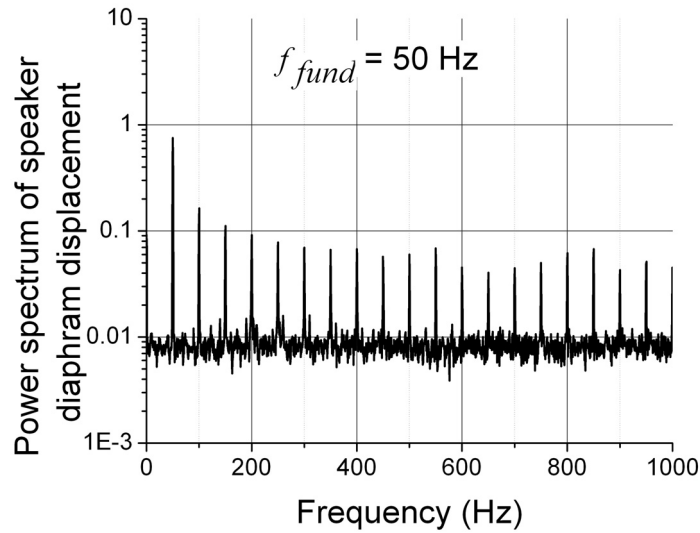


Figure 5.13. Power spectrum of speaker diaphragm displacement measured by a scanning laser doppler vibrometer showing harmonic components in the speaker output.

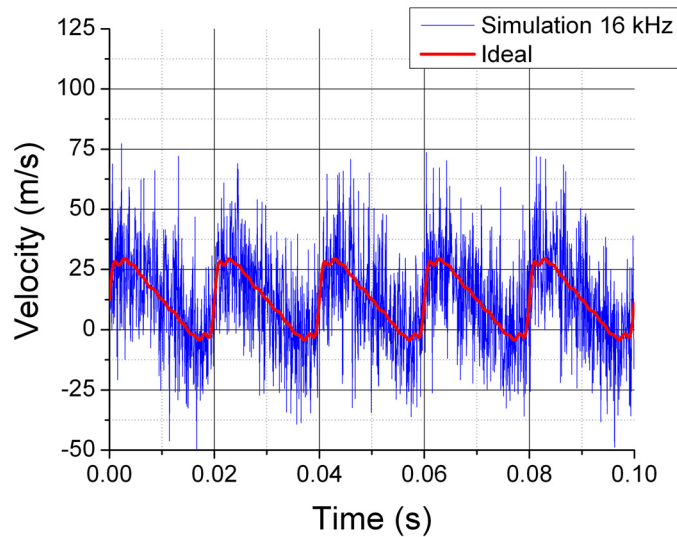


Figure 5.14. Simulated 16 kHz rate velocity data for 50 Hz fundamental sinusoidal velocity perturbation with $mean = 12.6 \text{ m/s}$ and $A(i) = 14.6, 5.7, 2.6, 1.6, 1.5, 1.1, 1.08, 0.94, 0.72, 0.7 \text{ m/s}$ for $i = 1$ to 10, where $A(1)$ is the amplitude at the fundamental frequency and $A(i)$ is the amplitude at the i^{th} harmonic frequency.

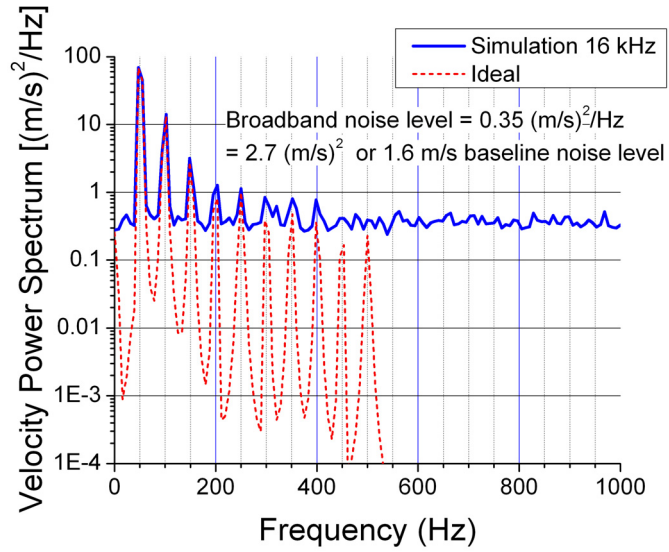


Figure 5.15. Power spectra of simulated velocity data from figure 5.14.

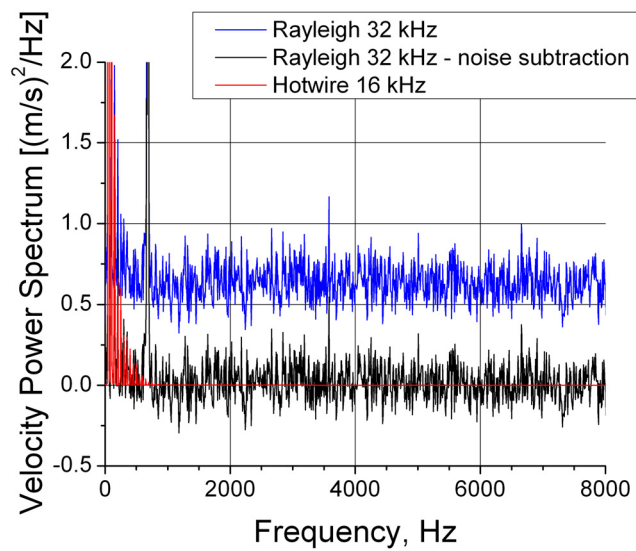


Figure 5.16. Experimental velocity power spectrum for Rayleigh and hotwire data illustrating the benefit of subtracting the noise floor from the Rayleigh power spectrum.

5.4 Experiment 2: Asymmetric oscillating counterflow with unequal enthalpies experiment: temperature and density fluctuation validation study

A counterflow with unequal enthalpies was perturbed by acoustically-induced pressure waves emanating from a loudspeaker in the unheated jet plumbing which was driven by a sinusoidal voltage input with a frequency of 100 Hz. Other excitation frequencies and fluctuation amplitudes were investigated; however only this representative case is presented. The unheated jet was operated at a temperature of 295 K and a velocity of 10 m/s. The heated jet was operated at a temperature of 425 K and velocity of approximately 12 m/s. Flow measurements were made using the Rayleigh technique and coldwire thermometry (CCA). The Rayleigh measurements were acquired at 16 and 32 kHz sampling rates, whereas the coldwire instrumentation was limited to a sampling rate of 1 kHz. Simulated temperature data was generated assuming a flow response consisting of a summation of sinusoidal functions at the fundamental frequency of 100 Hz and three additional harmonic frequencies using Eq. (5-2). The density in the simulations was calculated from the sinusoidal temperature input using the ideal gas law.

All three flow parameters (ρ , T , u_k) were measured using the Rayleigh technique, however the discussion will mainly focus on the temperature and density results since the velocity fluctuations were expected to be small at the chosen measurement location on the jet centerline near the stagnation point. Figure 5.17 shows a time segment of Rayleigh velocity results from this experiment compared with simulated data that assumes a non-fluctuating 0 m/s mean flow velocity, and figure 5.18 shows the corresponding power spectra for these data records. The Rayleigh velocity measurements exhibit fluctuation levels slightly greater than the fluctuations due to shot noise exhibited by the simulated

data in figure 5.17. The Rayleigh velocity power spectrum demonstrates higher fluctuation levels than the simulated velocity power spectrum at the acoustic fundamental driving frequency and the first two harmonic frequencies as shown in figure 5.18. The probe volume length in the radial direction was 1.1 mm making it possible that the Rayleigh measurements include off-centerline radial velocity fluctuations, especially if the probe volume is not perfectly centered in the axisymmetric flow. The off-centerline radial velocity fluctuations could be quite high near the stagnation plane where the flow is turned 90 degrees to its original axial orientation. The velocity fluctuations induced by acoustic modulation oscillate around a mean velocity of 0 m/s, demonstrating the ability of the Rayleigh technique to measure flow reversal. Although the velocity fluctuations are not completely negligible in this experiment, their presence should not affect the validation of temperature and density fluctuation measurements.

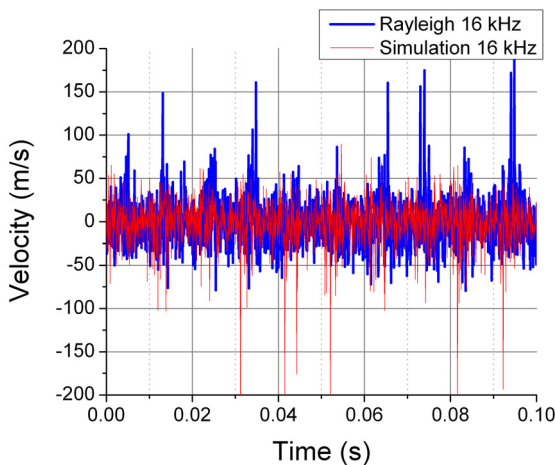


Figure 5.17. Rayleigh velocity data acquired in the asymmetric oscillating counterflow experiment with 100 Hz acoustic modulation compared to simulated non-fluctuating velocity data.

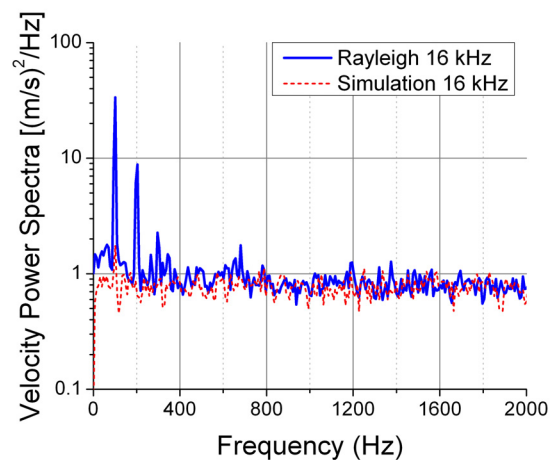


Figure 5.18. Power spectra of the Rayleigh and simulated velocity data shown in figure 5.17.

5.4.1 Temperature fluctuation validation

A short segment of the time-history record of the simulated temperature measurements for a sampling rate of 16 kHz is shown in figure 5.19 and the corresponding power spectrum calculated from the full time-history record is shown in figure 5.20. The input (ideal) temperature function is shown for comparison. The input temperature signal is a sum of sinusoidal functions as given by Eq. (5-2) with the mean and amplitude values as stated in the caption of figure 5.19. The time-history records and power spectra of experimental temperature data (Rayleigh and coldwire measurements) acquired at 16 kHz sampling rate in a similar flow scenario as that of the simulation are presented in figures 5.21 and 5.22, respectively. A simulated temperature record for the same flow conditions is shown for a sampling rate of 32 kHz in figure 5.23 and the power spectrum calculated from this data is shown in figure 5.24. The corresponding experimental data at 32 kHz sampling rate are shown in figures 5.25 and 5.26. Again, only the first 1000 Hz of the much longer power spectra are shown, and the experimental power spectra for both the Rayleigh and coldwire data indicate the presence of harmonic frequency components due to harmonic distortion in the loudspeaker output.

The time-history plots of simulated and experimental temperature data show comparable levels of random noise, as shown in figure 5.19 compared to figure 5.21 and figure 5.23 compared to figure 5.25. The noise levels at the maximum flow temperature are greater than the noise levels at the minimum temperature as a result of a lower molecular number density at the higher temperature. The baseline random noise levels calculated from the power spectra (indicated in figures 5.20, 5.22, 5.24, and 5.26) are nearly equal for the

simulated and experimental cases. Recall from the earlier uncertainty analysis that the lower bound on instantaneous temperature measurements was predicted to be on the order of 40 K for the lower temperature limit (298 K) at a sampling rate of 16 kHz and up to 100 K for the upper temperature limit (423 K) and a sampling rate of 32 kHz. The lower-bound uncertainty in the temperature fluctuation amplitude calculated from second-order statistics presented in this section is on the order of 7 – 9 K. The temperature fluctuation amplitude lower bound was determined to be in the range of 5 – 12 K for temperatures ranging from 298 to 423 K based on the numerical simulation analysis presented in figure 3.20 for a 32 kHz data rate.

The experimental power spectra exhibit some significant amplitude differences between the Rayleigh and coldwire measurements at the harmonic frequencies; although the amplitudes at the fundamental frequency compare pretty well. Even with subtraction of the random noise pedestal, the amplitude levels at the harmonic frequencies are still an order of magnitude different. One possible explanation is that the physical coldwire probe has a significant influence on the fluctuating flow field that causes an amplitude reduction in the temperature fluctuations. The position of the coldwire probe in the flow was observed to have an effect on the location of the maximum temperature gradient via the shadowgraph instrumentation. This observation leads to the belief that the coldwire probe may not provide an accurate measurement of the oscillating temperature field. The limited frequency response of the coldwire probe may also be a contributing factor. This situation reiterates the need for a non-intrusive measurement technique.

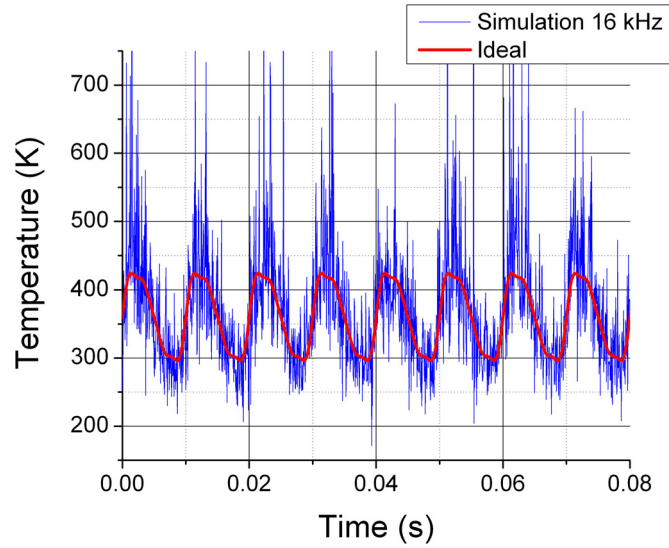


Figure 5.19. Simulated 16 kHz rate temperature data for 100 Hz fundamental sinusoidal temperature perturbation with $mean = 360$ K and $A(i) = 65.9, 10.6, 8.4, 4.4$ K for $i = 1$ to 4, where $A(1)$ is the amplitude at the fundamental frequency and $A(i)$ is the amplitude at the i^{th} harmonic frequency.

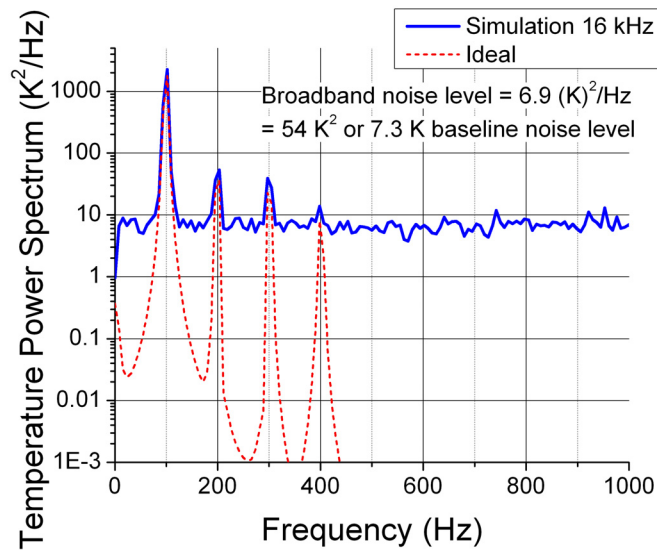


Figure 5.20. Power spectra of simulated temperature data from figure 5.19.

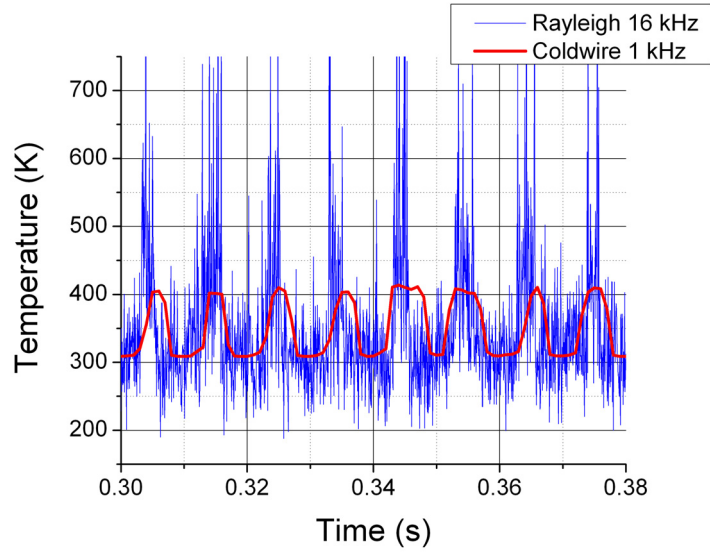


Figure 5.21. Experimental temperature data for a sinusoidal temperature perturbation with fundamental frequency of 100 Hz. Rayleigh data is sampled at 16 kHz and coldwire data is sampled at 1 kHz.

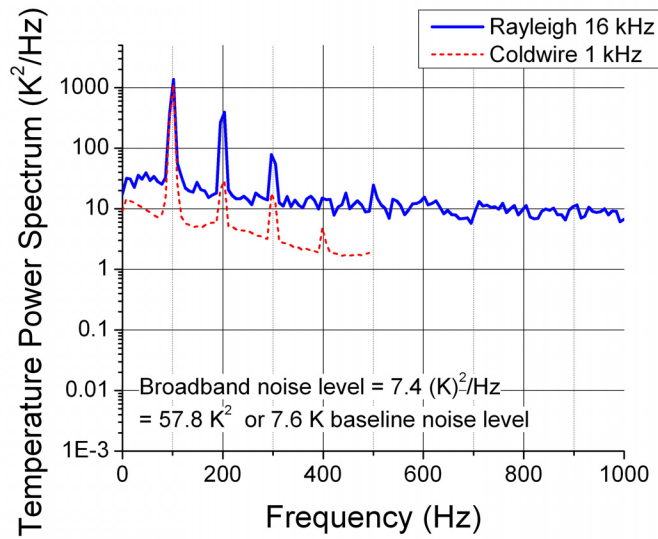


Figure 5.22. Power spectra of experimental temperature data from figure 5.21.

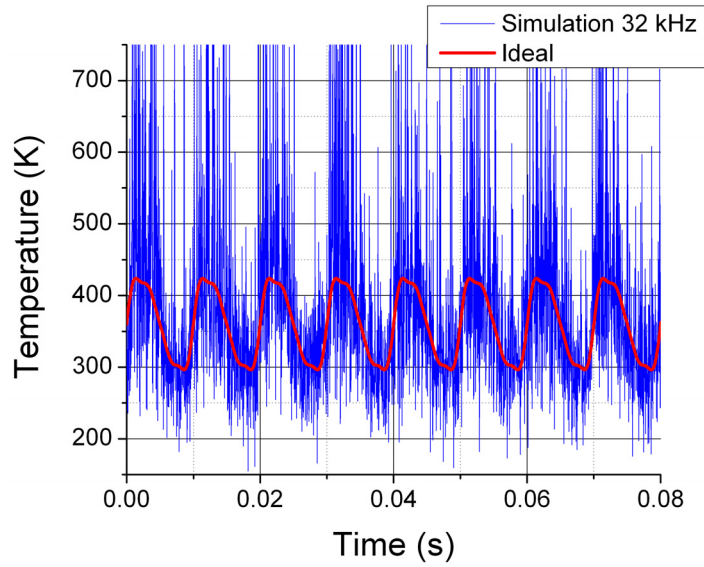


Figure 5.23. Simulated 32 kHz rate temperature data for 100 Hz fundamental sinusoidal temperature perturbation with *mean* and *A(i)* values same as in figure 5.19.

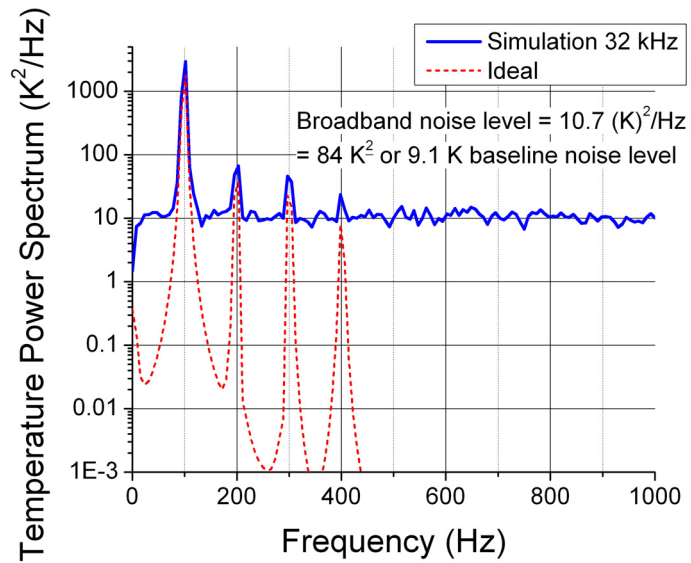


Figure 5.24. Power spectra of simulated temperature data from figure 5.23.

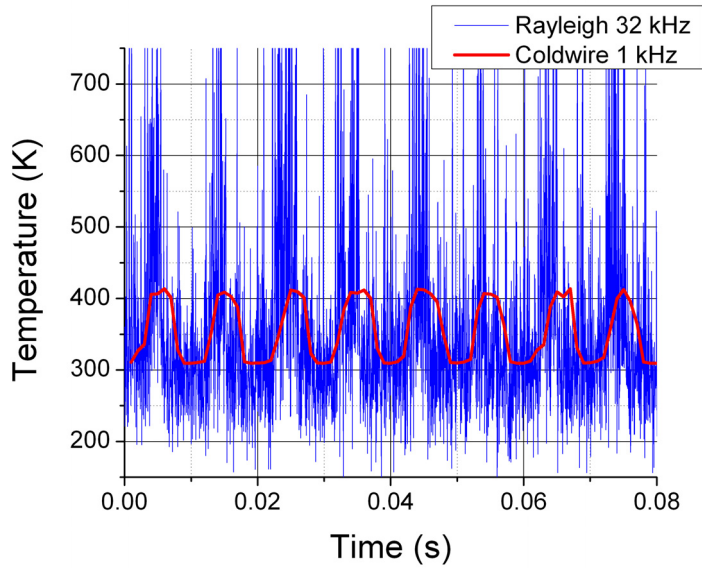


Figure 5.25. Experimental temperature data for a sinusoidal temperature perturbation with fundamental frequency of 100 Hz. Rayleigh data is sampled at 32 kHz and coldwire data is sampled at 1 kHz.

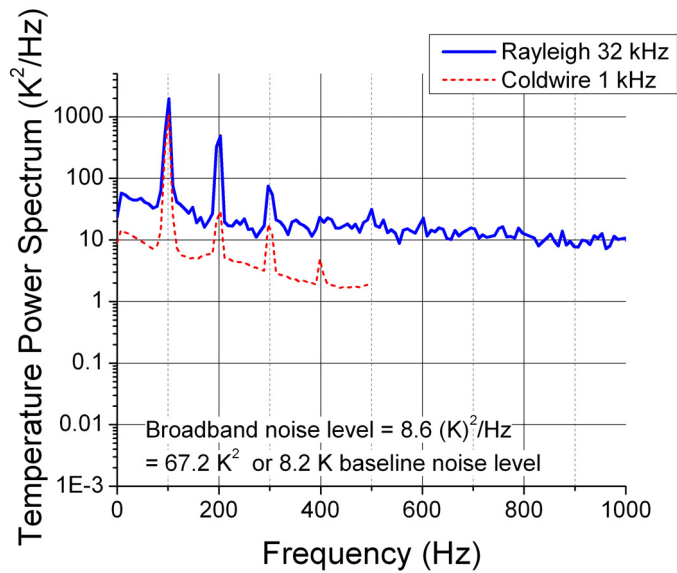


Figure 5.26. Power spectra of experimental temperature data from figure 5.25.

5.4.2 Density fluctuation validation

A short segment of the time-history record of the simulated density measurements for a sampling rate of 16 kHz is shown in figure 5.27, and the corresponding power spectrum calculated from the full time-history record is shown in figure 5.28. The input (ideal) density function is shown for comparison. The density signal was calculated from the input temperature function using the ideal gas law. The input temperature signal was based on Eq. (5-2) with mean temperature and amplitude values as stated in the caption of figure 5.19. The time-history record of experimental Rayleigh density data acquired at 16 kHz sampling rate in a similar flow scenario as that of the simulation is compared to density values calculated from coldwire temperature measurements acquired at 1 kHz sampling rate in figure 5.29. The corresponding power spectra are shown in figure 5.30. Simulated data for the same flow conditions are shown for a sampling rate of 32 kHz in figures 5.31 and 5.32, and the corresponding experimental flow data are shown in figures 5.33 and 5.34. Again, only the first 1000 Hz of the much longer power spectra are shown, and the experimental power spectra for both the Rayleigh and coldwire data indicate the presence of harmonic frequency components due to harmonic distortion in the loudspeaker output. As observed in the experimental temperature data in the previous section, the density power spectra also exhibit some significant amplitude differences between the Rayleigh measurements and those calculated from the coldwire measurements at the harmonic frequencies, possibly due to influences of the physical probe on the flow field or the limited frequency response of the coldwire probe.

The time-history plots of simulated and experimental density data show comparable levels of random noise, as shown in figure 5.27 compared to figure 5.29 and figure 5.31 compared to figure 5.33. The earlier uncertainty analysis presented in Chapter 3 showed that the lower bound on instantaneous density measurements was predicted to be on the order of $0.06 - 0.8 \text{ kg/m}^3$ for the density range studied in this experiment and a sampling rate of 32 kHz. The lower-bound uncertainty in the density fluctuation amplitude calculated from second-order statistics presented in this section is approximately 0.007 kg/m^3 , as indicated in figures 5.28, 5.30, 5.32, and 5.34, which is in agreement with that predicted by the simulation analysis presented in figure 3.15.

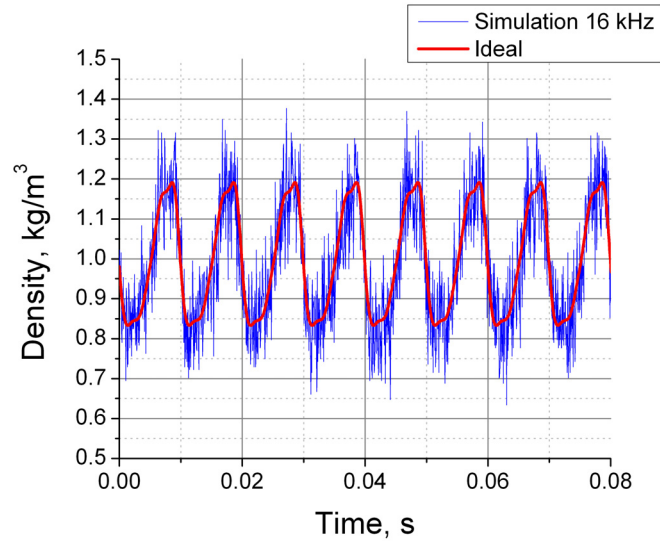


Figure 5.27. Simulated 16 kHz rate density data based on the 100 Hz fundamental sinusoidal temperature perturbation presented in figure 5.19. Density was calculated from the temperature input using ideal gas law and assuming atmospheric pressure.

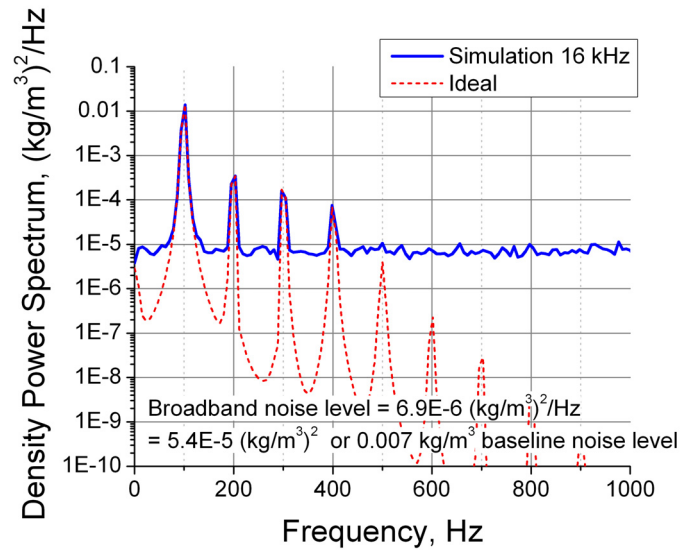


Figure 5.28. Power spectra of simulated density data from figure 5.27.

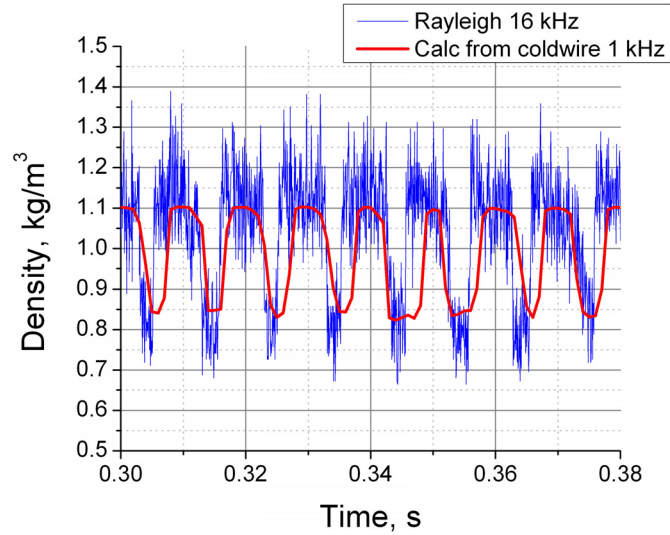


Figure 5.29. Experimental density data measured directly by the Rayleigh technique and calculated from coldwire temperature measurements using ideal gas law for a sinusoidal density perturbation with fundamental frequency of 100 Hz. Rayleigh data is sampled at 16 kHz and coldwire data is sampled at 1 kHz.

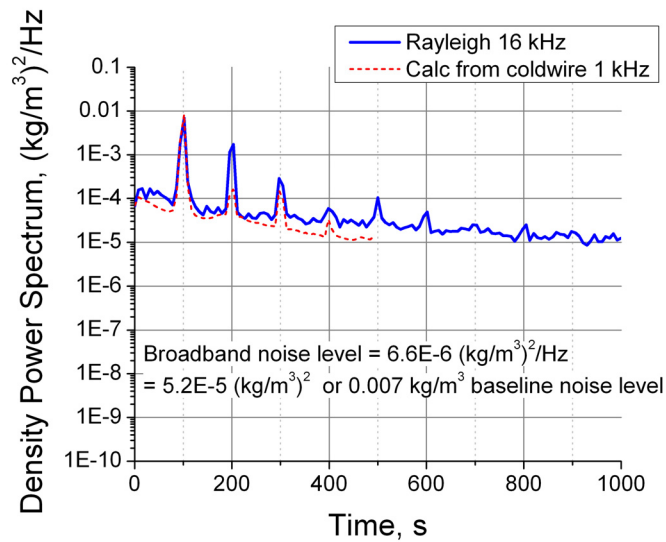


Figure 5.30. Power spectra of experimental density data from figure 5.29.

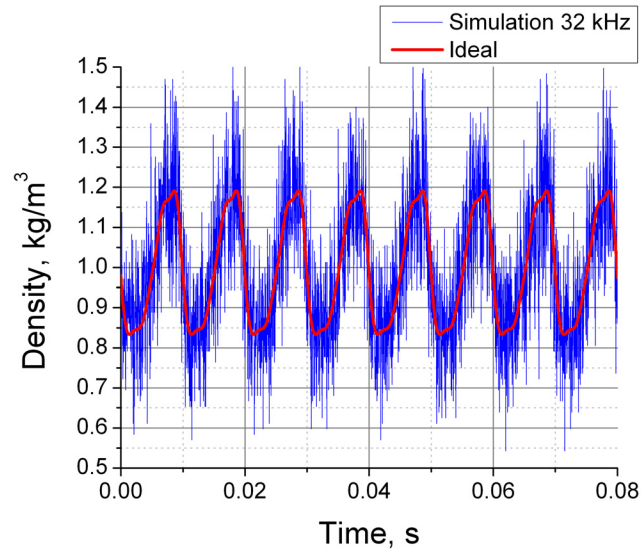


Figure 5.31. Simulated 32 kHz rate density data based on the 100 Hz fundamental sinusoidal temperature perturbation presented in figure 5.23. Density was calculated from the temperature input using ideal gas law and assuming atmospheric pressure.

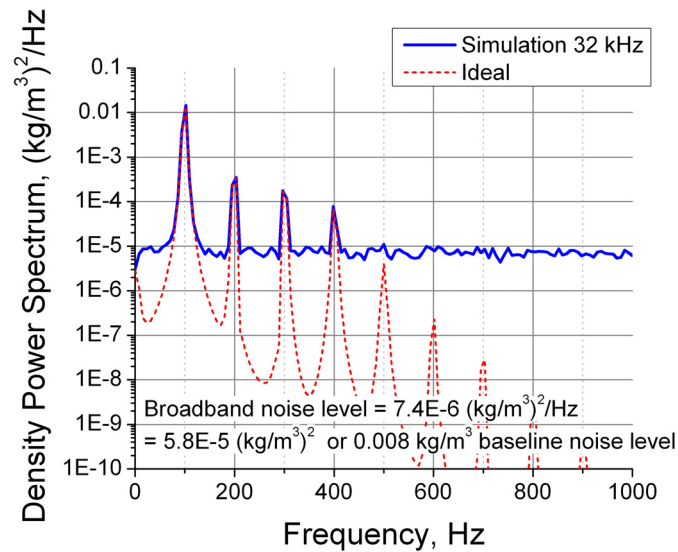


Figure 5.32. Power spectra of simulated density data from figure 5.31.

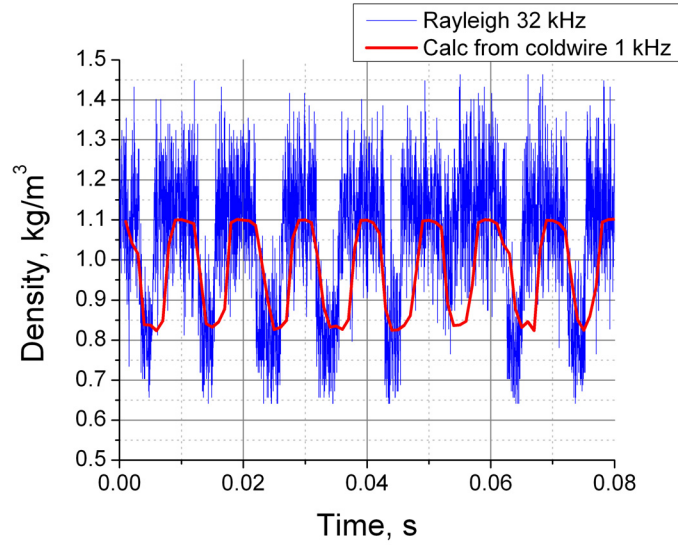


Figure 5.33. Experimental density data measured directly by the Rayleigh technique and calculated from coldwire temperature measurements using ideal gas law for a sinusoidal density perturbation with fundamental frequency of 100 Hz. Rayleigh data is sampled at 32 kHz and coldwire data is sampled at 1 kHz.

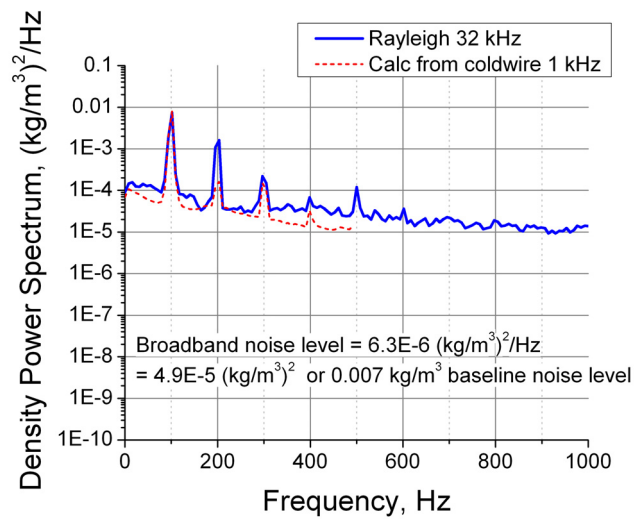


Figure 5.34. Power spectra of experimental density data from figure 5.33.

5.5 Experiment 3: High speed electrically-heated jet: simultaneous measurement demonstration

The electrically-heated high speed jet was operated at conditions which provided moderate temperature and velocity levels where resistance probes were applicable for measurement comparisons, as well as conditions achieving the maximum jet operating temperature and velocity. The Rayleigh probe volume and the hotwire and coldwire probes were scanned horizontally across the centerline of the electrically-heated jet at an axial station of 2 jet diameters (20 mm). Scans of the Rayleigh probe volume were performed at centerline jet conditions of 420 K and 38 m/s (case 1), 420 K and 110 m/s (case 2), and 775 K and 45 m/s (case 3). Due to the limitations discussed in Chapter 4, the coldwire probe could only be used to provide temperature fluctuations in the low velocity, low temperature flow (case 1). The hotwire probe also had severe physical limitations leading to the inability to make hotwire measurements in heated flows. Therefore, hotwire measurements were performed in room temperature flows with maximum velocities similar to the heated flow cases (~ 40 m/s and ~ 110 m/s). In cases where coldwire measurements could not be performed, the Rayleigh density measurements were used to provide a secondary temperature measurement. Temperatures were calculated from the density measurement by applying the ideal gas law and assuming the static pressure is equal to the ambient pressure, which should be a valid assumption in these subsonic nozzle flows exiting into ambient conditions. The radial scans provided measurements in the jet core as well as in the turbulent mixing layer formed between hot and cold air streams.

5.5.1 Measurements in low velocity, low temperature flow (case 1)

Figures 5.35 - 5.40 show density, temperature, and velocity power spectra plots for measurements acquired in a flow with maximum temperature of 420 K and maximum velocity of 38 m/s at a location in the shear layer (radial position = 7 mm). This measurement location was chosen for demonstration of power spectral calculations since the highest amplitude fluctuations occur in the shear layer. The power spectra were calculated from 1, 16, and 32 kHz Rayleigh data, 1 kHz coldwire temperature data, and 32 kHz hotwire velocity data acquired in an unheated, room temperature flow with maximum velocity of 38 m/s. The broadband noise floor was estimated from the last 1000 Hz of the 16 and 32 kHz Rayleigh power spectra and has been subtracted from those spectra. Since the 1 kHz data does not flatten out within the frequency range of that measurement, the noise floor was estimated using the numerical simulation and subtracted from the 1 kHz Rayleigh power spectrum. Figure 5.35 shows the density power spectra calculated from Rayleigh measurements and time-resolved density calculated from coldwire temperature measurements using the ideal gas law. Figure 5.37 shows the temperature power spectra calculated from Rayleigh and coldwire temperature data. Figure 5.39 shows the velocity power spectra calculated from Rayleigh and hotwire velocity data. Figures 5.36, 5.38, and 5.40 show the same power spectra as their respective preceding figure with different axis limits showing details of the low frequency content of the signal. Figures 5.36 and 5.38 demonstrate good agreement between the Rayleigh measurements and the coldwire measurements in the frequency range from 0 to 500 Hz. The Rayleigh velocity power spectra in figure 5.40 exhibit numerous peaks in the spectra that are believed to be erroneous peaks resulting from laser

frequency fluctuations. The laser has been known to exhibit resonant frequencies which cannot be controlled or eliminated in this laser system. The general shape of each Rayleigh velocity power spectrum, disregarding the large erroneous spectral peaks, is similar to that of the hotwire data. The hotwire measurements were acquired in an unheated flow and may not accurately reflect the velocity fluctuations in the heated flow case. The error induced by the laser frequency oscillations is non-negligible and ways to eliminate this error by use of a frequency-stabilized laser system will be investigated in future work.

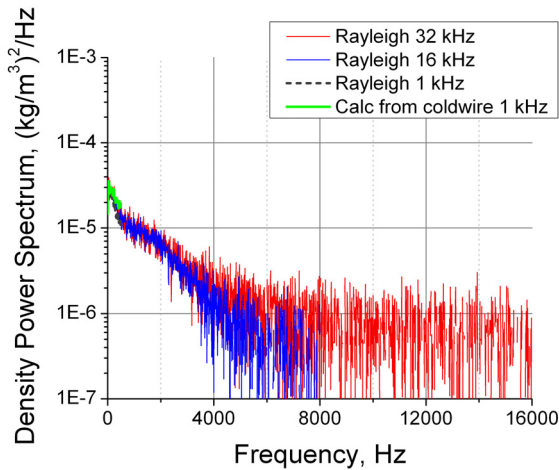


Figure 5.35. Density power spectra calculated from Rayleigh and coldwire data acquired in the shear layer of a flow with maximum temperature and velocity of 420 K and 38 m/s.

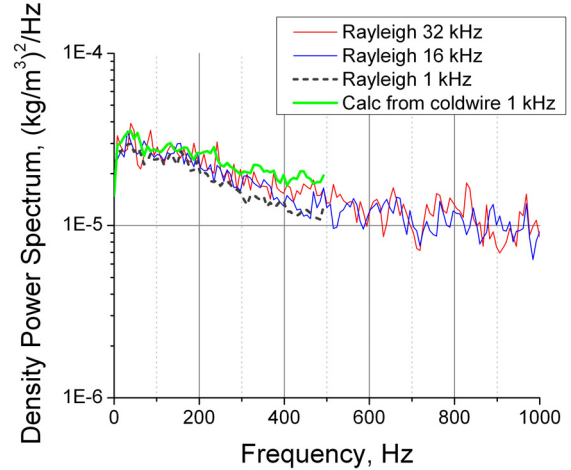


Figure 5.36. Low frequency region of the density power spectra shown in figure 5.35.

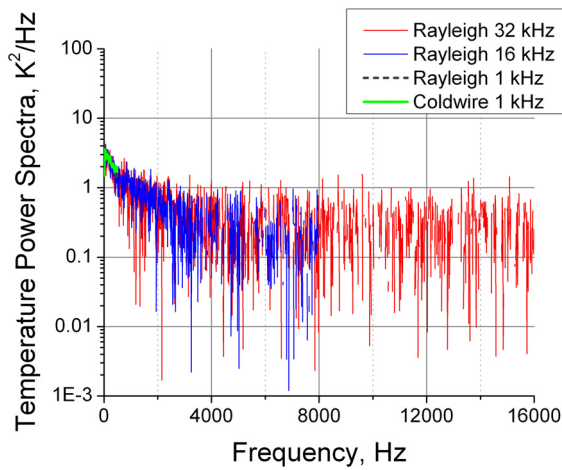


Figure 5.37. Temperature power spectra calculated from Rayleigh and coldwire data acquired in the shear layer of a flow with maximum temperature and velocity of 420 K and 38 m/s.

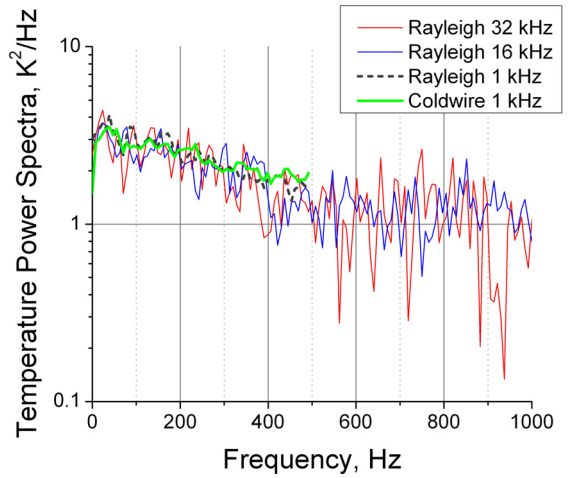


Figure 5.38. Low frequency region of the temperature power spectra shown in figure 5.37.

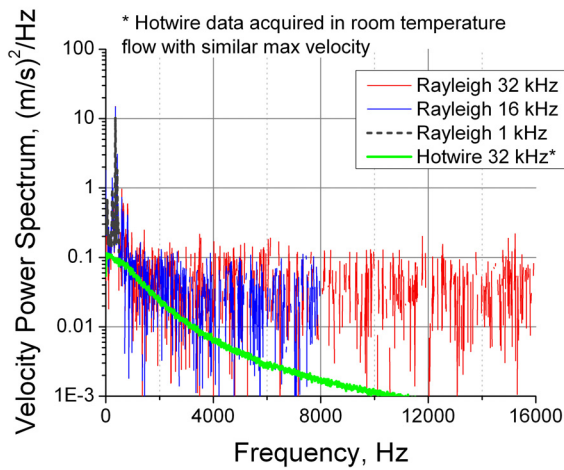


Figure 5.39. Velocity power spectra calculated from Rayleigh data acquired in the shear layer of a flow with maximum temperature and velocity of 420 K and 38 m/s and hotwire data acquired in a room temperature flow with maximum velocity of 38 m/s.

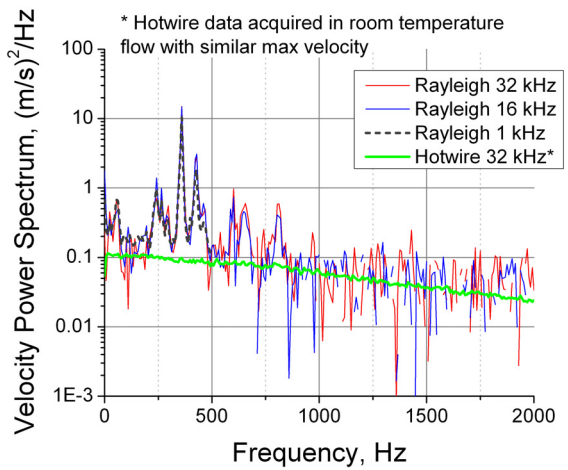


Figure 5.40. Low frequency region of the velocity power spectra shown in figure 5.39.

The mean density, temperature, and velocity values were calculated from the time-history data, and the turbulence density, temperature, and velocity fluctuations were calculated from the power spectra by taking the square root of the sum of all points in the spectra after the noise floor had been subtracted. Figures 5.41 and 5.42 show radial profiles across the jet flow of the mean density and turbulence density fluctuations, respectively, calculated from the 1, 16, and 32 kHz Rayleigh measurements compared with densities calculated from thermocouple and 1 kHz coldwire temperature measurements using ideal gas law. The mean density values compare well between the various data sets; the greatest deviation being approximately 2%. The coldwire measurements provide very accurate turbulence levels for fluctuations up to 500 Hz; however, as the 16 and 32 kHz power spectra show (figures 5.35 and 5.37), significant density and temperature fluctuations still exist beyond 500 Hz. Since the 1 kHz coldwire and Rayleigh measurements represent a low-pass filtered version of the fluctuations, the resulting turbulence levels from these data sets are lower than the true density fluctuations over all frequencies. Based on the rule of thumb that the peak shear layer fluctuations are approximately 15-20% of the difference between the centerline and ambient densities, the peak fluctuations are expected to be on the order of $0.05\text{-}0.07\text{ kg/m}^3$, which is in agreement with the 16 and 32 kHz Rayleigh measurements in figure 5.42, which show peak fluctuations of $0.06\text{ to }0.073\text{ kg/m}^3$. Comparison of the 1 kHz Rayleigh measurements with the coldwire results demonstrates accuracies of approximately 0.006 kg/m^3 .

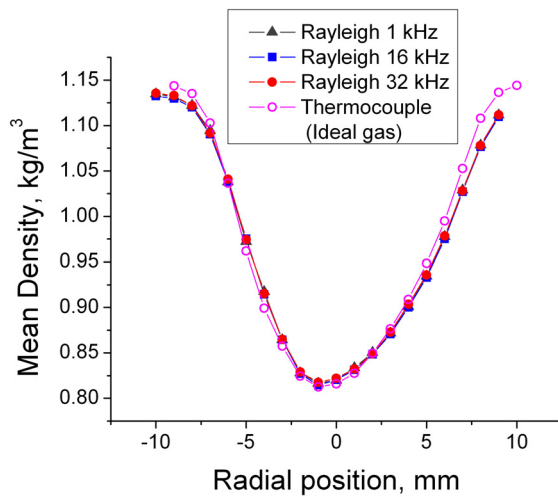


Figure 5.41. Mean density profile calculated from time-resolved Rayleigh data and measured by a thermocouple for a flow with maximum temperature and velocity of 420 K and 38 m/s.

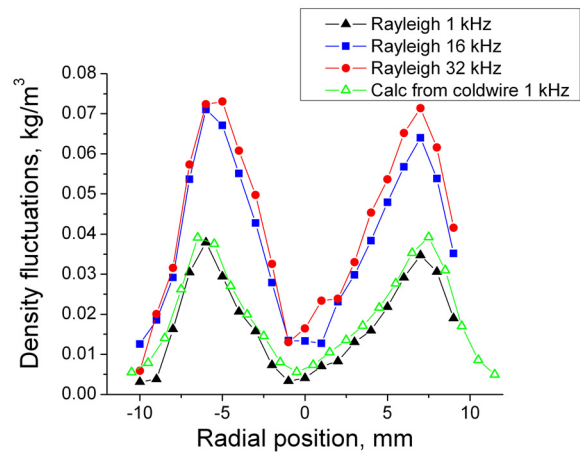


Figure 5.42. Density fluctuation profile calculated from Rayleigh and coldwire measurements in a flow with maximum temperature and velocity of 420 K and 38 m/s.

Figures 5.43 and 5.44 show radial profiles across the jet flow of the mean temperature and turbulence temperature fluctuations, respectively, calculated from the 1, 16, and 32 kHz Rayleigh measurements compared with thermocouple and 1 kHz coldwire temperature measurements. The mean temperatures from the Rayleigh measurements compare well with the thermocouple measurements which were acquired in the flow just prior to the Rayleigh data acquisition, with the greatest deviation being less than 2%. Deviation between the Rayleigh and coldwire mean temperatures is slightly greater; however the coldwire measurements were acquired on a different day and the jet conditions may not have been exactly duplicated. The 1 kHz Rayleigh temperature fluctuations match the 1 kHz coldwire measurements very well. The largest deviation between the two measurements is approximately 2 K and occurs in the jet core. The coldwire measurements provide very accurate turbulence levels for fluctuations up to 500

Hz; however, as the 16 and 32 kHz power spectra show (figure 5.37), significant temperature fluctuations still exist beyond 500 Hz. Since the 1 kHz coldwire and Rayleigh measurements do not account for higher frequency fluctuations, the resulting turbulence levels from these data sets are lower than the true temperature fluctuations over all frequencies. As an additional comparison or validation of the temperature fluctuations, the time-resolved density measurements were used to calculate time-resolved temperature by applying the ideal gas law to each sample in the time record, assuming the local pressure was equal to the ambient pressure. The temperature fluctuation levels were calculated from the power spectrum of the time-resolved density-calculated temperature record after the noise floor was subtracted. The fluctuation levels from this analysis are shown by the solid blue and red lines in figure 5.44, agreeing well with the corresponding direct temperature measurements by the Rayleigh technique shown by blue and red circles in the same figure for data rates of 16 and 32 kHz. The peak temperature fluctuations calculated from the direct Rayleigh temperature measurements range from 20 K to 24 K, agreeing with the rule of thumb for shear layer fluctuation levels, which are expected to be on the order of 18 – 24 K. Greater error is expected in the lower amplitude fluctuation measurements due to the non-zero temperature fluctuation amplitude measurement lower bound, which was determined to be 6 – 12 K for a 32 kHz data rate by the numerical simulation analysis in Chapter 3.

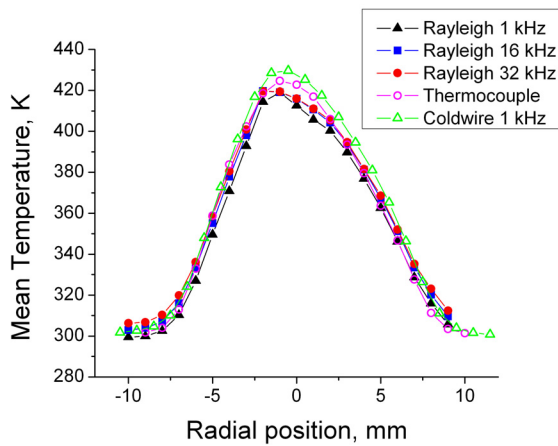


Figure 5.43. Mean temperature profile calculated from time-resolved Rayleigh and coldwire data and measured by a thermocouple for a flow with maximum temperature and velocity of 420 K and 38 m/s.

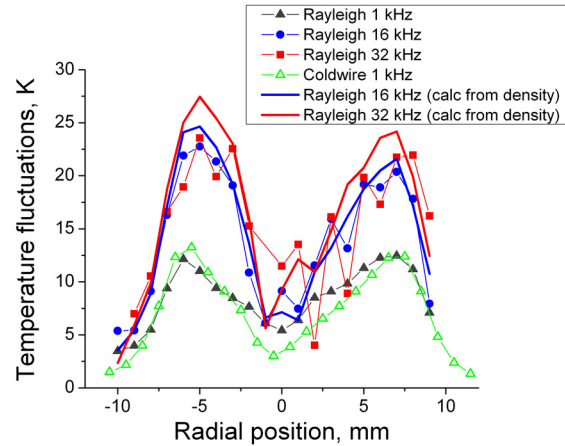


Figure 5.44. Temperature fluctuation profile calculated from Rayleigh and coldwire measurements in a flow with maximum temperature and velocity of 420 K and 38 m/s.

Figures 5.45 and 5.46 show radial profiles of mean velocity and turbulence velocity fluctuations, respectively, calculated from 1, 16, and 32 kHz Rayleigh measurements compared with pitot tube mean velocity measurements acquired in the same heated flow and 32 kHz hotwire velocity measurements acquired in an unheated flow at the same maximum velocity as the heated flow of case 1. The mean velocities from the Rayleigh measurements show some deviation from the pitot tube and hotwire measurements at some points in the radial profile. The Rayleigh velocity measurements in the low velocity region of the co-flow tend to be biased towards lower values than those measured by the pitot and hotwire probes by as much as 5 – 10 m/s. Agreement between the measurements gets better as velocity increases; however there are a few points that exhibit similar bias errors in the core region of the flow where the velocity and temperature are the greatest. As temperature increases, the Rayleigh spectral peak broadens and it becomes increasingly more difficult to accurately determine the spectral

peak location, which may be partly responsible for the errors observed in the mean velocity measurements. It has already been noted that the laser used for these measurements is not frequency stabilized; there is inherent drift in the laser frequency over time. Appendix F provides detailed analysis quantifying the amount of velocity error induced by frequency drift of this particular laser system. The expected laser frequency drift over the time period of the Rayleigh data acquisition leads to potential velocity bias error on the order of 4 m/s. Error due to the accuracy with which the reference fringe radius is set by the Fabry-Perot stabilization system results in additional bias error of up to 2 m/s, as quantified in Appendix F. The hotwire measurements provide shear layer fluctuation levels that are in line with the 15-20% rule of thumb that predicts fluctuations of 4.5 – 6 m/s; however the Rayleigh measurements indicate fluctuation levels 3-4 m/s greater than the hotwire data at the peaks and as much as 7 m/s greater in other regions of the profile. The hotwire measurements were acquired in an unheated flow and may not accurately reflect the velocity fluctuations in the heated flow case. The velocity turbulence intensity in a heated flow is expected to be less than the turbulence intensity in an unheated flow of the same velocity because the heated flow has a lower Reynolds number. Therefore, the fact that the hotwire measurements were not acquired in a heated flow does not account for the discrepancy. Several reasons for the high velocity fluctuation amplitude estimates by the Rayleigh technique have been identified. The Rayleigh velocity power spectra exhibit apparent velocity fluctuations that are related to laser frequency oscillations rather than actual flow velocity fluctuations, which will lead to a slight bias error in the velocity fluctuation estimates. The bias error associated with the erroneous spikes in the velocity power spectrum was estimated by calculating the rms

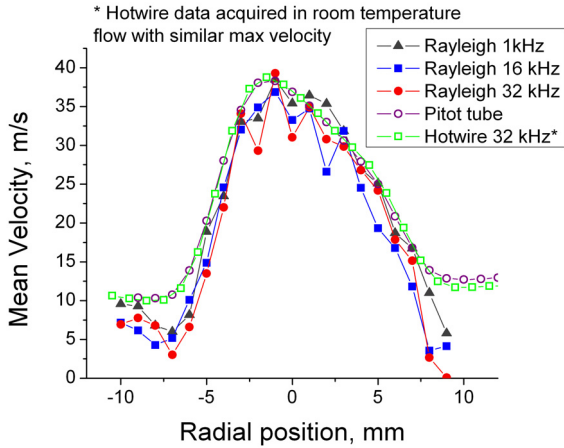


Figure 5.45. Mean velocity profile calculated from time-resolved Rayleigh and data and measured by a pitot tube in a flow with maximum temperature and velocity of 420 K and 38 m/s and hotwire measurements in a room temperature flow with maximum velocity of 38 m/s.

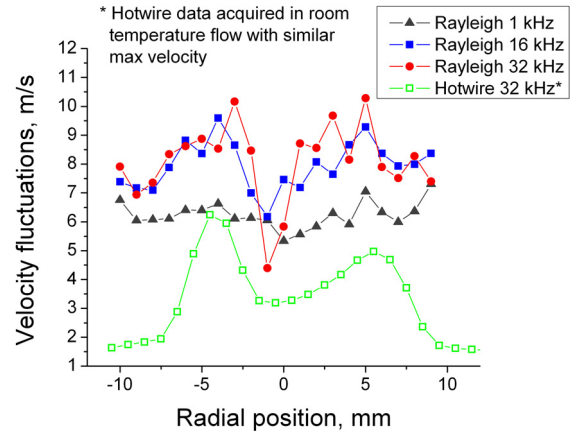


Figure 5.46. Velocity fluctuation profile calculated from Rayleigh measurements in a flow with maximum temperature and velocity of 420 K and 38 m/s and hotwire measurements in a room temperature flow with maximum velocity of 38 m/s.

fluctuations with these spikes included, and then again with the three highest amplitude peaks being replaced by power spectral levels equal to the average of the surrounding values. The rms velocity fluctuations calculated by the corrected power spectrum were approximately 2 m/s less than the rms fluctuations calculated from the original power spectrum containing the erroneous peaks. Also, the velocity fluctuation amplitude lower bound is on the order of 5 m/s based on numerical simulation analysis presented in figure 3.21, which means that velocity fluctuations that are less than this bound cannot be accurately measured.

5.5.2 Measurements in high velocity, low temperature flow (case 2)

Figures 5.47 - 5.49 show density, temperature, and velocity power spectra plots, respectively, for a measurement location in the shear layer (radial position = 7 mm)

calculated from 16 and 32 kHz Rayleigh data acquired in a flow with maximum temperature and velocity of 420 K and 110 m/s, and 32 kHz hotwire velocity data acquired in an unheated flow with maximum velocity of 110 m/s. The broadband noise floor has been subtracted from the Rayleigh power spectra. The coldwire probe was too delicate to withstand the high velocity of this flow; hence a secondary temperature fluctuation measurement by another technique is not available for this case. Instead, a second temperature measurement was calculated from the Rayleigh density measurement using ideal gas law, assuming the local pressure is equal to the ambient pressure. The density measurement is acquired independently from the temperature measurement in the Rayleigh technique and therefore provides a second independent temperature estimate to compare with the primary temperature results. The power spectra calculated from both temperature measurement methods are compared in figure 5.46 and show the same general trend, although the density-calculated temperature spectrum has a smaller amount of variance in the spectral estimate. The velocity power spectra for the Rayleigh measurements exhibits erroneous velocity fluctuation peaks in the spectra as observed previously. If these peaks are disregarded, the Rayleigh and hotwire velocity spectra have the same general shape, although the level of the 16 kHz Rayleigh spectrum is slightly lower at higher frequencies. The baseline noise level that was subtracted from the Rayleigh spectra may have been overestimated; it is possible that velocity fluctuations in the 7-8 kHz frequency range where the average noise floor was estimated were not completely negligible.

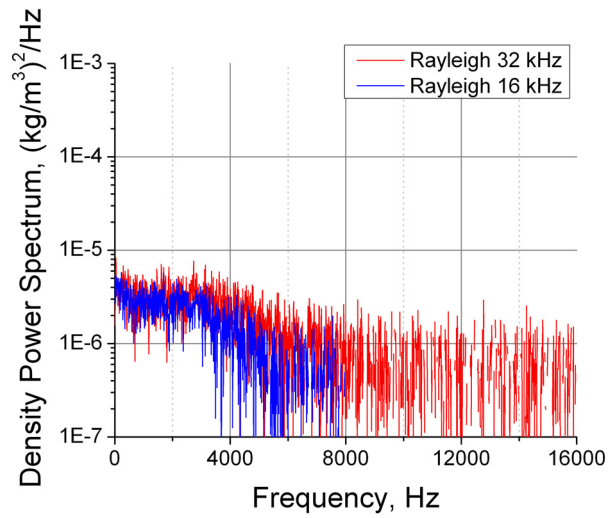


Figure 5.47. Density power spectrum calculated from Rayleigh data acquired in the shear layer of a flow with maximum temperature and velocity of 420 K and 110 m/s.

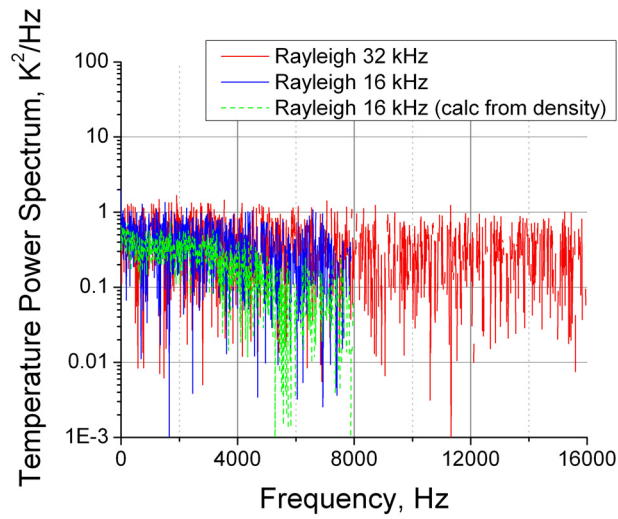


Figure 5.48. Temperature power spectra calculated from Rayleigh temperature and density data acquired in the shear layer of a flow with maximum temperature and velocity of 420 K and 110 m/s.

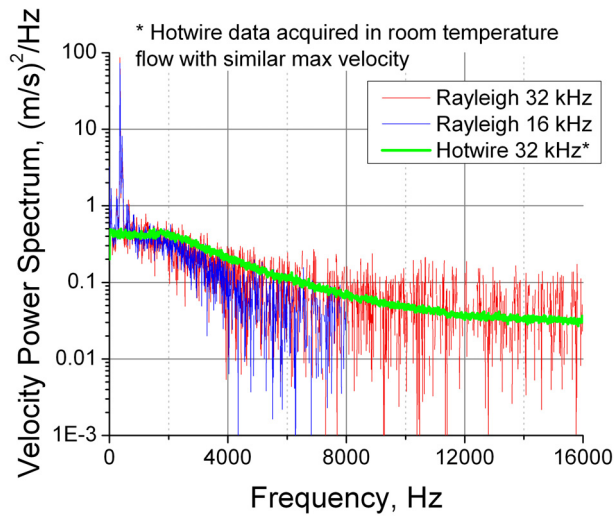


Figure 5.49. Velocity power spectra calculated from Rayleigh data acquired in the shear layer of a flow with maximum temperature and velocity of 420 K and 110 m/s and hotwire data acquired in a room temperature flow with maximum velocity of 110 m/s.

Figure 5.50 presents the mean density values calculated from the 16 and 32 kHz Rayleigh measurements across the jet flow at an axial station of 20 mm downstream of the nozzle exit compared to density values calculated from thermocouple measurements using ideal gas law. The corresponding turbulence density fluctuations are presented in figure 5.51. The Rayleigh mean density values deviate slightly from the thermocouple-calculated densities, with the greatest deviation being approximately 2.5%. Based on the rule of thumb that the peak shear layer fluctuations are approximately 15-20% of the difference between the centerline and ambient densities, the peak fluctuations are expected to be on the order of $0.05 - 0.07 \text{ kg/m}^3$, which is in agreement with the 16 and 32 kHz Rayleigh measurements in figure 5.51, which show peak fluctuation levels of $0.045 - 0.067 \text{ kg/m}^3$.

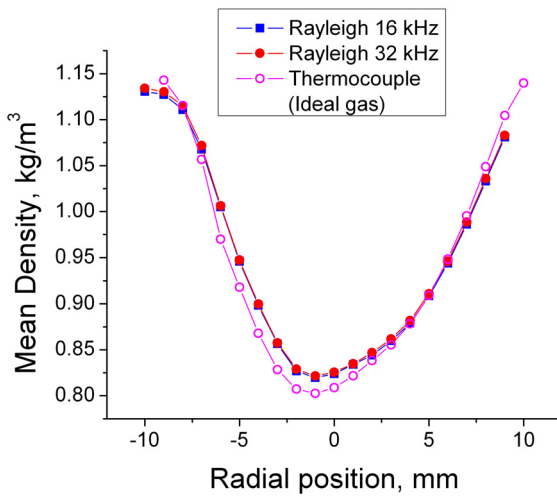


Figure 5.50. Mean density profile calculated from time-resolved Rayleigh data and measured by a thermocouple for a flow with maximum temperature and velocity of 420 K and 110 m/s.

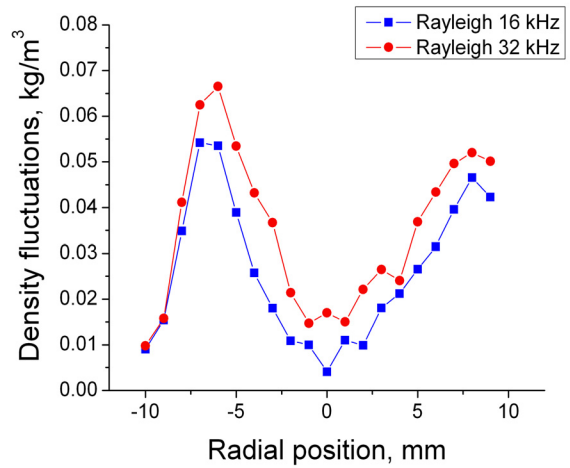


Figure 5.51. Density fluctuation profile calculated from Rayleigh measurements in a flow with maximum temperature and velocity of 420 K and 110 m/s.

Figure 5.52 shows the radial profile across the jet flow of the mean temperatures calculated from the 16 and 32 kHz Rayleigh measurements compared with thermocouple temperature measurements. The mean temperatures from the Rayleigh measurements deviate slightly from the thermocouple measurements by as much as 2%. Figure 5.53 shows the radial profile of temperature fluctuations across the jet flow calculated from the power spectra of the Rayleigh temperature measurements. Since the coldwire probe could not be used in these harsh flow conditions, temperature fluctuation measurements were calculated from the Rayleigh density measurements for comparison. The density-calculated temperature fluctuations were estimated from the power spectrum of the time-resolved density-calculated temperature record with the noise floor subtracted and are shown by the red and blue solid lines in figure 5.53. In general, the direct temperature fluctuation measurements agree well with the density-calculated temperature fluctuations,

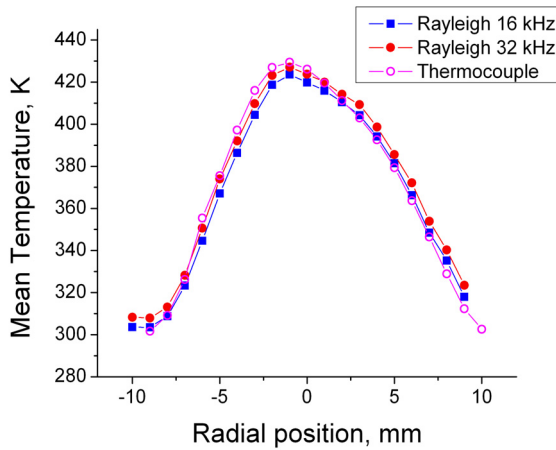


Figure 5.52. Mean temperature profile calculated from time-resolved Rayleigh data and measured by a thermocouple for a flow with maximum temperature and velocity of 420 K and 110 m/s.

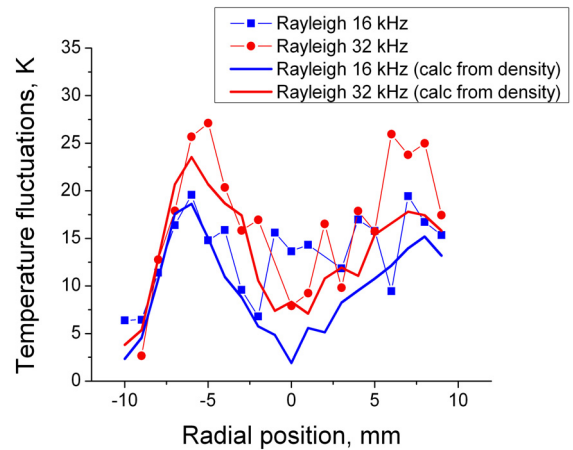


Figure 5.53. Temperature fluctuation profile calculated from Rayleigh measurements in a flow with maximum temperature and velocity of 420 K and 110 m/s.

although the temperature fluctuation levels calculated from the 16 kHz direct temperature measurement are slightly high in the jet core. Following the rule of thumb for shear layer fluctuation levels, the peak fluctuations are expected to be on the order of 18 – 24 K, which is in agreement with the levels measured in the shear layer by the 16 kHz Rayleigh measurements. The 32 kHz Rayleigh temperature fluctuation measurements are approximately 4 K high in the shear layer.

Figures 5.54 and 5.55 show radial profiles of mean velocity and turbulence velocity fluctuations, respectively, calculated from 16 and 32 kHz Rayleigh measurements compared with 32 kHz hotwire velocity measurements acquired in an unheated flow at the same maximum velocity as the heated flow of case 2. The mean velocities from the Rayleigh measurements show some deviation from the hotwire measurements at some points in the radial profile. The Rayleigh velocity measurements in the low velocity

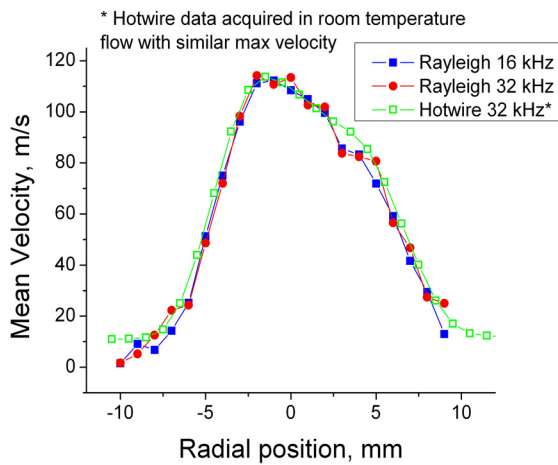


Figure 5.54. Mean velocity profile calculated from time-resolved Rayleigh and data in a flow with maximum temperature and velocity of 420 K and 110 m/s and hotwire measurements in a room temperature flow with similar maximum velocity.

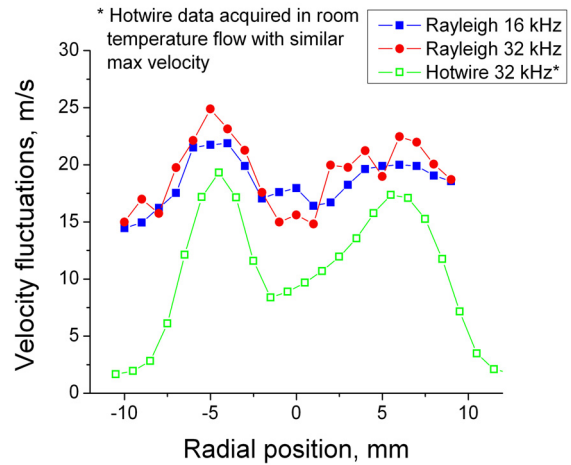


Figure 5.55. Velocity fluctuation profile calculated from Rayleigh measurements in a flow with maximum temperature and velocity of 420 K and 110 m/s and hotwire measurements in a room temperature flow with similar maximum velocity.

region of the co-flow tend to be biased towards lower values than those measured by the hotwire probe by as much as 5 – 10 m/s. This tendency is similar to that observed in the velocity measurements of case 1. The agreement between the measurements gets better as velocity increases; the Rayleigh measurements agree with the hotwire measurements within 5 m/s throughout most of the profile. The hotwire measurements provide shear layer fluctuation levels that are in line with the 15-20% rule of thumb, which gives expected shear layer fluctuations of 15 – 20 m/s; however the Rayleigh measurements indicate fluctuation levels 2 – 4 m/s greater than the hotwire data at the peaks and as much as 14 m/s greater in other regions of the profile. The reasons discussed previously, such as erroneous velocity fluctuations due to instability of the Rayleigh laser frequency and a non-zero fluctuation amplitude measurement lower bound, are also potentially responsible for the discrepancies observed in figure 5.55.

5.5.3 Measurements in low velocity, high temperature flow (case 3)

Figures 5.56 - 5.58 show density, temperature, and velocity power spectra plots, respectively, for a measurement location in the shear layer (radial position = 7 mm) calculated from 16 kHz Rayleigh data acquired in a flow with maximum temperature and velocity of 775 K and 45 m/s, and 32 kHz hotwire velocity data acquired in an unheated flow with similar maximum velocity. Recall from the simulation analysis in Chapter 3 that 32 kHz Rayleigh data at a temperature of 773 K experienced severe instabilities in the MLE analysis due to very low signal levels; hence experimental Rayleigh data was only acquired at the lower sampling rate of 16 kHz. The broadband noise floor has been subtracted from the Rayleigh power spectra. The maximum operating temperature for the coldwire probe was 423 K rendering it useless in this high temperature flow; hence the secondary temperature fluctuation measurement is provided by the Rayleigh density measurement using ideal gas law for comparison with the primary temperature measurements. The power spectra calculated from both temperature measurement methods are compared in figure 5.57 and show the same general trend, although the density-calculated temperature spectrum has a smaller amount of variance. The velocity power spectra for the Rayleigh measurements exhibits erroneous velocity fluctuation peaks in the spectra as observed previously. If these peaks are disregarded, the Rayleigh and hotwire velocity spectra have the same general shape, although the level of the Rayleigh spectrum is slightly higher at all frequencies. The higher fluctuation level measured by the Rayleigh technique is unexpected since the hotwire measurements were acquired in an unheated flow and fluctuations in a heated flow are expected to be slightly less due to a reduction in Reynolds number. The magnitude of the hotwire power

spectrum is at or below the baseline noise level of the Rayleigh power spectrum (~ 0.1 $(\text{m/s})^2/\text{Hz}$) over the entire frequency range; therefore the low amplitude velocity fluctuations present in this flow cannot be accurately measured by the Rayleigh technique under these experiment conditions.

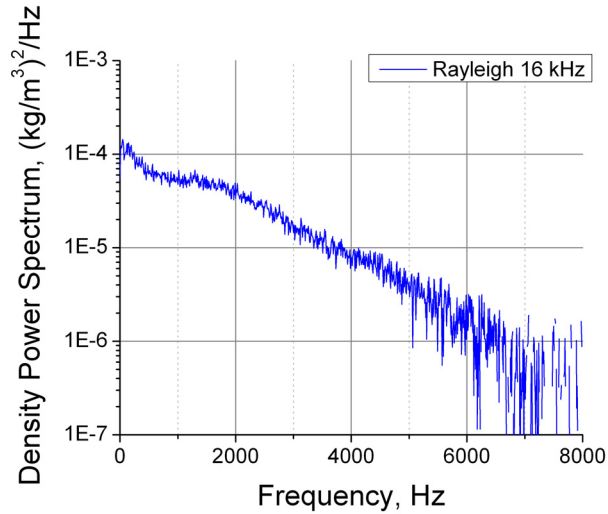


Figure 5.56. Density power spectrum calculated from Rayleigh data acquired in the shear layer of a flow with maximum temperature and velocity of 775 K and 45 m/s.

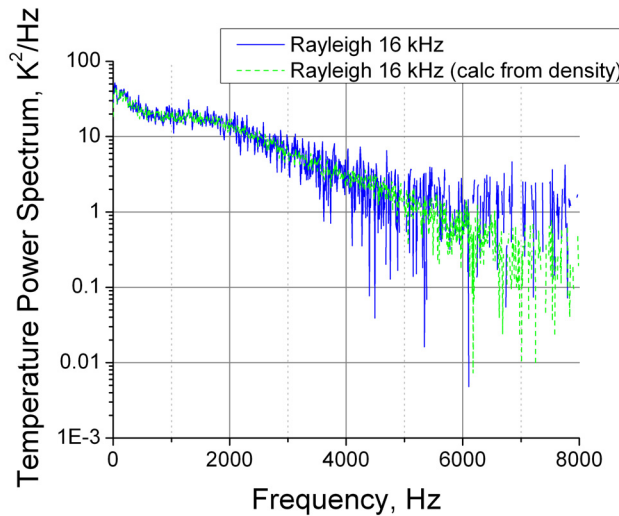


Figure 5.57 Temperature power spectra calculated from Rayleigh temperature and density data acquired in the shear layer of a flow with maximum temperature and velocity of 775 K and 45 m/s.

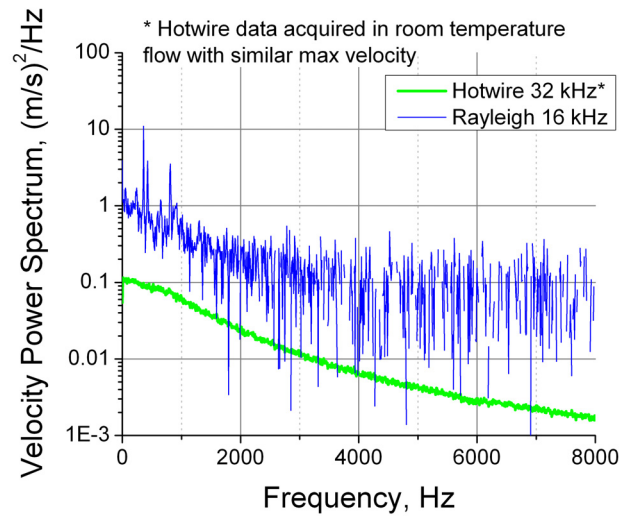


Figure 5.58. Velocity power spectra calculated from Rayleigh data acquired in the shear layer of a flow with maximum temperature and velocity of 775 K and 45 m/s and hotwire data acquired in a room temperature flow with similar maximum velocity.

Figure 5.59 shows the mean density values calculated from the 16 kHz Rayleigh measurements across the jet flow at an axial station of 20 mm downstream of the nozzle exit compared to density values calculated from thermocouple measurements using ideal gas law. The corresponding turbulence density fluctuations are presented in figure 5.60. The Rayleigh mean density values deviate by as much as 2.5% from the thermocouple-calculated densities. Based on the rule for shear layer fluctuations, the peak fluctuations are expected to be on the order of 0.11 - 0.14 kg/m³. The peak fluctuations measured by the Rayleigh technique in figure 5.60 indicate slightly higher fluctuation levels than expected by about 0.02 kg/m³.

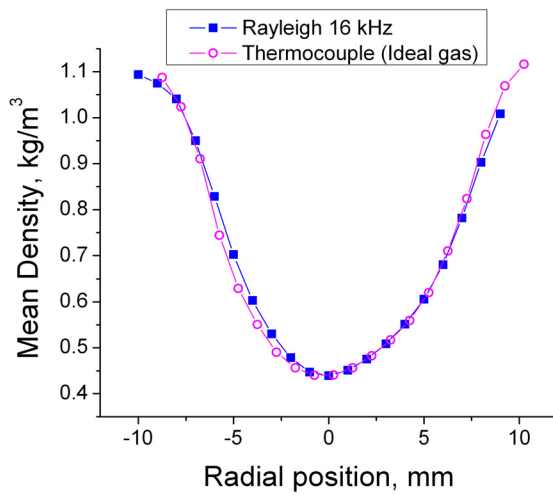


Figure 5.59. Mean density profile calculated from time-resolved Rayleigh data and measured by a thermocouple for a flow with maximum temperature and velocity of 775 K and 45 m/s.

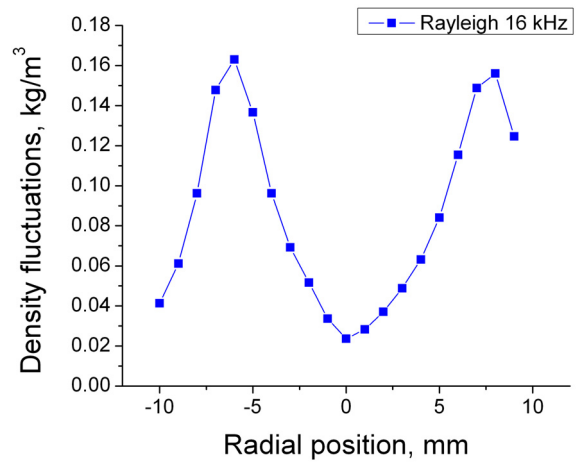


Figure 5.60. Density fluctuation profile calculated from Rayleigh measurements in a flow with maximum temperature and velocity of 775 K and 45 m/s.

Figure 5.61 shows the radial profile across the jet flow of the mean temperatures calculated from the 16 kHz Rayleigh measurements compared with thermocouple temperature measurements. The mean temperatures from the Rayleigh measurements agree well with the thermocouple measurements. Maximum deviation of the mean temperatures is approximately 2%. Figure 5.62 shows the radial profile of temperature fluctuations across the jet flow calculated from the power spectra of the 16 kHz Rayleigh temperature measurements. The Rayleigh density measurement provides a second temperature fluctuation estimate for comparison due to the lack of an applicable alternative temperature fluctuation measurement probe. The density-calculated temperature fluctuations were estimated from the power spectrum of the time-resolved density-calculated temperature record with the noise floor subtracted and are shown by the blue solid line in figure 5.62. The density-calculated temperature fluctuations are

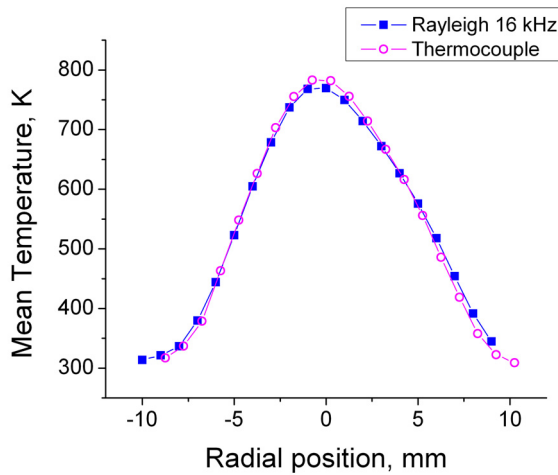


Figure 5.61. Mean temperature profile calculated from time-resolved Rayleigh data and measured by a thermocouple for a flow with maximum temperature and velocity of 775 K and 45 m/s.

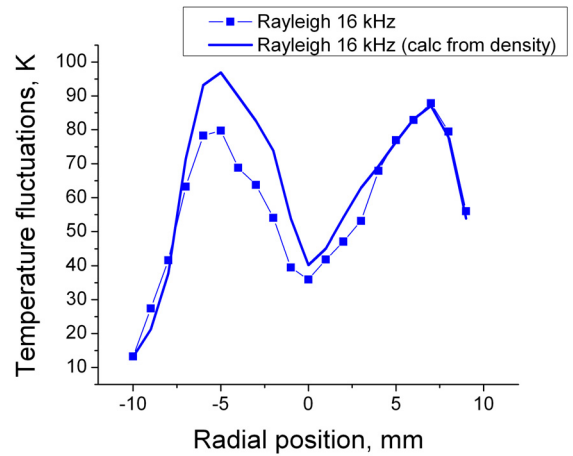


Figure 5.62. Temperature fluctuation profile calculated from Rayleigh measurements in a flow with maximum temperature and velocity of 775 K and 45 m/s.

quite a bit higher than the temperature fluctuation levels calculated from the 16 kHz direct temperature measurement on the left side (negative radial positions) of the jet centerline. The expected peak fluctuation levels should be on the order of 70 – 95 K, which is in agreement with the levels calculated in the shear layer from both the direct temperature measurement and the density-calculated temperature measurement. It is not clear what has led to the discrepancies between the two Rayleigh measurements observed in figure 5.62.

Figures 5.63 and 5.64 show radial profiles of mean velocity and turbulence velocity fluctuations, respectively, calculated from 16 kHz Rayleigh measurements compared with 32 kHz hotwire velocity measurements acquired in an unheated flow at a similar maximum velocity as the heated flow of case 3. The mean velocities from the Rayleigh measurements show some deviation from the hotwire measurements at points in the jet

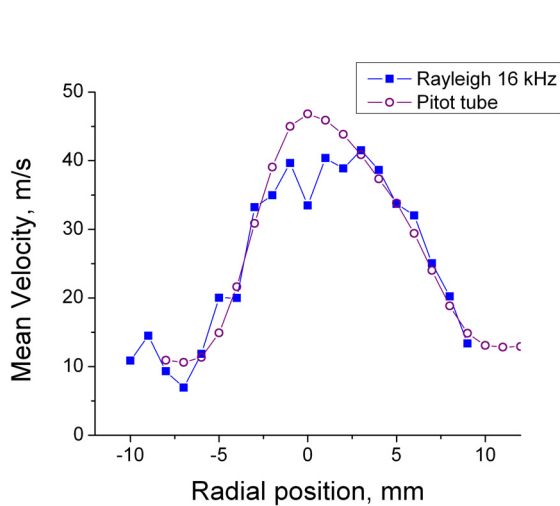


Figure 5.63. Mean velocity profile calculated from time-resolved Rayleigh data and pitot tube measurements in a flow with maximum temperature and velocity of 775 K and 45 m/s.

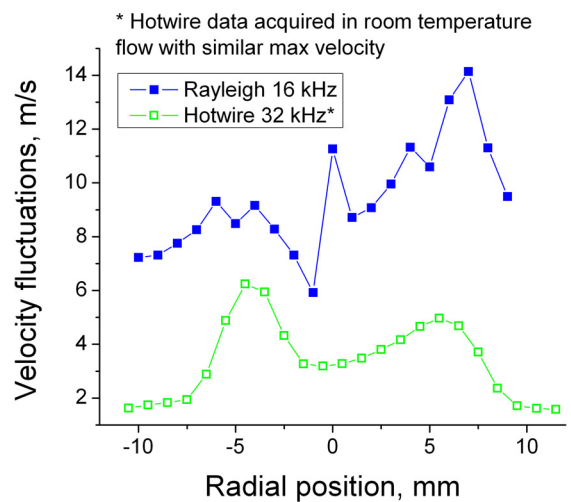


Figure 5.64. Velocity fluctuation profile calculated from Rayleigh measurements in a flow with maximum temperature and velocity of 775 K and 45 m/s and hotwire measurements in a room temperature flow with similar maximum velocity.

core where the temperatures are highest. High gas temperatures lead to difficulty in accurately determining the frequency shift due to a broad spectral peak. Also, the hotwire measurements were acquired at a different time in an unheated flow. It is possible that the velocity condition of the unheated jet was not matched perfectly with that of the heated jet of case 3. The hotwire measurements provide shear layer fluctuation levels that are in line with the 15-20% rule of thumb, which gives expected shear layer fluctuations of 5 – 7 m/s; however the Rayleigh measurements indicate fluctuation levels 2 – 7 m/s greater than these expected fluctuation levels. These discrepancies can potentially be explained by the reasons discussed previously: the Rayleigh velocity data exhibits erroneous fluctuations due to instability of the Rayleigh laser frequency and shot noise in the Rayleigh data results in a non-zero fluctuation amplitude measurement lower bound.

CHAPTER 6

CONCLUSIONS AND FUTURE WORK

6.1 Concluding statements

A technique for obtaining time-resolved gas velocity, temperature, and density measurements using molecular Rayleigh scattering was developed. Temperature and velocity were determined by analyzing the scattered light with a Fabry-Perot interferometer while density was determined from an overall intensity measurement of the scattered light. An image dissector, which consisted of four elliptical concentric mirrors with 12° angled surfaces, was designed to resolve the image of the circular Fabry-Perot interference pattern into one circular and three annular regions. The light imaged in each region was reflected and focused at four separate PMT detectors. An additional PMT was used to detect a sample of the collected light prior to spectral filtering providing a photon count measurement that is proportional to the total scattered intensity. The signals from the five PMTs were simultaneously recorded using photon counting at sampling rates up to 32 kHz. Maximum likelihood estimation using a model function that was developed for this application was used to estimate the temperature and velocity from the photon count data recorded at the output of the Fabry-Perot, while density was evaluated from a direct linear relationship with the overall intensity measurement.

Cramer-Rao lower bound analysis was used to calculate the expected uncertainty in instantaneous density, temperature and velocity measurements for the Rayleigh scattering experiments. The Cramer-Rao lower bound analysis was used to optimize the optical system parameters, such as radii of the image dissector mirrors and radius of the

reference fringe corresponding to incident laser light, by minimizing the measurement uncertainty within the temperature and velocity range of interest in these experiments. The lower bound uncertainty in the instantaneous parameter estimates were calculated as 5 – 22% in density, 35 – 200 K in temperature, and 17 – 80 m/s in velocity. These uncertainty estimates represent the expected rms error in the instantaneous measurements. The uncertainty is governed mainly by the shot noise in the photon count measurements. Increasing the mean photon counts increases the signal-to-noise ratio and improves the instantaneous measurement uncertainty. Various ways to improve the signal-to-noise ratio without reducing the sampling rate were discussed in Chapter 3. These included increasing the laser power, increasing the probe volume size, or increasing the collection cone angle. Although the uncertainty in the instantaneous measurements is rather high, the 2nd order statistics can be calculated with much lower uncertainty by using methods such as the Welch method of modified periodograms.

A numerical simulation of the optical measurement system was developed that included modeling of the Rayleigh scattering spectrum, spectral analysis with a Fabry-Perot interferometer, and photon counting detection including statistical shot noise. The numerical simulation was used to generate synthetic data with zero-turbulence velocity and temperature inputs. Analyzing the synthetic data provided a means of estimating the uncertainty in the 2nd order statistical properties calculated from the time-resolved Rayleigh measurements. This analysis demonstrated power spectrum noise floors of $6 \times 10^{-6} \text{ (kg/m}^3\text{)}^2\text{/Hz}$, 5 – 40 K²/Hz, and 0.5 – 5.5 (m/s)²/Hz for the density, temperature, and velocity power spectra, respectively. The frequency resolution of the power spectra

(7.8125 Hz) was used to calculate the fluctuation amplitude lower bound based on these power spectra noise floor values. The density fluctuation amplitude measurement lower bound is expected to be 0.006 kg/m^3 , the temperature fluctuation amplitude lower bound is $4 - 17 \text{ K}$, and the velocity fluctuation lower bound is $2 - 6.5 \text{ m/s}$. The simulation was validated by comparison with experimental data. The simulation provides a useful tool for designing future experiments in test facilities where run-time is limited and expensive.

The Rayleigh technique was validated in two experiments involving acoustic modulation of the flow field. An acoustically modulated unheated nozzle flow was used to validate velocity fluctuation measurements by comparison with hotwire measurements. An asymmetric oscillating counterflow with unequal enthalpies was studied to validate temperature and density fluctuations by comparison with coldwire measurements. Simultaneous measurements of all three flow properties using the Rayleigh technique were demonstrated at data rates up to 32 kHz in a high speed electrically-heated nozzle flow where temperature and density fluctuations were compared with coldwire measurements and velocity fluctuations were compared with hotwire measurements.

The minimum fluctuation measurement limits observed in the experimental data agreed with the simulation estimates. The power spectra calculated from the time-resolved velocity measurements in the acoustically-modulated nozzle flow demonstrated lower bounds of 2.2 m/s or less. The power spectra resulting from the data acquired in the asymmetric oscillating counterflow with unequal enthalpies experiment demonstrated

lower bounds of 7 – 9 K in temperature fluctuation measurements and 0.007 – 0.008 kg/m³ in density fluctuation measurements.

The calibration data exhibited mean temperature errors of ± 7 K and mean velocity errors of ± 7 m/s. The mean density measurements from Rayleigh measurements in the electrically-heated jet experiment had approximately 0.02 kg/m³ accuracy when compared to mean densities calculated from temperature measurements by physical probes (thermocouple and coldwire probes). The mean temperatures measured by the Rayleigh technique in these experiments had accuracies of approximately 5-12 K when compared with thermocouple measurements. The mean velocities exhibited errors of 4 – 10 m/s based on comparison with either pitot tube or hotwire measurements.

Investigations of the laser frequency drift and reference fringe radius accuracy resulted in velocity bias error estimates of 4 – 6 m/s. Fluctuation amplitude measurements of density, temperature, and velocity in the ranges of 0.02 – 0.125 kg/m³, 5 – 60 K, and 10 – 20 m/s with accuracies better than 0.01 kg/m³, 3 K, and 7 m/s were achieved, respectively.

6.2 Recommendations and future work

In future work, the velocity measurements will be improved by resolving issues related to the bias error due to erroneous velocity fluctuations. The laser used in these measurements was not frequency stabilized and therefore had inherent drift and resonance in its output frequency. The velocity measurement relies on having a very stable incident laser frequency, or the ability to monitor the laser frequency

simultaneously and account for any drift or changes in the reference laser frequency in the Rayleigh measurements. A Yb:YAG thin-disk laser has been purchased for use in future work. This laser can provide up to 7.5 Watts of power at 515 nm wavelength with the capability of implementing frequency control and stabilization in real time. It is unclear at this time if this laser will have similar resonance issues causing erroneous fluctuation peaks in the velocity power spectra; however the bias error in the mean velocity should be corrected by using a frequency-controlled source. Uncertainty in the reference fringe radius also induced some of the bias error evidenced in the mean velocity data; most of this uncertainty will be removed by using the new laser since most of the drift in reference fringe radius, and hence the need for the Fabry-Perot stabilization system, is due to laser frequency drift.

The efficiency of the data processing methods will also be improved to speed up the analysis time. The processing of the data files containing thousands of data records per file was extremely time-consuming due to the need to perform a MLE analysis for each individual data record containing the five photon count values. A single data file containing more than 160,000 photon count records may take as long as 2-3 hours to process. The processing code will be analyzed to determine ways to perform the calculations more efficiently. The code already uses a look-up-table approach for the TENTI S6 spectral calculations. A similar approach may be possible for the complete model function, eliminating several numerical integrations that are currently performed during each iteration in the MLE analysis. Utilizing a more powerful computer will also help to speed up the time required for data processing.

The presented Rayleigh scattering technique was developed for application in aeronautics research at NASA. As mentioned in Chapter 1, experiments are currently underway to evaluate the contribution of temperature fluctuations to far-field noise by application of the presented Rayleigh scattering technique in the SHJAR, a heated nozzle facility at NASA GRC. Sound pressure fluctuation (microphone) measurements will be acquired simultaneously with Rayleigh measurements allowing correlation between flow property fluctuations and noise generation. The results of the experiments will provide aeroacoustics researchers with information critical to computational model development for jet noise prediction. With experimental data as well as an accurate computational model, engineers will have the tools to develop ways to reduce aircraft noise levels and design quieter, more efficient aircraft. In addition to the tests in the SHJAR facility, future work also includes the integration of a Rayleigh scattering system in the 15 x 15 cm supersonic wind tunnel at NASA GRC, which is capable of generating flows up to Mach 3.5, to provide time-resolved flow measurements in the presence of shocks. A multiple-point measurement system is also planned for development in this facility to provide mass flux measurement capabilities. This work is in support of the Supersonic and Hypersonic elements of NASA's Fundamental Aeronautics Program.

APPENDIX A

RAMAN SCATTERING CONTRIBUTION TO RAYLEIGH SIGNAL

A.1 Introduction

The inelastic rotational Raman scattering signal falls in close proximity to the frequency of the incident laser. Therefore, it is critical to evaluate the potential contribution of Raman scattering to the detected Rayleigh signal and determine whether it must be included in the analysis of the data.

A.2. Rotational Raman scattering

Molecular light scattering consists of elastic (Rayleigh) and inelastic (Raman) scattering components. The inelastic or energy-exchanging scattering results in a frequency shift of the scattered light. The vibrational Raman bands are the furthest removed from the laser frequency with shifts on the order of a few hundred to a few thousand wavenumbers. This type of scattering clearly poses no threat of coinciding with the Rayleigh scattering signal, which occurs at or near the incident laser frequency. The rotational Raman band occurs in closer proximity to the laser frequency. The pure rotational Raman signal for diatomic molecules, such as N₂ and O₂, consists of a series of lines associated with the $\Delta J = \pm 2$ rotational transitions (Miles et al., 2001). A rotational Raman spectrum was calculated using the CARSFIT computer code (Farrow et al., 1985) for a gas composed of 80% N₂ and 20% O₂ at room temperature and atmospheric pressure and is shown in figure A.1. The contributions of the total signal from O₂ and N₂ are indicated by the green and red curves, respectively. Figure A.2 shows the rotational Raman lines closest to the excitation laser frequency for 80% N₂/20% O₂ gas at 300 K and the same gas at 775 K.

These calculations indicate that the rotational Raman lines closest to the laser frequency occur at approximately 12 cm^{-1} for N_2 , and approximately 14 cm^{-1} for O_2 and that the scattered intensity is greatly reduced as temperature increases but the Raman shifts remain the same. The Rayleigh linewidth for room temperature air is on the order of 0.037 cm^{-1} and is centered at the laser frequency ν_0 for a gas with no bulk velocity. For a flow with a bulk velocity of 200 m/s the Rayleigh line shift would be on the order of 0.018 cm^{-1} . Figure A.3 demonstrates the relative locations of the Rayleigh and rotational Raman lines for N_2 , indicating that the rotational Raman lines are far enough removed from the laser frequency such that they can be ignored in the Rayleigh spectral model. A Rayleigh line shift of 12 cm^{-1} would require a flow velocity of 136,000 m/s. Additionally, the Rayleigh scattering cross-section is typically 2 orders of magnitude greater than the rotational cross-sections; therefore the rotational Raman signal would comprise less than 1% of the total signal if it did coincide with the Rayleigh signal.

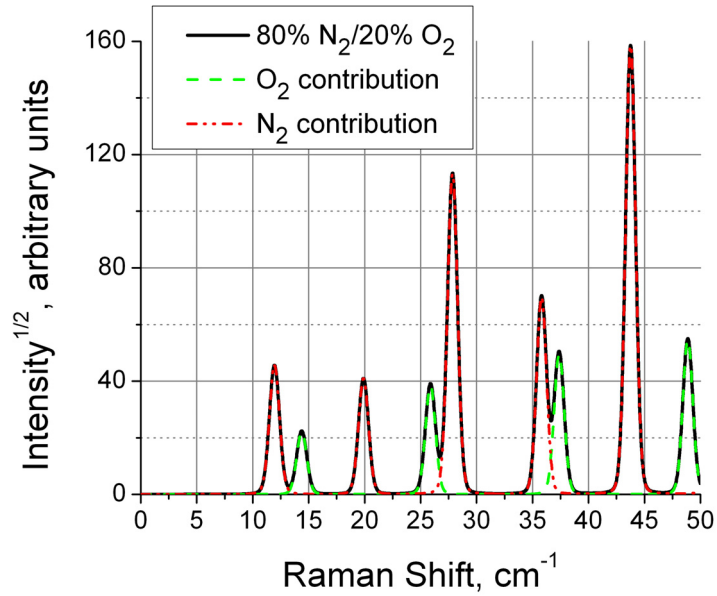


Figure A.1. Rotational Raman spectrum for a gas that is composed of 80% N₂ and 20% O₂ at room temperature and atmospheric pressure calculated by the CARSFIT code. The individual contributions from O₂ and N₂ are shown in green and red, respectively.

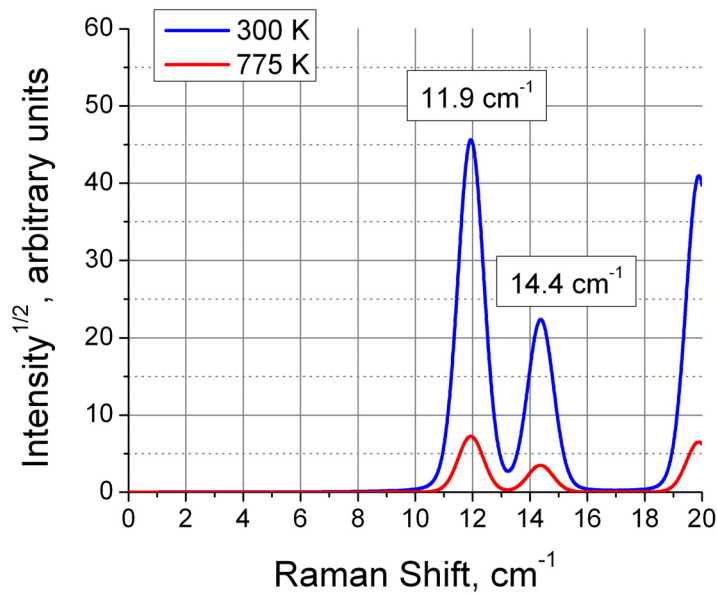


Figure A.2. Rotational Raman shifts closest to the excitation laser frequency for a gas that is composed of 80% N₂ and 20% O₂ at temperatures of 300 K and 775 K and atmospheric pressure calculated by the CARSFIT code.

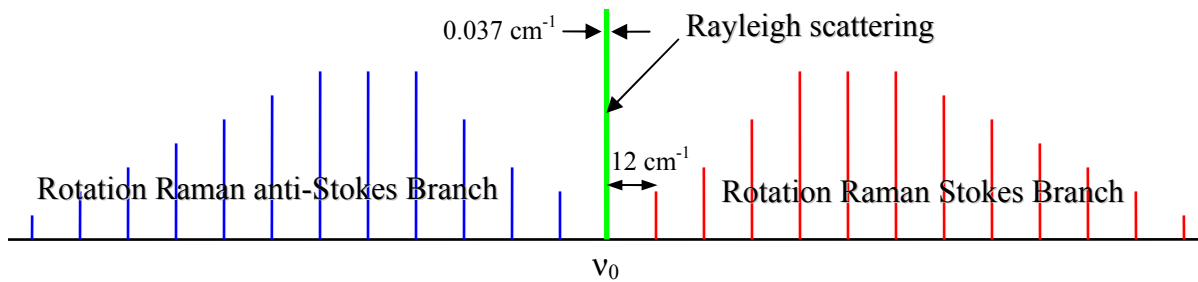


Figure A.3. Rotational Raman lines for N_2 relative to the Rayleigh line. The right and left wings of the Raman spectral lines are identified as the rotational Stokes and anti-Stokes branches, respectively.

APPENDIX B

THE POISSON DISTRIBUTION

B.1 Introduction

The Poisson distribution is the statistical probability distribution used to model experiments that count the number of occurrences of random events, such as photon counting experiments. The shot noise of photon counting experiments is often synonymously referred to as Poisson noise. The details of this discrete probability distribution are described in this appendix.

B.2. Poisson distribution

The Poisson distribution is a discrete probability distribution that is used to model experiments that count the number of events occurring at random during a given time interval, provided that the events occur with a definite average rate and are independent of the time since the last event. The formula for such a distribution is:

$$P(x, \mu) = \frac{e^{-\mu} \mu^x}{x!} \quad \text{for } x = 0, 1, 2, \dots \quad (\text{B-1})$$

where the shape parameter μ is a positive real number ($\mu > 0$) and is equal to the average number of events in the given time interval ($\mu = \langle x \rangle$). It has been shown that μ is equal to the variance ($\sigma^2 = \langle x^2 \rangle - \langle x \rangle^2$) of the distribution as well. (Taylor, 1982). For large values of μ , the discrete Poisson distribution is reasonably approximated by the continuous Gaussian distribution with the same mean and standard deviation.

$$G(x, \mu, \sigma) = \frac{1}{\sigma\sqrt{2\pi}} e^{-\frac{(x-\mu)^2}{2\sigma^2}} \quad (\text{B-2})$$

Figure B.1 shows the discrete Poisson distribution with $\mu = 25$ and the corresponding continuous Gaussian approximation. The number of occurrences fluctuates about the mean μ with a standard deviation $\sigma = \sqrt{\mu}$ and these fluctuations are called Poisson noise or “shot noise”. The photon counting performed in these experiments is a Poisson process with shot noise following a Poisson distribution. Although the standard deviation in the measurement increases as the average number of photons counted in a given time interval increases, the fractional uncertainty decreases as shown in figure B.2.

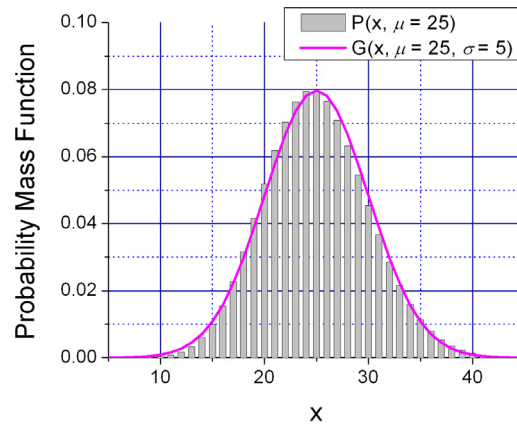


Figure B.1. Poisson and Gaussian distributions for $\mu = 25$.

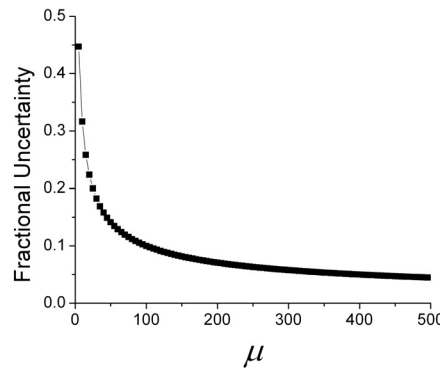


Figure B.2. Fractional uncertainty $\frac{\sqrt{\mu}}{\mu}$ as a function of mean number of counts μ .

APPENDIX C

CRAMER-RAO LOWER BOUND

C.1 Introduction

The relations to evaluate the Cramer-Rao lower bound (CRLB) for density, temperature, and velocity estimates in a Rayleigh scattering experiment assuming the spectrum is Gaussian and measured with an *ideal* instrument was derived. Following are the details of this analysis. A sample calculation for an *ideal* instrument is provided along with a discussion of how the lower bound was determined for a *real* instrument.

C.2 Derivation of the lower bound for an *ideal* instrument

For a measurement that is a set of unknown parameters $\beta_i = [\beta_1, \beta_2, \beta_3, \dots]$ it can be shown that any estimator for these parameters has a variance which cannot be less than a particular lower bound called the Cramer-Rao bound. Then the variance (σ_i^2) of the individual parameter estimates $\hat{\beta}_i$, where the hat denotes an estimate of the parameters β_i , satisfies the inequality (Whalen, 1971):

$$\sigma_i^2 \geq [\Gamma^{-1}]_{ii} \quad (C-1)$$

where Γ is the Fisher information matrix:

$$\Gamma_{i,j} = \sum_k \frac{1}{\sigma_k^2} \frac{\partial \langle N_k \rangle}{\partial \beta_i} \frac{\partial \langle N_k \rangle}{\partial \beta_j} \quad (C-2)$$

where $\langle N_k \rangle$ is the expected number of photoelectron counts in the Rayleigh spectrum over the frequency range f_k to $f_k + \Delta f$ and σ_k^2 is the variance of $\langle N_k \rangle$. For Poisson

statistics (Appendix B) where the expected or mean value is equal to the variance this matrix can be written as:

$$\Gamma_{i,j} = \sum_k \frac{1}{\langle N_k \rangle} \frac{\partial \langle N_k \rangle}{\partial \beta_i} \frac{\partial \langle N_k \rangle}{\partial \beta_j} \quad (\text{C-3})$$

The expected number of photoelectron counts $\langle N_k \rangle$ is evaluated by:

$$\langle N_k \rangle = \langle N_R \rangle S(f_k) \Delta f \quad (\text{C-4})$$

where $\langle N_R \rangle$ is the total number of Rayleigh scattered photoelectrons collected into solid angle Ω , which is proportional to the gas density ρ , and $S(f)$ is the normalized Gaussian spectrum, which is a function of gas temperature and velocity:

$$S(f) = \frac{2\sqrt{\pi}}{aK} e^{-\left(\frac{2\pi(f-f_o) - \vec{K} \cdot \vec{v}}{Ka}\right)^2} \quad (\text{C-5})$$

Substituting Eq. (C-4) in Eq. (C-3) we get

$$\Gamma_{i,j} = \sum_k \frac{1}{\langle N_R \rangle S(f_k) \Delta f} \frac{\partial [\langle N_R \rangle S(f_k) \Delta f]}{\partial \beta_i} \frac{\partial [\langle N_R \rangle S(f_k) \Delta f]}{\partial \beta_j} \quad (\text{C-6})$$

For sufficiently small Δf the sum can be expressed as an integral:

$$\Gamma_{i,j} = \int_{-\infty}^{\infty} \frac{1}{\langle N_R \rangle S(f)} \frac{\partial [\langle N_R \rangle S(f)]}{\partial \beta_i} \frac{\partial [\langle N_R \rangle S(f)]}{\partial \beta_j} df \quad (\text{C-7})$$

In the ideal experiment the unknown parameters are: $\beta_1 = \rho$; $\beta_2 = T$; $\beta_3 = u_k$. To evaluate the Fisher information matrix, the partial derivatives of the function $\langle N_R \rangle S(f)$ with respect to each of the unknown parameters must be evaluated. Let $\langle N_R \rangle = k' \rho$, where

k' is an arbitrary constant, and $\vec{K} \cdot \vec{v} = Ku_k$ where u_k is the velocity component in the \vec{K} direction. Also note that the normalized spectrum is not a function of ρ .

$$\frac{\partial[\langle N_R \rangle S(f)]}{\partial \rho} = \frac{\partial[\langle N_R \rangle]}{\partial \rho} S(f) \quad (\text{C-8})$$

$$\frac{\partial[\langle N_R \rangle S(f)]}{\partial T} = \langle N_R \rangle \frac{\partial S(f)}{\partial T} \quad (\text{C-9})$$

$$\frac{\partial[\langle N_R \rangle S(f)]}{\partial u_k} = \langle N_R \rangle \frac{\partial S(f)}{\partial u_k} \quad (\text{C-10})$$

The remaining derivatives were evaluated with the following results:

$$\frac{\partial[\langle N_R \rangle]}{\partial \rho} = \frac{\langle N_R \rangle}{\rho} \quad (\text{C-11})$$

$$\frac{\partial S(f)}{\partial T} = \frac{1}{T} \left[\left(\frac{2\pi(f-f_o) - Ku_k}{Ka} \right)^2 - \frac{1}{2} \right] S(f) \quad (\text{C-12})$$

$$\frac{\partial S(f)}{\partial u_k} = \frac{2}{a} \left(\frac{2\pi(f-f_o) - Ku_k}{Ka} \right) S(f) \quad (\text{C-13})$$

Now substitute Eqs. (C-8) – (C-13) into Eq. (C-7) and compute each element of the Fisher information matrix:

$$\Gamma_{1,1} = \int_{-\infty}^{\infty} \frac{1}{\langle N_R \rangle S(f)} \left[\frac{\langle N_R \rangle}{\rho} S(f) \right]^2 df = \frac{\langle N_R \rangle}{\rho^2} \int_{-\infty}^{\infty} S(f) df \quad (\text{C-14})$$

Since $S(f)$ is defined as the normalized spectrum, this means that $\int_{-\infty}^{\infty} S(f) df = 1$; therefore

$$\boxed{\Gamma_{1,1} = \frac{\langle N_R \rangle}{\rho^2}} \quad (\text{C-15})$$

$$\Gamma_{2,2} = \int_{-\infty}^{\infty} \frac{1}{\langle N_R \rangle S(f)} \left[\langle N_R \rangle \frac{1}{T} \left[\left(\frac{2\pi(f-f_o) - Ku_k}{Ka} \right)^2 - \frac{1}{2} \right] S(f) \right]^2 df \quad (C-16)$$

$$\Gamma_{2,2} = \frac{\langle N_R \rangle}{T^2} \int_{-\infty}^{\infty} \left[\left(\frac{2\pi(f-f_o) - Ku_k}{Ka} \right)^2 - \frac{1}{2} \right]^2 S(f) df \quad (C-17)$$

$$\boxed{\Gamma_{2,2} = \frac{\langle N_R \rangle}{2T^2}} \quad (C-18)$$

$$\Gamma_{3,3} = \int_{-\infty}^{\infty} \frac{1}{\langle N_R \rangle S(f)} \left[\langle N_R \rangle \frac{2}{a} \left(\frac{2\pi(f-f_o) - Ku_k}{Ka} \right) S(f) \right]^2 df \quad (C-19)$$

$$\Gamma_{3,3} = \langle N_R \rangle \left(\frac{2}{a} \right)^2 \int_{-\infty}^{\infty} \left(\frac{2\pi(f-f_o) - Ku_k}{Ka} \right)^2 S(f) df \quad (C-20)$$

$$\boxed{\Gamma_{3,3} = \frac{2\langle N_R \rangle}{a^2}} \quad (C-21)$$

It can be shown that the off-diagonal elements ($i \neq j$) are all equal to zero:

$$\boxed{\begin{aligned} \Gamma_{1,2} &= \Gamma_{2,1} = 0 \\ \Gamma_{1,3} &= \Gamma_{3,1} = 0 \\ \Gamma_{2,3} &= \Gamma_{3,2} = 0 \end{aligned}} \quad (C-22)$$

Therefore the Fisher information matrix is written in matrix form as:

$$\Gamma = \begin{bmatrix} \frac{\langle N_R \rangle}{\rho^2} & 0 & 0 \\ 0 & \frac{\langle N_R \rangle}{2T^2} & 0 \\ 0 & 0 & \frac{2\langle N_R \rangle}{a^2} \end{bmatrix}; \quad (C-23)$$

and the inverse of this matrix is

$$\Gamma^{-1} = \begin{bmatrix} \frac{\rho^2}{\langle N_R \rangle} & 0 & 0 \\ 0 & \frac{2T^2}{\langle N_R \rangle} & 0 \\ 0 & 0 & \frac{a^2}{2\langle N_R \rangle} \end{bmatrix} \quad (\text{C-24})$$

Therefore the variances in the estimates of the three unknown parameters if an ideal instrument is used to measure the Rayleigh spectrum are:

$$\sigma_\rho^2 \geq [\Gamma^{-1}]_{1,1} = \frac{\rho^2}{\langle N_R \rangle} \quad (\text{C-25})$$

$$\sigma_T^2 \geq [\Gamma^{-1}]_{2,2} = \frac{2T^2}{\langle N_R \rangle} \quad (\text{C-26})$$

$$\sigma_{u_k}^2 \geq [\Gamma^{-1}]_{3,3} = \frac{a^2}{2\langle N_R \rangle} \quad (\text{C-27})$$

C.3 Sample calculation of lower bound for an *ideal* loss-free instrument

Recall from Chapter 2 that the total Rayleigh scattered power in terms of photoelectron counts can be expressed as:

$$\langle N_R \rangle = \frac{\varepsilon P_0 n L_x \lambda \Omega \Delta t}{h c} \left(\frac{d\sigma}{d\Omega} \right) \sin^2 \beta \quad (2-16)$$

Assume typical values for an experiment performed in an air flow with static temperature of 298 K at standard atmospheric pressure using a sampling rate of 32 kHz and $f/4$ collection optics as given in Table C.1.

Table C.1. Experiment parameters for 32 kHz data rate and air at 298 K and 1 atm.

Parameter	Variable	Value
Optical system efficiency	ε	100% (loss-free)
Incident laser power	P_0	10 Watts
Molecular number density	n	$2.46 \times 10^{25} \text{ m}^{-3}$
Probe volume length	L_x	0.0011 m
Illumination wavelength	λ	$532 \times 10^{-9} \text{ m}$
Solid collection angle	Ω	0.049 sr
Integration time	Δt	$3.125 \times 10^{-5} \text{ s}$
Differential scattering cross-section	$\frac{d\sigma}{d\Omega}$	$5.9 \times 10^{-32} \text{ m}^2 \text{ sr}^{-1}$
Angle between \vec{E} and \vec{K}	β	90°
Planck's constant	h	$6.626 \times 10^{-34} \text{ N m s}$
Speed of light	c	$2.998 \times 10^8 \text{ m s}^{-1}$
Density	ρ	1.185 kg m^{-3}
Most probably molecular speed	a	413 m s^{-1}

Substituting these values into Eq. (2-16) gives $\langle N_R \rangle = 65472$ photoelectron counts occurring in a single time bin at a 32 kHz data rate. The required values were substituted into Eqs. (C-23) – (C-25) to obtain the lower bound uncertainty in the estimates of density, temperature, and velocity using an ideal instrument resulting in the following:

$$\sigma_\rho \geq 0.0046 \text{ kg/m}^3$$

$$\sigma_T \geq 1.65 \text{ K}$$

$$\sigma_{u_k} \geq 1.14 \text{ m/s}$$

C.4 Lower bound for a *real* instrument

In the actual experiment, a Fabry-Perot interferometer is used to resolve the spectrum of the scattered light, resulting in an interference pattern that is a convolution of the Rayleigh spectrum and the Fabry-Perot instrument function. This interference pattern is detected by PMT's that have detection efficiency less than 100%. The optical system also has other losses, such as coupling and transmission losses associated with the optical fiber and losses due to reflection or absorption at the various components in the optical path. The model function developed in Chapter 2, Eq. (2-19), takes into account the transmission properties of the Fabry-Perot and all system and detection losses. The Fisher information matrix was calculated using this function. The TENTI S6 spectral model was used to calculate the Rayleigh scattering spectrum in this analysis rather than using the simpler, less accurate Gaussian model used in the analysis above (Boley et al., 1972; Tenti et al., 1974). The derivatives of the model function with respect to the unknown parameters were evaluated using finite difference method. The uncertainty analysis results presented in Chapter 3 were evaluated by this method.

APPENDIX D

NUMERICAL SIMULATION OF RAYLEIGH PHOTON COUNT DATA

D.1 Introduction

The model function developed in Chapter 2 for the Fabry-Perot interference fringe pattern that contains the spectral information of the Rayleigh scattered light is used to generate simulated photon count data. Temperature and velocity values are provided as input for the simulation and *ideal* (noise-free) data are computed in terms of expected photon counts from each of the five PMTs based on Eqs. (2-16) and (2-19). In photon counting experiments, the counting events follow a Poisson distribution (Appendix B). Therefore, photon count values following a Poisson distribution simulating the electronic shot noise in the photon counting process are evaluated by generating random numbers based on the expected mean counts. The *ideal* and *noisy* simulated photon count values associated with PMTs 1-5 are recorded in a data file. The simulated data record is then be read into another program that performs MLE analysis on the simulated photon counts to determine instantaneous density, temperature, and velocity values. The MLE algorithm is identical to the data analysis performed on *experimental* data acquired in the experiments. The simulation provides a way to determine baseline noise levels that can be used in the design and optimization of experiments. Both the numerical simulation software and the MLE analysis software are written in FORTRAN programming language.

D.2 Computation algorithm

The assumptions and calculations involved in the numerical simulation are summarized in the following algorithm:

1. Read in temperature and velocity from input file
2. Assume static pressure is equal to the ambient pressure (101325 Pa)
3. Calculate molecular number density using ideal gas law
4. Calculate other temperature and pressure dependent fluid properties (shear and bulk viscosity, most probable molecular speed, thermal conductivity, γ -parameter)
5. Calculate the total number of Rayleigh scattered photons by Eq. (2-16)
6. Calculate the *ideal* photons counted by PMT 5 by taking into account system losses (coupling losses into fiber, transmission losses through fiber, beamsplitter losses, and detector efficiency). The overall efficiency may be estimated or evaluated from experiments.
7. Using the *ideal* mean number of photons detected by PMT 5, determine a random number based on a Poisson distribution to model the ‘shot noise’ of the photon counting process. The RNPOI subroutine from the International Mathematical and Statistical Libraries (IMSL) was used to generate pseudorandom deviates from a Poisson distribution with mean equal to the expected photon counts (IMSL Stat/Library, 1997).
8. Calculate the *ideal* photons transmitted through the Fabry-Perot interferometer including all system losses (coupling losses into fiber, transmission losses through fiber, beamsplitter losses, and interferometer reflectivity losses) except detector

efficiencies. The overall efficiency may be estimated or evaluated from experiments.

9. Integrate over each annular area of the circular interference pattern as split up by the concentric mirror image dissector and account for detector efficiency to determine the *ideal* mean number of photons detected by PMTs 1 – 4 using Eq. (2-19). Use IMSL RNPOI subroutine to generate pseudorandom photon count values from a Poisson distribution with mean equal to the expected photon counts.
10. Record the *ideal* and *noisy* photon count values in a data file for later MLE data analysis.
11. Repeat for all velocity and temperature records in the input data files.

The *noisy* data was analyzed using the same algorithm used to analyze the experimental data. The maximum likelihood parameter estimation algorithm is described in Appendix E. A schematic of the numerical simulation algorithm is shown in figure D.1.

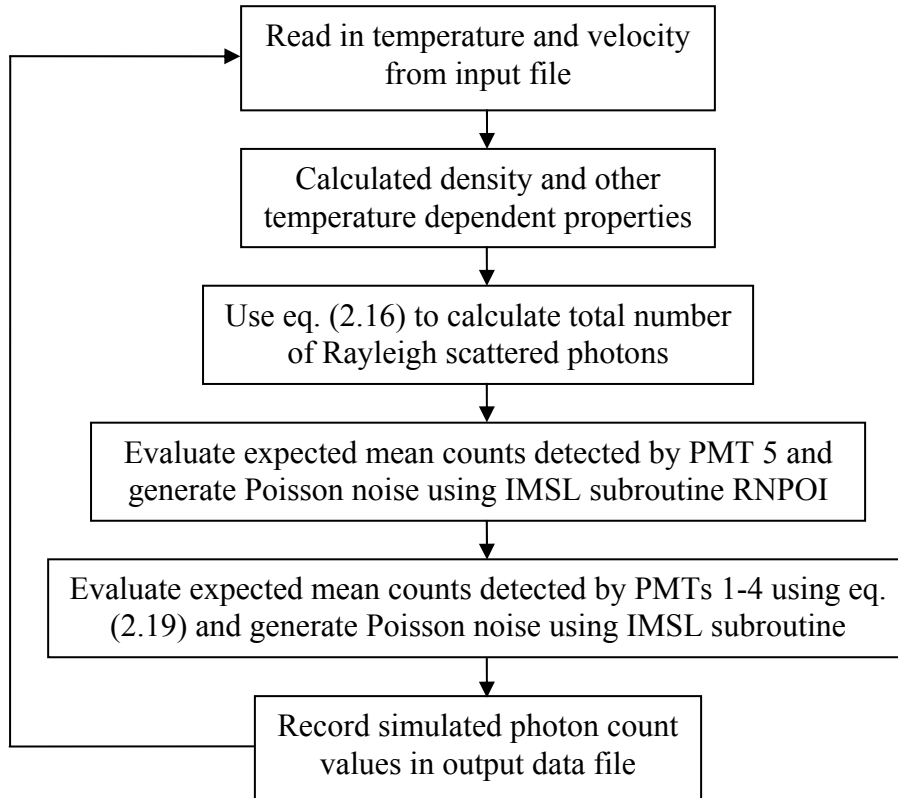


Figure D.1. Numerical Simulation Algorithm.

APPENDIX E

DATA ANALYSIS BY MAXIMUM LIKELIHOOD PARAMETER ESTIMATION

E.1 Introduction

The photon count data were analyzed by maximum likelihood estimation (MLE). Parameter estimation is the process of determining estimates of physical parameters by fitting a model function to experimental data. The fact that photon counting is a Poisson process was taken into account in determining the set of parameters that give the maximum likelihood estimate such that data with the smallest values were weighted the strongest. The details of this analysis are presented in this appendix.

E.2 Model function and parameter estimation

The model function for Rayleigh scattering data was developed in Chapter 2. The expected number of photoelectron counts detected within the q^{th} annular region of the interference pattern, which has been dissected into one circular and three annular regions is given by:

$$\langle N_q \rangle = \frac{\langle N_R \rangle}{\pi r_{\text{max}}^2} 2\pi \int_{r_{i,q}}^{r_{o,q}} \int_{-\infty}^{\infty} S_R(x_f) I_{FP}(x_f, r) r dx_f dr \quad (2-19)$$

were the Rayleigh spectrum S_R is evaluated by the TENTI S6 model calculated using a computer code provided by Professor G. Tenti (Boley et al., 1972; Tenti et al., 1974). The model function includes a number of parameters that may be known or unknown, such as radius of the fringe at the laser frequency, efficiency factors, Fabry-Perot finesse, and fringe forming lens focal length, in addition to the main parameters of interest, which include gas density ρ , gas temperature T , and the axial component of the gas velocity u_k .

These unknown parameters are estimated by fitting the model function to the experimental data using the procedure described below. The notation used by Beck and Arnold (1977) will be adopted in the development of the parameter estimation process. The model function is $\eta_q = \langle N_q \rangle$ and the photon count data are given by Y_q where q denotes a photodetector (PMT). The parameter estimates are found by minimizing the weighted sum of residuals, which gives the maximum likelihood estimate (Beck & Arnold, 1977; Edwards, 2006):

$$S_{ML} = \sum_q \frac{1}{V_q} (Y_q - \eta_q) \quad (\text{E-1})$$

where V_q is the variance of the q^{th} measurement. For errors associated with a Poisson process (photon counting), the variance is simply equal to the mean and the sum of residuals becomes:

$$S_{ML} = \sum_q \frac{1}{\eta_q} (Y_q - \eta_q) \quad (\text{E-2})$$

Since the model function is nonlinear in the parameters an iterative procedure must be used to determine the estimates; the Gauss method will be used (Beck & Arnold, 1977).

Using the matrix notation of Beck and Arnold (1977), the model function for M measurements and P parameters can be written as:

$$\boldsymbol{\eta} = \mathbf{X}\boldsymbol{\beta} \quad (\text{E-3})$$

such that

$$\boldsymbol{\eta} = \begin{bmatrix} \eta_1 \\ \eta_2 \\ \vdots \\ \eta_M \end{bmatrix}, \mathbf{X} = \begin{bmatrix} X_{11} & X_{12} & \cdots & X_{1P} \\ X_{21} & X_{22} & \cdots & X_{2P} \\ \vdots & \vdots & \ddots & \vdots \\ X_{M1} & X_{M2} & \cdots & X_{MP} \end{bmatrix}, \boldsymbol{\beta} = \begin{bmatrix} \beta_1 \\ \beta_2 \\ \vdots \\ \beta_P \end{bmatrix}$$

$$\text{and } \eta_q = \sum_{i=1}^P X_{qi} \beta_i, \quad q = 1, 2, \dots, M$$

where \mathbf{X} is the sensitivity matrix with elements

$$X_{qi} = \frac{\partial \eta_q}{\partial \beta_i} \quad (\text{E-4})$$

The expression for the sum of residuals can be written as:

$$S_{ML} = (\mathbf{Y} - \mathbf{X}\boldsymbol{\beta})^T \boldsymbol{\Psi}^{-1} (\mathbf{Y} - \mathbf{X}\boldsymbol{\beta}) \quad (\text{E-5})$$

where \mathbf{Y} is defined as:

$$\mathbf{Y} = \boldsymbol{\eta} + \boldsymbol{\varepsilon} \quad (\text{E-6})$$

and $\boldsymbol{\Psi}$ is the variance-covariance matrix of \mathbf{Y} . If \mathbf{Y} has additive zero mean errors $\boldsymbol{\varepsilon}$, the following equalities are true for the expected value and variance-covariance matrix of \mathbf{Y} :

$$E(\mathbf{Y}) = E(\boldsymbol{\eta}) \quad (\text{E-7})$$

$$\boldsymbol{\Psi} = \text{cov}(\mathbf{Y}) = \text{cov}(\boldsymbol{\varepsilon}) \quad (\text{E-8})$$

The variance-covariance matrix of the errors can be written as:

$$\boldsymbol{\Psi} = \begin{bmatrix} E(\varepsilon_1^2) & E(\varepsilon_1 \varepsilon_2) & \cdots & E(\varepsilon_1 \varepsilon_M) \\ E(\varepsilon_2 \varepsilon_1) & E(\varepsilon_2^2) & \cdots & \vdots \\ \vdots & \vdots & \ddots & \vdots \\ E(\varepsilon_M \varepsilon_1) & E(\varepsilon_M \varepsilon_2) & \cdots & E(\varepsilon_M^2) \end{bmatrix} \quad (\text{E-9})$$

If the errors are uncorrelated then

$$E(\varepsilon_i \varepsilon_j) = 0, \quad i \neq j \quad (\text{E-10})$$

$$E(\varepsilon_i^2) = V(Y_i) \quad (\text{E-11})$$

and the variance-covariance matrix of the errors becomes:

$$\boldsymbol{\Psi} = \begin{bmatrix} V(Y_1) & 0 & \cdots & 0 \\ 0 & V(Y_2) & \cdots & \vdots \\ \vdots & \vdots & \ddots & \vdots \\ 0 & 0 & \cdots & V(Y_M) \end{bmatrix} \quad (\text{E-12})$$

Since \mathbf{Y} is a Poisson process then the variance of \mathbf{Y} may be written as:

$$V(Y_i) = E(Y_i) = \eta_i \quad (\text{E-13})$$

An unbiased maximum likelihood estimator of the parameters $\boldsymbol{\beta}$ is (Beck & Arnold, 1977):

$$\boldsymbol{\beta} = E(\mathbf{b}_{\text{ML}}) \quad (\text{E-14})$$

where

$$\mathbf{b}_{\text{ML}} = (\mathbf{X}^T \boldsymbol{\Psi}^{-1} \mathbf{X})^{-1} \mathbf{X}^T \boldsymbol{\Psi}^{-1} \mathbf{Y} \quad (\text{E-15})$$

Let

$$\mathbf{P}_{\text{ML}} = (\mathbf{X}^T \boldsymbol{\Psi}^{-1} \mathbf{X})^{-1} \quad (\text{E-16})$$

and note that

$$(\mathbf{X}^T \boldsymbol{\Psi}^{-1} \mathbf{X})_{ij} = \mathbf{X}_{ik}^T (\boldsymbol{\Psi}^{-1})_{kl} \mathbf{X}_{lj} \quad (\text{E-17})$$

Since $\boldsymbol{\Psi}$ is diagonal,

$$(\boldsymbol{\Psi}^{-1})_{kl} = (\boldsymbol{\Psi}^{-1})_{kl} \delta_{kl}, \quad \text{where } \delta_{kl} = \begin{cases} 1 & \text{for } k = l \\ 0 & \text{for } k \neq l \end{cases} \quad (\text{E-18})$$

then

$$(\mathbf{X}^T \boldsymbol{\Psi}^{-1} \mathbf{X})_{ij} = X_{ik}^T (\boldsymbol{\Psi}^{-1})_{kk} X_{kj} = X_{ki} (\boldsymbol{\Psi}^{-1})_{kk} X_{kj} \quad (\text{E-19})$$

and

$$(\mathbf{P}_{ML}^{-1})_{ij} = \sum_{k=1}^M X_{ki} (\boldsymbol{\Psi}^{-1})_{kk} X_{kj} = \sum_{k=1}^M \frac{\partial \eta_k}{\partial \beta_i} \frac{1}{V(Y_k)} \frac{\partial \eta_k}{\partial \beta_j} \quad (\text{E-20})$$

Note that this is the Fisher information matrix which was previously denoted by $\boldsymbol{\Gamma}$ in

Appendix C:

$$\mathbf{P}_{ML} = \boldsymbol{\Gamma}^{-1} \quad (\text{E-21})$$

Define a vector \mathbf{H} such that:

$$H_i = \mathbf{X}^T \boldsymbol{\Psi}^{-1} \mathbf{Y} = \sum_{k=1}^M \frac{\partial \eta_k}{\partial \beta_i} \frac{1}{V(Y_k)} (Y_k - \eta_k) \quad (\text{E-22})$$

If the model were linear in the parameters, the parameter estimates would be given by

$$b_{ML_j} = \sum_{i=1}^P \Gamma_{ji}^{-1} H_i, \quad \text{for } j = 1 \dots P \quad (\text{E-23})$$

In this case the model is nonlinear in the parameters and an iterative procedure known as the Gauss method is required to obtain the parameter estimates by repeatedly applying the following:

$$b_j^{(k+1)} = b_j^{(k)} + \sum_{i=1}^P \Gamma_{ji}^{-1} H_i, \quad \text{for } j = 1 \dots P \quad (\text{E-24})$$

An initial *guess* $\mathbf{b}^{(0)}$ for each parameter must be supplied to start the iteration. Iteration is continued until convergence is achieved. Convergence is determined by checking the change in \mathbf{b} for successive iterations until the change is less than some value δ :

$$\left| b_j^{(k+1)} - b_j^k \right| < \delta_j, \quad \text{for all } b_j \quad (\text{E-25})$$

E.3 Algorithm for parameter estimation of experimental data

The following assumptions are made in the maximum likelihood analysis of the experimental data:

1. The variance-covariance matrix of the errors is diagonal and can be expressed by Eq. (E-12).
2. The variance of the errors is the sum of the photon statistical noise plus the read noise. For the q^{th} detector with measured value Y_q the variance is:

$$V(Y_q) = V_{read} + \eta_q \quad (\text{E-26})$$

The following algorithm is implemented for the estimation of the unknown parameters ρ , T , and u_k :

1. Read all relevant known or calibrated parameters, such as radius of the fringe at the laser frequency, efficiency factors, Fabry-Perot finesse, and fringe forming lens focal length, from the parameter input file.
2. Read in photon counts acquired by PMTs 1-5 from data file ($Y_q, q = 1 \dots 5$).
3. Replace statistical outliers (more than 3 standard deviations from the mean) with average of the preceding and succeeding values.
4. Read ambient pressure, total pressure, and total temperature measured by additional experiment instrumentation from data file.
5. Evaluate ρ via the linear relationship with Y_5 as determined by experiment calibration.

6. Evaluate initial guesses for T and u_k using isentropic flow relations with measured static and total pressure and total temperature as input or use values measured by alternate instrumentation (thermocouple, pitot tube, etc.).
7. If $k = 1$, where k is the iteration number, set T and u_k to the initial guesses; otherwise set T and u_k to their iterated values.
8. For $k = 1$ set static pressure to the measured ambient pressure; for $k > 1$ evaluate static pressure using ideal gas law with ρ evaluated from Y_5 and T for the current iteration.
9. Evaluate other temperature and pressure dependent fluid properties (shear and bulk viscosity, most probable molecular speed, thermal conductivity, γ -parameter)
10. Evaluate η_q for $q = 1,2,3,4$ using the model function given by Eq. (2-19) with the current parameter values.
11. Compute the sensitivity matrix \mathbf{X} for the parameter values using Eq. (E-4).
Evaluate the partial derivatives using finite difference method.
12. Compute the Fisher information matrix $\mathbf{\Gamma}$ using Eq. (E-20).
13. Compute the inverse Fisher matrix $\mathbf{\Gamma}^{-1}$.
14. Compute the \mathbf{H} vector using Eq. (E-22).
15. Compute the iterated parameter estimates using Eq. (E-24).
16. Check if convergence has been achieved by Eq. (E-25).
17. If not converged, go to step 6 and repeat until convergence is achieved or until maximum number of allowed iterations is reached ($k_{max} = 40$).
18. Upon convergence write ρ , T , and u_k estimates to output file.

19. Go to step 2 and repeat until parameter estimation has been completed for all photon count records in the data file. A single data file may contain as many as 163840 records depending on the data sampling rate used in the experiments.

APPENDIX F

VELOCITY BIAS ERROR DUE TO LASER FREQUENCY INSTABILITY

F.1. Introduction

It was not uncommon to observe velocity bias error in the Rayleigh measurements by as much as 5-10 m/s. After further investigation, it was found that this bias is mainly due to laser frequency drift (as much as 10 MHz drift over 30 seconds) and/or uncertainty in the reference fringe radius due to limitations of how tightly the Fabry-Perot stabilization system can maintain the fringe radius as the laser frequency changes. The current experiment does not have a way to monitor the laser frequency or the reference fringe radius in real time while the data is acquired to account for them properly in the data analysis. Any frequency drift during the data acquisition period will be manifest as an apparent velocity drift. Similarly, any error in the reference fringe radius, which is directly related to the laser frequency, will produce bias error in the velocity measurement. In this appendix the amount of velocity bias error that is associated with the laser frequency drift and reference fringe radius error will be quantified.

F.2 Velocity bias error in Rayleigh measurements

Some of the results shown in Chapter 5 exhibited bias error in the mean Rayleigh velocity measurements. Two sample data points were chosen to demonstrate the drift in velocity over the time-period of the data acquisition, which is most likely caused by drift in the laser frequency. Figures F.1 and F.2 show time-resolved velocity measurements for heated jet case 1 at radial positions of 0 and -1 mm, respectively, along with a linear curve fit of each data record. The mean flow velocities based on pitot tube measurements

are given at the bottom of each plot. The linear curve fit in figure F.1 has a slope indicating a downward drift in velocity from 36.5 m/s to 30 m/s over the 10 second data acquisition time. The measured velocity at the start of the acquisition period agrees with the pitot tube measured value however the downward drift in velocity causes the mean value to be slightly lower than expected. The curve fit in figure F.2 indicates a slightly upward drift in velocity from 34.5 m/s to 39.2 m/s, where the velocity measured near the end of the acquisition period is closer to the pitot tube measured velocity. The fact that the velocity measurement at that start of the acquisition was biased low indicates that there is another source of error besides laser frequency drift. This additional error source is the uncertainty in the reference fringe radius resulting from accuracy limitations of the stabilization system. In the data analysis the reference fringe radius is assumed to be 6.5 mm, as set by the input to the stabilization system which adjusts the Fabry-Perot mirror spacing until the fringe is the desired size; however the stabilization system can only maintain the radius to within ± 0.01 mm. The combination of laser drift and accuracy limitations in setting the reference fringe radius are the main contributors to the bias error observed in the Rayleigh velocity measurements.

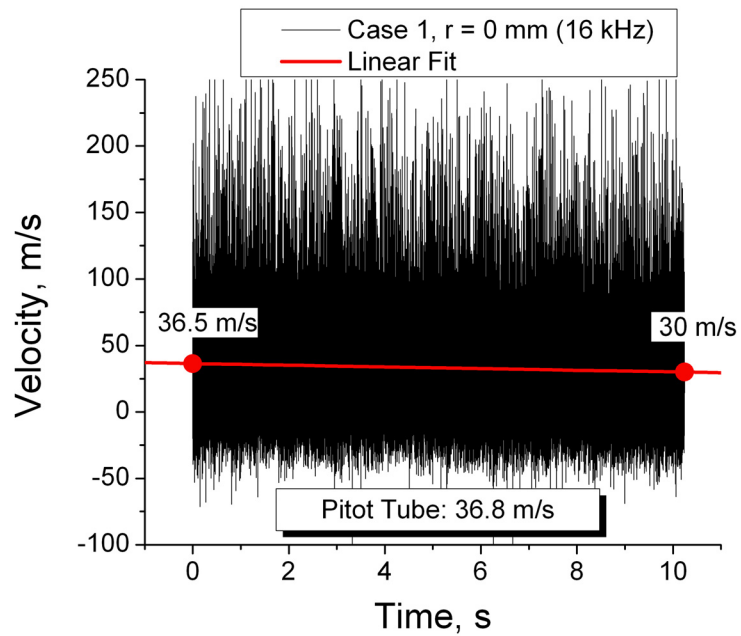


Figure F.1. Time resolved Rayleigh velocity data for experiment 3 (case 1) and a radial position of 0 mm. The linear curve fit shows a drift in mean velocity from 36.5 m/s to 30 m/s over the 10 second data acquisition time.

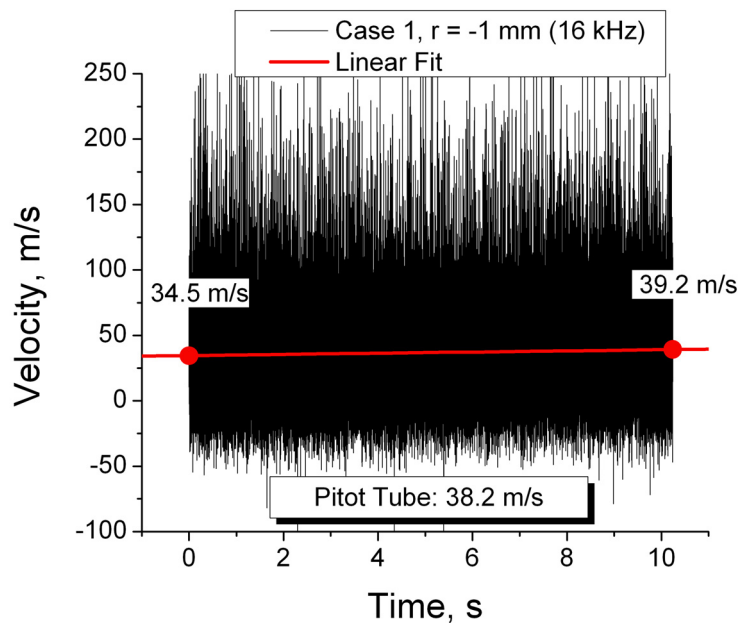


Figure F.2. Time resolved Rayleigh velocity data for experiment 3 (case 1) and a radial position of -1 mm. The linear curve fit shows a drift in mean velocity from 34.5 m/s to 39.2 m/s over the 10 second data acquisition time.

F.3. Laser frequency instability

The drift or instability of the output frequency of the Coherent 10 Watt Verdi laser was monitored by observing the radius of the Fabry-Perot fringe pattern. The radius of the fringe can be related to the change in laser frequency (Δf) by the following analysis:

$$\frac{r}{r_0} = \left[1 + \frac{\Delta f}{n_0 FSR} \right]^{1/2} \quad (\text{F-1})$$

$$n_0 = \frac{d}{\lambda} \left[\frac{r_0}{f_L} \right]^2 \quad (\text{F-2})$$

where n_0 is the fringe order, d is the Fabry-Perot mirror spacing, λ is the illumination wavelength, FSR is the free spectral range of the instrument, f_L is the focal length of lens that focuses the fringe pattern at the image plane, and Δf is the change in frequency associated with the change in fringe radius from r_0 to r . The frequency was monitored during periods when the data acquisition system was in the feedback stabilization mode, and also when the stabilization was deactivated. Figure F.3 shows a portion of the data collected for this laser over a 30 minute period during which the stabilization mode was cycled on and off for several minutes at time. The laser frequency drift is indicated by the black curve and the left axis, while the status of stabilization is shown by the blue curve and the right axis. A status of 0 indicates that the stabilization was inactive and the drift seen was purely related to the laser drift. During active stabilization (status = 1) the Fabry-Perot mirror spacing is adjusted by piezoelectric transducers to account for laser drift and maintain a set fringe radius. Even in the stabilizing mode, the equivalent frequency drift was approximately ± 5 MHz. Without stabilization the frequency drifted by approximately ± 10 MHz. Figure F.4 shows a shorter time segment of the frequency

drift data during a 10 minute period when the stabilization mode was deactivated for 5 minutes and then activated for 5 minutes. In this figure it is clearly evident that the laser output has frequency oscillations with a peak-to-peak period of 30 seconds.

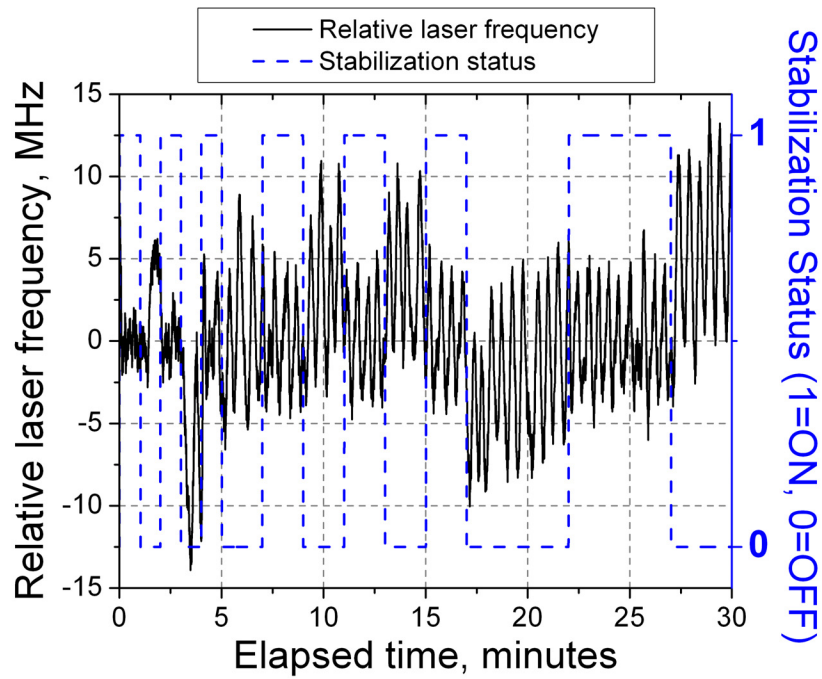


Figure F.3. Frequency drift data for the Coherent 10 Watt Verdi laser over a 30 minute period during which the stabilization feedback system is cycled on and off for several minutes at a time.

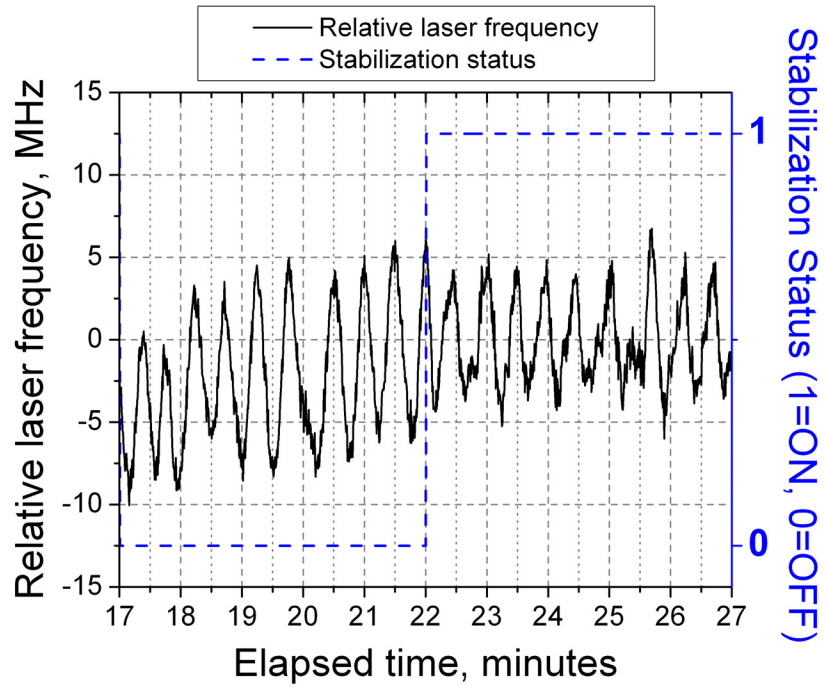


Figure F.4. Frequency drift of the Coherent 10 Watt Verdi laser in the 10 minute interval from 17 to 27 minutes shown in figure F.3 during which the Fabry-Perot stabilization is deactivated for the first 5 minutes and is active for the latter 5 minutes. This plot demonstrates the 30 second oscillation period of the laser.

F.4 Quantification of velocity error associated with laser frequency instability

The velocity error induced by a frequency drift of 10 MHz can be determined by calculating the velocity associated with an equivalent Doppler frequency shift:

$$u_k = \frac{2\pi \Delta f}{K} \quad (\text{F-3})$$

where K is the magnitude of the interaction wave vector calculated using Eq. (2-4) as 16702567 m^{-1} . Therefore, the velocity bias error for a 10 MHz frequency shift is 3.8 m/s. The accuracy limit of maintaining the reference fringe radius at the desired value results in potential reference frequency error of 5 MHz or a velocity bias of 1.9 m/s. Therefore, the worst case scenario for velocity bias error based on these two error source estimates is 5.7 m/s.

F.5 Potential solutions for reducing bias error

Attempts were made in the current work to eliminate some of the error by using fringe radius information recorded via the stabilization system software approximately 15 seconds prior to Rayleigh data acquisition and approximately 5 seconds after completion of the data acquisition. This allowed us to determine a more accurate reference fringe radius value for each measurement point; however it did not take into account radius change induced by laser frequency drift and/or Fabry-Perot mirror drift during the data acquisition time since it is currently not possible to record this information during collection of the Rayleigh signal. Using the radius information improved the velocity measurements slightly; however bias errors of 5 – 10 m/s were still observed in some instances.

The best solution to the bias error problem is real time monitoring of the laser frequency during Rayleigh data acquisition. Possible ways of implementing such monitoring will be investigated in future work. One possibility is to install a second optical fiber which collects a small portion of the incident laser light. This light can be directed through the same Fabry-Perot interferometer as the Rayleigh light but on a different optical path using different regions of the Fabry-Perot mirror surfaces. A two-mirror dissection and two-PMT detection system could be used to monitor the diameter of the reference fringe radius simultaneously with the Rayleigh scattering detection system. However, extreme care must be taken to avoid contamination of the Rayleigh signal with direct laser light.

BIBLIOGRAPHY

- Ahn, T., Adamovich, I., & Lempert, W. R. (2005) Stimulated Raman scattering measurements of V V transfer in oxygen. *Chem. Phys.*, 323, 532-544.
- Allen, M. G. (1998) Diode laser absorption sensors for gas-dynamic and combustion flows. *Meas. Sci. Technol.*, 9, 545-562.
- Barker, P. F., Grinstead, J. H., & Miles, R. B. (1999) Single-pulse temperature measurement in supersonic air flow with predissociated laser-induced thermal gratings. *Optics Comm.*, 168, 177-182.
- Beck, J. V., & Arnold, K. J. (1977) *Parameter estimation in engineering and science*. New York: John Wiley & Sons.
- Bell, W. A. (1982) Spectral analysis algorithms for the laser velocimeter: A comparative study. *AIAA Journal*, 21, 714-719.
- Benedict, L. H., Nobach, H., & Tropea, C. (2000) Estimation of turbulent velocity spectra from laser doppler data. *Meas. Sci. Technol.*, 11, 1089-1104.
- Bivolaru, D., Danehy, P. M., Grinstead, K. D., Tedder, S., & Cutler, A. D. (2006) Simultaneous CARS and interferometric Rayleigh scattering. *AIAA paper # 2006-2968*.
- Boguszko, M., & Elliott, G. S. (2005) On the use of filtered Rayleigh scattering for measurements in compressible flows and thermal fields. *Exp. Fluids*, 38, 33-49.
- Boley, C. D., Desai, R. C., & Tenti, G. (1972) Kinetic models and Brillouin scattering in a molecular gas. *Can. J. Phys.*, 50, 2158-2173.
- Bonnet, J. P., Grésillon, D., Cabrit, B., & Frolov, V. (1995) Collective light scattering as non-particle laser velocimetry. *Meas. Sci. Technol.*, 6, 620-636.
- Bruchhausen, M., Guillard, F., & Lemoine, F. (2005) Instantaneous measurement of two-dimensional temperature distributions by means of two-color planar laser induced fluorescence (PLIF). *Exp. Fluids*, 38, 123-131.
- Callen, H. B., Barasch, M. L., & Jackson, J. L. (1952) Statistical mechanics of irreversibility. *Phys. Rev.*, 88, 1382-1386.
- Cecil, E., & McDaniel, C. (2005) Planar velocity and temperature measurements in rarefied hypersonic flow using iodine LIF. *AIAA paper # 2005-4695*.

- Chang, A. Y., DiRosa, M. D., Davidson, D. F., & Hanson, R. K. (1991) Rapid tuning cw laser technique for measurements of gas velocity, temperature, pressure, density, and mass flux using NO. *Appl. Optics*, *30*, 3011-3022.
- Chen, T. H., Goss, L. P., Trump, D. D., & Schmoll, W. J. (1988) Studies of a turbulent premixed flame using CARS-LDV diagnostics. *AIAA paper # 1988-3194*.
- Chen, Y. C., & Mansour, M. S. (1997) Simultaneous Rayleigh scattering and laser-induced CH fluorescence for reaction zone imaging in high-speed premixed hydrocarbon flames. *Appl. Phys. B*, *64*, 599-605.
- Clark, N. A. (1975) Inelastic light scattering from density fluctuations in dilute gases: The kinetic hydrodynamic transition in monoatomic gas. *Phys. Rev.*, *A12*, 232-244.
- Cummings, E. B. (1995) Laser-induced thermal acoustics. *Doctoral Dissertation, California Institute of Technology, Pasadena, CA*.
- Cummings, E. B., Hornung, H. G., Brown, M. S., & DeBarber, P. A. (1995) Measurement of gas-phase sound speed and thermal diffusivity over a broad range using laser-induced thermal acoustics. *Optics Letters*, *20*, 1577-1579.
- Dec, J.E., & Keller, J.O., (1990) Time-resolved gas temperatures in the oscillating turbulent flow of a pulse combustor tail pipe. *Combustion and Flame*, *80*, 358-370.
- Dégardin, O., Renou, B., Boukhalfa, A. M., & Dominguez, E. (2004) Local flame structure analysis of stratified V-shaped flame by Rayleigh scattering and PLIF on acetone. Proceedings from *the 12th International Symposium on Applications of Laser Techniques to Fluid Mechanics*, Lisbon, Portugal, paper # 4-5.
- Eckbreth, A. C. (1996) *Laser diagnostics for combustion temperature and species* (2nd ed.). New York: Gordon and Breach: Combustion Science and Technology Series.
- Edwards, R. V. (2006) *Processing random data: Statistics for engineers and scientists*. Hackensack, NJ: World Scientific Publishing.
- Eichler, H. J. (1986) Introduction to the special issue on dynamic gratings and four-wave mixing. *IEEE J. Quantum Electronics*, *QE-22*, 1194-1195.
- Fajardo, C. M., Smith, J. D., & Sick, V. (2006) Sustained simultaneous high-speed imaging of scalar and velocity fields using a single laser. *Appl. Phys. B*, *85*, 25-31.

- Farrow, R. L., Lutch, R. P., Clark, G. L., and Palmer, R. E. (1985) Species concentration measurements using CARS with nonresonant susceptibility normalization. *Appl. Opt.*, 24, 2241-2251.
- Forkey, J. N., Lempert, W. R., & Miles, R. B. (1997) Corrected and calibrated I₂ absorption model at frequency-doubled Nd:YAG laser wavelengths. *Appl. Optics*, 36, 6729-6738.
- Forkey, J. N., Lempert, W. R., & Miles, R. B. (1998) Accuracy limits for planar measurements of flow field velocity, temperature and pressure using filtered Rayleigh scattering. *Exp. Fluids*, 24, 151-162.
- Giezendanner-Thoben, R., Meier, U., Meier, W., Heinze, J., & Aigner, M. (2005) Phase-locked two-line OH planar laser-induced fluorescence thermometry in a pulsating gas turbine model combustor at atmospheric pressure. *Appl. Optics*, 44, 6565-6577.
- Hanson, R. K., & Jeffries, J. B. (2006) Diode laser sensors for ground testing. *AIAA paper # 2006-3441*.
- Hart, R. C., Balla, R. J., & Herring, G. C. (1999) Nonresonant referenced laser-induced acoustics thermometry in air. *Appl. Optics.*, 38, 577-584.
- Hemmerling, B., Kozlov, D. N., & Stampanoni-Panariello, A. (2000) Temperature and flow-velocity measurements by use of laser-induced electrostrictive gratings. *Optics Letters*, 25, 1340-1342.
- Hillard, M. E., Hunter, W. W., Meyers, J. F., & Feller, W. V. (1974) Simultaneous Raman and laser velocimeter measurements. *AIAA Journal*, 12, 1445-1447.
- Hu, H., & Koochesfahani, M. M., (2006) Molecular tagging velocimetry and thermometry and its application to the wake of a heated circular cylinder. *Meas. Sci. Technol.*, 17, 1269-1281.
- IMSL Stat/Library Volume 2*. (1997) Houston, TX: Visual Numerics, Inc., 1189-1190.
- Jernquist, L. F., & Johansson, T. G. (1974) A laser doppler anemometer for the measurement of an arbitrary velocity component in highly turbulent fluid flows. *J. Phys. E: Sci. Instr.*, 7, 246-247.
- Jiang, N. (2006) Development of high repetition rate NO planar laser induced fluorescence imaging. *Doctoral Dissertation, The Ohio State University, Columbus, OH*.
- Kojima, J., & Nguyen, Q. V. (2004) Measurement and simulation of spontaneous Raman scattering in high-pressure fuel-rich H₂-air flames. *Meas. Sci. Tech.*, 15, 565-580.

- Koochesfahani, M. M. (1999) Molecular tagging velocimetry (MTV): Progress and applications. *AIAA paper # 99-3786*.
- Koochesfahani, M. M., Cohn, R. K., Gendrich, C. P., & Nocera, D. G. (1996) Molecular tagging diagnostics for the study of kinematics and mixing in liquid-phase flows. Proceedings from *the 8th International Symposium on Applications of Laser Techniques to Fluid Mechanics*, Lisbon, Portugal, 1.2.1 – 1.2.12.
- Kozlov, D. N., Hemmerling, B., & Stampanoni-Panariello, A., (2000) Measurement of gas jet flow velocities using laser-induced electrostrictive gratings. *Appl. Phys. B*, *71*, 585-591.
- Lading, L., Saffman, M., & Edwards, R. V. (1997) Laser anemometry based on collective scattering: the effects of propagating and nonpropagating fluctuations. *Optics and Lasers in Engineering*, *27*, 531-542.
- Lahr, M. D., Pitz, R. W., Douglas, Z. W., & Carter, C. D. (2006) Hydroxyl tagging velocimetry in cavity-piloted Mach 2 combustor. *AIAA paper # 2006-40*.
- Landau, L., & Placzek, G. (1934) Structure of the undisplaced scattering line. *Phys. Z. Soviet. Un.*, *5*, 172.
- Lemoine, F., Antoine, Y., Wolff, M., & Lebouche, M. (1999) Simultaneous temperature and 2D velocity measurements in a turbulent heated jet using combined laser-induced fluorescence and LDA. *Exp. Fluids*, *26*, 315-323.
- Lempert, W. R., Boehm, M., Jiang, N., Gimelshein, S., & Levin, D. (2003) Comparison of molecular tagging velocimetry data and direct simulation Monte Carlo simulations in supersonic micro jet flows,” *Exp. Fluids*, *34*, 403-411.
- Lempert, W. R., Magee, K., Ronney, P., Nosenchuck, D. M., & Miles, R. B. (1993) Flow tagging in water by photo-activated nonintrusive tracking of molecular motion (PHANTOMM). *AIAA paper # 93-0517*.
- Lempert, W. R., Zuzeek, Y., Uddi, M., Frederickson, K., & Jiang, N. (2006) RELIEF velocimetry using picosecond tagging and Nd:YAG-based interrogation. *AIAA paper # 2006-2970*.
- Li, Y., Roberts, W. L., & Brown, M. S. (2002) Investigation of gaseous acoustic damping rates by transient grating spectroscopy. *AIAA Journal*, *40*, 1071-1077.
- McKenzie, R. L. (1996) Measurement capabilities of planar doppler velocimetry using pulsed lasers. *Appl. Optics*, *35*, 948-964.

- McMillin, B. K., Seitzman, J. M., & Hanson, R. K. (1994) Comparison of NO and OH planar fluorescence temperature measurements in scramjet model flowfields. *AIAA Journal*, 32, 1945-1952.
- Melling, A. (1997) Tracer particles and seeding for particle image velocimetry. *Meas. Sci. Technol.*, 8, 1406-1416.
- Mielke, A. F., Elam, K. A., & Sung, C. J. (2007) Development of a Rayleigh scattering diagnostic for time-resolved gas phase flow velocity, temperature, and density measurements in aerodynamic test facilities. Proceedings from *the 22nd International Congress on Instrumentation in Aerospace Simulation Facilities*, Pacific Grove, CA.
- Mielke, A. F., Seasholtz, R. G., Elam, K. A., & Panda, J. (2005) Time-average measurements of velocity, density, temperature, and turbulence velocity fluctuations using Rayleigh and Mie scattering. *Exp. Fluids*, 39, 441-454.
- Miles, R. B., Grinstead, J., Kohl, R. H., & Diskin, G. (2000) The RELIEF flow tagging technique and its application in engine testing facilities and for helium-air mixing studies. *Meas. Sci. Technol.*, 11, 1272-1281.
- Miles, R. B., Lempert, W. R., & Forkey, J. N. (2001) Laser Rayleigh scattering. *Meas. Sci. Technol.*, 12, R33-R51.
- Miles, R. B., Lempert, W. R., Zhang, B., & Zhou, D. (1993) Local time-averaged and instantaneous temperature measurements by RELIEF flow tagging. *AIAA paper # 1993-0514*.
- Miller, M. F., Bowman, C. T., & Mungal, M. G. (1998) An experimental investigation of the effects of compressibility on a turbulent reacting mixing layer. *J. Fluid Mech.*, 356, 25-64.
- Miller, M. F., Kessler, W. J., & Allen, M. G. (1996) Diode laser-based air mass flux sensor for subsonic aeropropulsion inlets. *Appl. Optics*, 35, 4905-4912.
- Nooren, P. A., Versluis, M., van der Meer, T. H., Barlow, R. S., & Frank, J. H. (2000) Raman-Rayleigh-LIF measurements of temperature and species concentrations in the Delft piloted turbulent jet diffusion flame. *Appl. Phys. B*, 71, 95-111.
- O'Byrne, S., Danehy, P. M., & Cutler, A. D. (2004) Dual-pump CARS thermometry and species concentration measurements in a supersonic combustor. *AIAA paper # 2004-0710*.
- Oppenheim, A. V., & Schafer, R. W. (1975) *Digital Signal Processing*, Englewood Cliffs, NJ: Prentice-Hall.

- Paa, W., Müller, D., Stafast, H., & Treibel, W. (2007) Flame turbulences recorded at 1 kHz using planar laser induced fluorescence upon hot band excitation of OH radicals. *Appl. Phys. B*, 86, 1-5.
- Palmer, J. L., & Hanson, R. K. (1996) Temperature imaging in a supersonic free jet of combustion gases with two-line OH fluorescence. *Appl. Optics*, 35, 485-499.
- Panda, J., & Seasholtz, R. G. (1999) Velocity and temperature measurement in supersonic free jets using spectrally resolved Rayleigh scattering. *AIAA paper # 1999-0296*.
- Paul, P. H., Farrow, R. L., & Danehy, P. M. (1995) Gas-phase thermal-grating contributions to four-wave mixing. *J. Opt. Soc. Am. B*, 12, 384-392.
- Pietri, L., Amielh, M., & Anselmet, F. (2000) Simultaneous measurements of temperature and velocity fluctuations in a slightly heated jet combining a cold wire and laser doppler anemometry. *Int. J. Heat Fluid Flow*, 21, 22-36.
- Pitz, R. W., Ribarov, L. A., Wehrmeyer, J. A., & Batliwala, F. (1998) Ozone tagging velocimetry for unseeded velocimetry measurements in air flows. *AIAA paper # 1998-2610*.
- Raffel, M., Willert, C., & Kompenhans, J. (1998) *Particle Image Velocimetry, a Practical Guide*. Berlin: Springer-Verlag.
- Ribarov, L. A., Wehrmeyer, J. A., Hu, S., & Pitz, R. W. (2004) Multiline hydroxyl tagging velocimetry measurements in reacting and nonreacting experimental flows. *Exp. Fluids*, 37, 65-74.
- Roy, S., Meyer, T. R., Brown, M. S., Velur, V. N., Lucht, R. P., & Gord, J. R. (2003) Triple-pump coherent anti-Stokes Raman scattering (CARS): Temperature and multiple-species concentration measurements in reacting flows. *Opt. Comm.*, 224, 131-137.
- Roy, S., Meyer, T. R., Lucht, R. P., Belovich, V. M., Corporan, E., & Gord, J. R. (2004) Single-shot thermometry and multiple-species measurements using dual-pump, dual-broadband CARS in a liquid-fueled CFM56 combustor. *AIAA paper # 2004-0711*.
- Samimy, M., & Wernet, M. P. (2000) Review of planar multiple-component velocimetry in high-speed flows. *AIAA Journal*, 38, 553-574.
- Sandoval, R. P., & Armstrong, R. L. (1976) Rayleigh-Brillouin spectra in molecular nitrogen. *Phys. Rev. A*, 13, 752-757.
- Schlamp, S., Cummings, E. B., & Hornung, H. G. (1999) Beam misalignments and fluid velocities in laser-induced thermal acoustics. *Appl. Optics*, 38, 5724-5733.

- Schlamp, S., Hornung, H. G., Sobota, T. H., & Cummings, E. B. (2000a) Accuracy and uncertainty of single-shot, nonresonant laser-induced thermal acoustics. *Appl. Optics*, *39*, 5477-5481.
- Schlamp, S., Cummings, E. B., & Sobota, T. H. (2000b) Laser-induced thermal-acoustic velocimetry with heterodyne detection,” *Optics Letters*, *25*, 224-226.
- Seasholtz, R. G., Buggele, A. E., & Reeder, M. F. (1997) Flow measurements based on Rayleigh scattering and Fabry-Perot interferometer. *Optics and Lasers in Engineering*, *27*, 543-570.
- Seasholtz, R. G., & Greer, L. (1998) Rayleigh scattering diagnostic for measurement of temperature and velocity in harsh environments. *AIAA paper # 1998-0206*.
- Seasholtz, R. G., Panda, J., & Elam, K. A. (2002) Rayleigh scattering diagnostic for measurement of velocity and density fluctuation spectra. *AIAA paper # 2002-0827*.
- Shimizu, H., Noguchi, K., & She, C. Y. (1986) Atmospheric temperature measurement by a high spectral resolution lidar. *Appl. Optics*, *25*, 1460-1466.
- Stampanoni-Panariello, A., Hemmerling, B., & Hubschmid, W. (1998) Temperature measurements in gases using laser-induced electrostrictive gratings. *Appl. Phys. B*, *67*, 125-130.
- Stier, B., & Koochesfahani, M. M. (1999) Molecular tagging velocimetry (MTV) measurements in gas phase flows. *Exp. Fluids*, *26*, 297-304.
- Studer, D., & Vervisch, P. (2007) Raman scattering measurements within a flat plate boundary layer in an inductively coupled plasma wind tunnel. *J. of Appl. Phys.*, *102*, Retrieved September 9, 2007, from <http://jap.aip.org/jap/top.jsp>.
- Taylor, J. R. (1982) *An introduction to error analysis*. Mill Valley, CA: Oxford University Press.
- Tedder, S. A., Bivolaru, D., Danehy, P. M., Weikl, M. C., Beyrau, F., & Seeger, T. (2007) Characterization of a combined CARS and interferometric Rayleigh scattering system. *AIAA paper # 2007-0871*.
- Tenti, G., Boley, C. D., & Desai, R. C. (1974) On the kinetic model description of Rayleigh-Brillouin scattering from molecular gases. *Can. J. Phys.*, *52*, 285-290.
- Thurber, M. C., Grisch, F., & Hanson, R. K. (1997) Temperature imaging with single- and dual-wavelength acetone planar laser-induced fluorescence. *Optics Letters*, *22*, 251-253.

- Thurber, M. C., Kirby, B. J., & Hanson, R. K. (1998) Instantaneous imaging of temperature and mixture fraction with dual-wavelength acetone PLIF. *AIAA paper* # 98-0397.
- Thurow, B. S., Jiang, N., Lempert, W. R., & Samimy, M. (2005) Development of a megahertz-rate planar doppler velocimetry for high-speed flows. *AIAA Journal*, 43, 500-511.
- Toro, V. V., Mokhov, A. V., Levinsky, H. B., & Smooke, M. D. (2005) Combined experimental and computational study of laminar, axisymmetric hydrogen-air diffusion flames. *Proceedings of the Combustion Institute*, 30, 485-492.
- Tropea, C. (1995) Laser doppler anemometry: Recent developments and future challenges. *Meas. Sci. Technol.*, 6, 605-619.
- Vaughan, G., Wareing, D. P., Pepler, S. J., Thomas, L., & Mitev, V. (1993) Atmospheric temperature measurements made by rotational Raman scattering. *Appl. Optics*, 32, 2758-2764.
- Vaughan, J. M. (1989) *The Fabry-Perot interferometer. History, theory, practice, and applications*. Philadelphia: Adam Hilger.
- Wang, G. H., Clemens, N. T., & Varghese, P. L. (2005) Two-point, high-repetition-rate Rayleigh thermometry in flames: Techniques to correct for apparent dissipation induced by noise. *Appl. Optics*, 44, 6741-6751.
- Wehr, L., Meier, W., Kutne, P., & Hassa, C. (2007) Single-pulse 1D laser Raman scattering applied in a gas turbine model combustor at elevated pressure. *Proceedings of the Combustion Institute*, 31, 3099-3106.
- Welch, P. D. (1967) The use of fast Fourier transform for the estimation of power spectra: A method based on time averaging over short, modified periodograms. *IEEE Trans. on Audio and Electroacoustics*, AU-15, 70-73.
- Wernet, M. P. (2004) Planar particle imaging doppler velocimetry: a hybrid PIV/DGV technique for three-component velocity measurements. *Meas. Sci. Technol.*, 15, 2011-2028.
- Wernet, M. P. (2007) Temporally resolved PIV for space-time correlations in both cold and hot jet flows. *Meas. Sci. Technol.*, 18, 1387-1403.
- Whalen, A. D. (1971) *Detection of Signals in Noise*. New York: Academic Press.
- Yeh, Y., & Cummins, H. Z. (1964) Localized fluid flow measurements with an He-Ne laser spectrometer. *Appl. Phys. Letters*, 4, 176-178.

Yip, S., & Nelkin, M. (1964) Application of a kinetic model to time-dependent density correlations in fluids. *Phys. Rev.*, 135, A1241-A1247.